Universidad Autónoma de Nuevo León

Facultad de Ciencias de la Tierra

Bending The Sierra Madre Oriental: Paleomagnetism And Structural Analysis Of Jurassic And Cretaceous Rocks In North Eastern Mexico.

By

Rafael Guerra Roel

Como requisito parcial para obtener el grado de doctor en ciencias con orientación en geociencias.

Julio 2025

Universidad Autónoma de Nuevo León

Facultad de Ciencias de la Tierra

Bending the Sierra Madre Oriental: Paleomagnetism and Structural Analysis of Jurassic and Cretaceous Rocks in North Eastern Mexico.

By

Rafael Guerra Roel

ha sido aceptada como requisito parcial para optar al grado de

Doctor en Ciencias con Orientación en Geociencias

_____

Director de Tesis

Dr. Gabriel Chávez Cabello

Julio 2025

Universidad Autónoma de Nuevo León

Facultad de Ciencias de la Tierra

Bending the Sierra Madre Oriental: Paleomagnetism and Structural Analysis of Jurassic and Cretaceous Rocks in North Eastern Mexico.

By

Rafael Guerra Roel

ha sido aceptada como requisito parcial para optar al grado de

Doctor en Ciencias con Orientación en Geociencias

Director Externo

Dr. Daniel Pastor Galán

Julio 2025

Bending the Sierra Madre Oriental: Paleomagnetism and Structural Analysis of Jurassic and Cretaceous Rocks in North Eastern Mexico.

By

Rafael Guerra Roel

Comite Doctoral

Dr. Gabriel Chávez Cabello	Dr. Daniel Pastor Galán
Dr. José Jorge Aranda Gómez	Dr. José Rafael Barboza Gudiño
Dr. César Francisco Ramírez Peña	Subdirector de Posgrado Dr. Fernando Velasco Tapia

Julio 2025

Bending the Sierra Madre Oriental

Paleomagnetism and Structural Analysis

of Jurassic and Cretaceous Rocks in North Eastern Mexico.

By Rafael Guerra Roel

A mis hijas Catalita y Elizabeth

A mi Esposa Diana

A mis Padres Irma y Jaime

Agradecimientos

Este proyecto me llevo a lugares que jamas crei visitar, y a circunstancias en las cuales jamas pensé verme. Durante el trayecto conocí a personas extraordinarias. Este camino me enseñó la verdadera esencia de los que me rodean. Y mas que nada me enseño a conocer quien soy yo.

Valla... agradecimientos, por donde empezar...

Como dijo mi asesor Daniel, "-*Tantos años hablando de rocas hace que escribir sobre ellas sea sencillo. A diferencia de las personas, las rocas no se enfadan por publicar sobre ellas meras suposiciones. Tampoco les molesta que te olvides de mentar aquel afloramiento tan bueno que tantos datos aportó*-". Espero no omitir a nadie, pero si lo hago, sepan que no es intencional, en mi defensa. Años de lamer rocas y de discutir modelos geologicos dignos de serie de ciencia ficción aunado a altos consumos de atun y alcohol, puedan haber hecho estragos en mi memoria.

Es solamente lógico ser agradecido con las personas que me han ayudado, pero, soy creyente de que no solo debemos de ser agradecidos por las cosas buenas en esta vida, si no, de igual manera ser agradecido por las dificultades y obstaculos que la vida nos pone enfrente. Porque estos nos hacen mejores personas.

Sin duda la persona mas importante en esta gran travesia es la que estuvo conmigo desde antes que pudieramos ver el inicio del camino. En las buenas, en las no tan buenas, en las malas y en las no tan malas. Estuviste ahí para mí antes y durante el proceso. Y afortunadamente sigues aqui, apoyandome y dandome aliento por mas fantasiosas que sean mis ideas. Tu creiste en mi

desde el principio. Grandes adversidades y obstáculos se nos atravesaron en el camino y las noches se hicieron muy obscuras. Pero nunca me soltaste la mano.y nunca solte la tuya. Gracias a eso, juntos pudimos salir adelante. Sin duda sin ti este logro no hubiera sido posible. Me refiero a mi mejor mitad, mi compañera y el amor de mi vida. Gracias **Diana.**

Dios ah sido bueno. Y estoy agradecido por todo lo que me ah concedido lograr. Pero no más agradecido que por el tiempo que me ah dejado estar al lado de mis padres.. **Papá, Mamá,** espero que este logro mio sea un oleo para sus corazones y que se sientan satisfechos por su trabajo y su gran esfuerzo. Que de primera mano sepan que nada de lo que han hecho ah sido en vano. Gracias por este mundo de esfuerzo. Gracias mamá por tu apoyo incondicional y por siempre estar ahi cuando te necesite. Gracias Papá por ayudarme a creer en mi mismo y por impulsarme a querer ser mejor y a jamas conformarme. Gracias a ambos por enseñarme a ser resiliente y decidido. Y mas que todo a ser muy terco con las cosas que quiero y por enseñarme a trabajar por ellas. Que este cuarto titulo profesional sea referente de su gran labor como padres. Que hoy y siempre mis logros sean tambien de ustedes.

Gracias a mi director de tesis **Gabriel Chávez Cabello** por toda su ayuda y sus enseñanzas. Si bien no fue facil, me impusaste a querer ser siempre mejor.
Quiero agradecer de una manera especial a mi asesor **Roberto Stanley Molina Garza**. Estaré eternamente agradecido por toda tu ayuda y enseñanzas. Hoy no estas aqui fisicamente pero se que estas viendome desde algun lugar muy relajado con los pies sobre la mesa brindando con mezcal y un cigarro. Gracias por todo, y espero verte de nuevo. Este trabajo es un modesto tributo a tu trabajo y trayectoria. Y a tus grandes aportaciones al entendimiento sobre la evolucion tectonica de Mexico y Norte America.

Despues de la subita partida de Roberto me vi perdido y sin apoyo. Crei que no tenia muchas opciones. Pero recorde una de las muy placenteras platicas con Roberto en la sala de su casa. Donde discutiamos trabajos interesantes, para mi sopresa muchos de los trabajos de investigadores que llegue a admirar eran buenos amigos de Roberto. Uno de ellos sobresalia amenudo en las platicas. Por la similitud de las cosas que el habia hecho y lo que yo estaba haciendo. Lo contacte, y me respondio. "- No te preocupes Rafa, yo te ayudo" (Cosa que despues te arepentias jajajaja) Gracias "Tio" por toda tu ayuda. Me sacaste de un hoyo que no crei iba a salir. "Que viva el orden y la Ley! Que viva España y el Rey!!! Gracias **Dr. Daniel Pastor Galan.**

Gracias al **Dr. Jose Jorge Aranda** por todo su apoyo y sus consejos y por abrirme las puertas de su casa. Por ultimo agradesco al **Dr. Cesar Francisco Ramirez Peña** y al **Dr. Jose Rafael Barboza Gudiño** por su colaboracion y sus observaciones al manuscrito final.

Una mención especial a los amigos que me acompañaron durante este largo proceso, en esos interminables dias de campo y laboratorio. Al ya Ingeniero **Gerardo Patiño Méndez** alias el "Jerry", que no faltó a ninguna jornada de campo ni laboratorio. Al Ingeniero **David Galvan** alias el "Zlatan" al Master **"Jorgito" Flores Salgado** y al terrible **Carlitos**! Minions muy importantes en este trabajo. Catarino y los rurales se agarraban a balazos todos los dias a las 5am a maximo volumen. ¡¡¡Agradecido con el de arriba... !!!!

Gracias al **Dr. Harald Böhnel** y a los brothers del Laboratorio de Pmag en el entonces CEGEO de Juriquilla al **Dr. Alejandro y al Dr. Hector Ibarra** por su ayuda con los equipos del laboratorio.

Muy agradecido con mis couches que siempre estaban pal desestres! El **Dr. Simon Reyes, El MC. Sergio "Maquina"**, El **Dr. Omar Diaz** (Que si cura gente), al **MC. Pepe "Pitino corajes" Aguirre** y al **Daniel "Sobador" Guerrero**. Que la fuerza del Maquineo los acompañe siempre, y que nunca falten las mañanas con Franco de Vita!

Gracias a esos amigos que me encontre en el camino. A **Lenin Valdez. Diana Clara, Coste, Esteban Gomez y Natalia Ovalle**, que sin duda hicieron la estancia en Juriquilla mas amena!

Gracias a todo el personal del laboratorio del Fort Hoofddijk al **Dr. Mark Dekkers, Dr. Lennart de Groot, Dr. Wout Krijgsman, Dr. D.V. (Dan) Palcu, Msc. Rosa de Boer, MSc Liz van Grinsven**, **Dr. Frenk Out** y a **Romy Meyer MSc.**
Thank you for your valuable support and friendship. I'll never forget you guys.

Un Agradecimiento muy especial a mi Familia del otro lado del oceano Atlantico. A las personas que me abrieron las puertas de su casa sin conocerme y por ayudarme cunado lo necesité en un pais, en un continente desconocido a mi hermano del alma **Wim de Hass y su Esposa Niritsia** y su hermosa familia. Estare eternamente agradecido por todo su apoyo y su amistad.
" I would like give a very special mencion of gratefulness to my family on the other side of the Atlantic ocean. I will be eternally grateful to the people that welcomed me into their home without knowing me and helped me when I most needed it . To Wim de Hass, his wife Neritisia and their beautiful family. Thank you for all your support and for your friendship."

Agradesco profundamente a los Hermanos de las Logias de Utrecht, Paises Bajos. Por su hospitalidad, su apoyo y fraternidad. Al Hermano Rudolph, H:. Rinus, H:. Magnuson ...

A todos ustedes y a los que no menciono. Gracias, Gracias, Gracias.

Contents

Resumen

Las curvaturas en los sistemas orogénicos son una de las características más comunes en límites de placas convergentes alrededor del mundo. Estos segmentos curvados poseen información acerca de su evolución tectónica que algunas veces se pierde en procesos tectónicos destructivos. La Cordillera Norteamericana es un cinturón plegado sinuoso que delimita el margen occidental de Norte América. Esta cordillera está conformada por varios salientes y recesos que son producto de ~350 millones de años de subducción episódica bajo el cratón de Norteamérica, acreción de terrenos y vulcanismo. La parte sur de la cordillera Norteamericana está representada por "El Orógeno Mexicano" del Cretácio-Paleogeno, que es producto de una serie de eventos tectónicos prolongados, los cuales involucran bloques tectonicos y secuencias antiguas depositadas en las cuencas resultantes de la fragmentación de Pangea occidental y el *rollback* de la placa oceánica de Kula. Durante este tiempo la sedimentación fue propiciada por una configuración de horst y grabens entre Norte y Suramérica. Posteriormente, la subducción episódica de las placas Kula/Farallón en conjunto con cambios en el ángulo de subducción en el margen occidental propició la formación de arcos magmáticos, inversión de cuencas, plegamientos y cabalgaduras. Los dominios cordilleranos del Orogeno Mexicano están representados por La Sierra Madre Occidental (Transpais) y el Cinturón de Pliegues y Cabalgaduras Mexicano (Antepaís). Una de las provincias fisiográficas más prominentes del Cinturón de Pliegues y Cabalgaduras Mexicano es la Sierra Madre Oriental. La parte noreste de este cinturón exhibe una curvatura de ~110° convexa al noreste. En las últimas décadas esta prominente característica ha sido objeto de muchos estudios versados en los aspectos geológicos, geocronológicos, sedimentológicos y geofísicos de su naturaleza. Sin embargo, estos estudios

no se han enfocado en la cinemática ni en las diferentes características en planta de la Sierra Madre Oriental. En este trabajo se estudió la cinemática de este sector en el NE de la Sierra Madre Oriental empleando Paleomagnetismo en combinación con análisis estructural regional para abordar la problemática de su evolución tectónica. Para esto, se seleccionaron dos grupos de rocas para ser analizadas en este estudio, los lechos rojos pre-Oxfordianos de las formaciones Nazas, La Joya y La Boca, así como la Formación Taraises del Cretácico Inferior. Debido a su edad y distribución son idóneas para atender adecuadamente las incógnitas en el lapso de tiempo de deformación de la Sierra Madre Oriental. Esto fue complementado con una compilación bibliográfica rigurosa de los estudios paleomagnéticos previos en la Sierra Madre Oriental. Los resultados muestran evidencia de magnetizaciones primarias Jurásicas y del Cretácico temprano asi como tres eventos de remagnetización (Jurásico Tardío, Cretácico Tardío y Paleogeno). Adicionalmente los datos muestran rotaciones antihorarias significativas de hasta 90° en el flanco norte y rotaciones horarias menos prominentes (~30°) en el flanco sur del area estudiada. Estos resultados comprueban que la Sierra Madre Oriental experimentó un proceso de plegamiento oroclinal de los 90 a los 50 Ma que a su vez revela que la SMO se formó originalmente como un cinturón semi recto con vergencia aproximada de Norte a Sur.

Abstract

Curvatures in orogenic systems are one of the most common features in convergent plate margins around the world. These curved segments hold valuable information about the tectonic evolution that is sometimes lost to destructive tectonic processes. The North American cordillera is a winding orogenic belt that borders the western margin of North America and is conformed by numerous salients and recesses that were generated due to ~350 million of years of intermittent subduction underneath the American craton, Terrain accretion and its consequent volcanism. The southern segment of the NA Cordillera, “The Cretaceous-Paleogene Mexican Orogen”, is product of a series of protracted tectonic events that involved ancient tectonic crustal blocks and sedimentary secuences deposited in the resulting basins from the breakup of western Pangea and the roll-back of the oceanic Kula plate. During this time, sedimentation was triggered by a configuration of horst and grabens between North and South America. Afterwards, The continued subduction of the Kula-Farallon constituent plates in the western margin along with angle changes in in the subduccion, triggered arc formation, basin inversion, thrusting and folding. The cordilleran dominions of the Mexican Orogen are represented by the Sierra Madre Occidental (Hinterland) and the Mexican fold and Thrust Belt (Foreland). One of the most prominent physiographical provinces in the Mexican foreland belt is the Sierra Madre Oriental. Its North Eastern segment exhibits a 110° curvature convex to the North East. In the past several decades this striking feature has been the object of many studies versing on the Geological, geochronological, sedimentological and geophysical aspects of its nature. However, these studies have not focused on the kinematics of the North eastern section of Sierra Madre Oriental nor on the map view characteristics that this section of this Thrust belt shows. This work investigates the kinematics of the

northeastern curvature of Sierra Madre Oriental by applying paleomagnetism combined with a regional structural analysis to address the tectonic evolution of the Sierra Madre Oriental. Two sets of rocks were chosen to be analyzed in this study. The pre-Oxfordian red beds of NE Mexico, (The Nazas, La Boca and La Joya Fm.) and the Early Cretaceous Taraises Formation. These lithologies are appropriate in age and in distribution to properly assess the timeframe of deformation of the Sierra Madre Oriental. This was complemented with a rigorous bibliographical compilation of the previous Paleomagnetic analyses in the Sierra Madre Oriental. The results show evidence of primary Jurassic and Early Cretaceous magnetizations as well as three widespread remagnetization events in the Sierra Madre Oriental (Late Jurassic, Late Cretaceous and Paleogene). Additionally, significant anticlockwise vertical axis rotations of up to 90° in the northern limb of the curvature and less prominent clockwise rotations in the southern limb of 30°. These results prove that the Sierra Madre Oriental underwent a oroclinal bending/buckling process from 90 to 50 Ma. This thesis speculates with the potential process that could drive the orocline formation: a lapse of flat slab subduction that ultimately led to the thick-skinned style deformation pulse during Eocene time.

Chapter 1

Introduction

"The invariable mark of wisdom is to see the miraculous in the common."

— **Emerson**

Orogens constitute one-fourth of all the continental crust on Earth and represent one of the most important physiographic elements on the planet. Orogens hold the bulk of Earth's economic and natural resources and distribution. Controls local climate and strongly influences global climatic zones. Mountain chains hold diverse ecosystems and natural diversity, and approximately 85 % of the world's species of amphibians, birds, and mammals, many of which cannot be found anywhere else in the world (Rahbek et al., 2019). Finally, orogens have played a fundamental role in many aspects of human evolution. The development of ancient and modern societies revolves around mountainous regions and the hydrological conditions and mineral resources they create (Price, 2015; Rahbek et al., 2019; Zhu et al., 2022). Understanding the processes and the mechanisms that create mountain belts and their evolution is one of the most important keys to comprehend Earth's history, our origins, and our future as a society, enabling us to find and extract more natural resources towards a more sustainable life.

Orogenic studies typically focus on cross-sections at different scales, from hinterlands to forelands, to understand the kinematics and dynamics of mountain building (e.g. DeCelles, 2004; DeCelles et al., 2009; Fitz-Díaz et al., 2018; Pfiffner, 2017; Schmidt et al., 2014). This approach has been fruitful in deciphering the intricacies of transverse orogenic evolution. However, orogens are often non-cylindrical and/or significantly curved (e.g. the Variscan, Andes, Alaskan ranges, Central Asian Orogenic Belt, Eastern Pontides, Lesser Caucasus...). Classical cross-section studies do not provide enough information to understand the lateral variations of such orogens adequately. Hence the importance of a map-view approach to better understand orogen kinematics and the mechanisms that create them.

1.1 Orogenic curvature: Concept

Curved segments of orogens have intrigued Earth scientists since the 19th century. Early terms like ‘salients,’ ‘recesses,’ ‘promontories,’ and ‘reentries’ were used to describe the concave or convex shapes of these arcs relative to the (paleo-)continental margin, without addressing their geological significance (Miser, 1932). In 1955 the term “Orocline” was introduced (Carey, 1955), derived from the Greek “oros” meaning mountain and “clino” to bend. Its original meaning describes a linear orogenic belt that acquired a curvature. Since Carey, geologists have developed several ways to classify curved mountain belts (e.g. Hindle & Burkhard, 1999; Marshak, 1988; Ries & Shackleton, 1976; Sussman & Weil, 2004). Most of these systems are grounded on the shape of the orogen and the deformation paths. The main drawback of such classifications is that they require knowledge of the mechanism behind the curvature formation, which often is obscured in older orogens.

1.1.1 Kinematic classification

Unlike mechanism-based systems, Weil and Sussman (2004; partially modified by Johnston et al., 2013) proposed a kinematic classification of curved orogens. This classification describes the movement but does not explain its cause. A kinematic classification is simpler and, importantly, knowing the kinematics is crucial to understanding any formation process for tectonic features. This thesis follows this classification, which identifies two different types of curved orogens:

a) Primary Arcs

The first distinction of curvatures is of a primary arc or curvature (not to be mistaken with volcanic arc). Primary arcs are defined as arcuate or curved orogens whose curvature is inherited from physiographic features or previous

deformation processes and acquired no tightening during subsequent deformation events (Figure 1.1 A). Primary arcs do not account for any vertical axis rotations regardless of the total orogenic curvature. To discriminate between Primary Arcs (non-rotational) and Oroclines (rotational) one must implement the characterization of primary features that register the initial orientation of the orogen about a point of reference (Eldredge et al., 1985; Hindle & Burkhard, 1999).

b) Oroclines

Carey (1955) defines an orocline as "an orogenic system which has been flexed in plan to a horse-shoe or elbow shape". The kinematic classification of Oroclines involves vertical axis rotations on elements either formed prior (Secondary) or during (Progressive) the orocline bending process (Johnston et al., 2013; Sussman & Weil, 2004). The driving mechanisms of orocline bending are diverse in scales from thrust sheets to tectonic plates and may even involve the lithospheric mantle (Pastor-Galán et al., 2012).

Progressive Oroclines

Progressive Oroclines acquire their curvature during the main orogenic pulse. This term also includes belts that acquire only a portion of their curvature during a subsequent deformation event. Progressive oroclines portray vertical axis rotations but are systematically of less magnitude than the amount of the orogen’s curvature (Figure 1.1 B). This depicts a kinematic intermediate member between primary arcs and secondary oroclines (Johnston et al., 2013).

Secondary Oroclines

Secondary oroclines are orogenic belts that acquire all their curvature in a deformation event that postdates the orogenic building (Figure 1.1 C). These structures derive from an initially roughly rectilinear orogen that later

underwent bending or buckling. The relationship between the vertical axis rotations in secondary oroclines is proportional to the amount of curvature at any given place in the orogen's curvature (Figure 1.1 C).

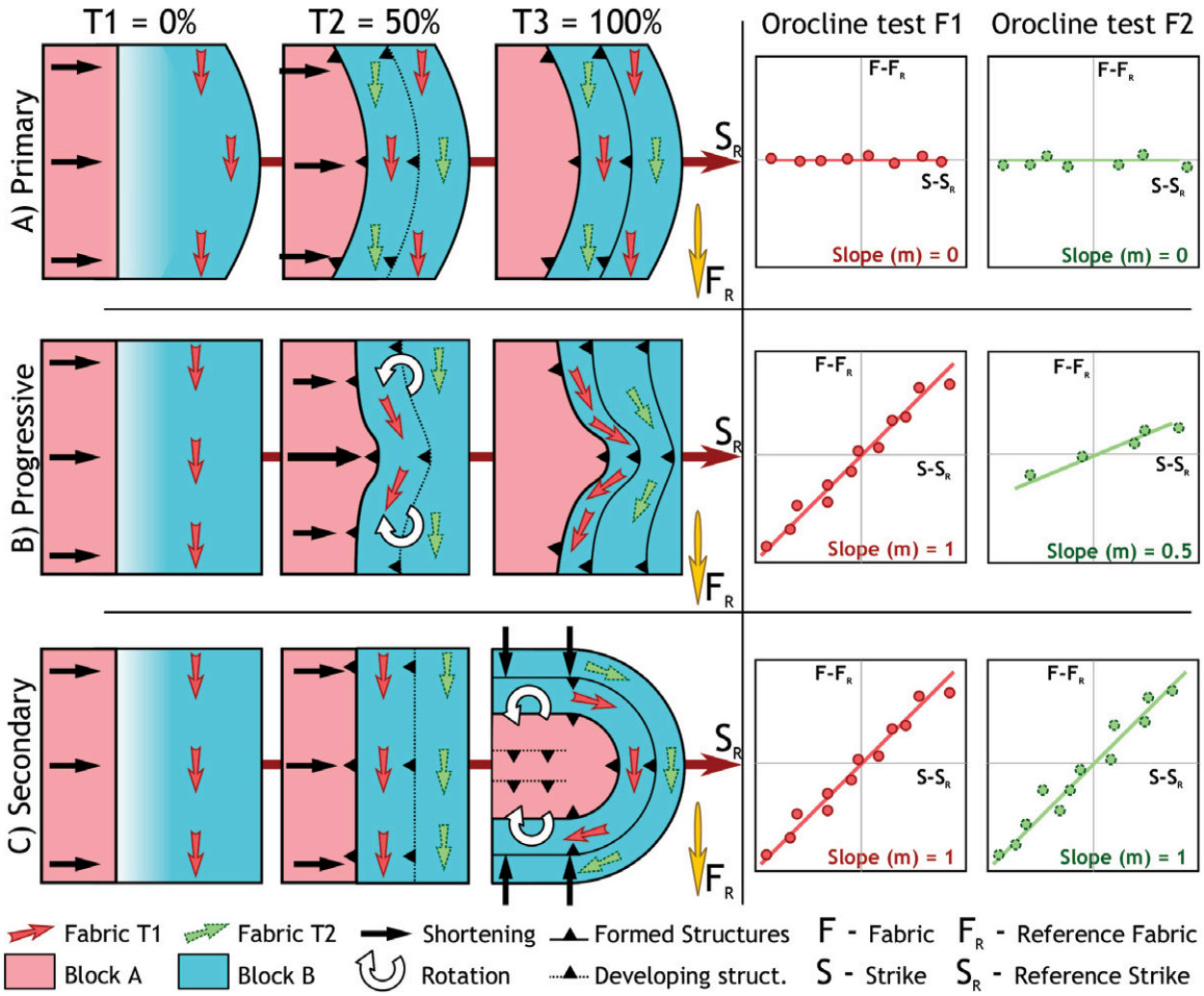

Figure 1.1 Different kinematics for orocline formation at three different stages: T1 before any orogenic deformation (0%); T2 during the orogenic deformation process (50%); and T3 when the orogenic edifice has been formed (100%). To the right the expected orocline test for fabrics developed at T1 and T2. (A) Primary curve, in which the entire curvature is inherited, i.e., existed before the orogeny. (B) A typical case for a progressive orocline test, in which the curvature is acquired during the orogeny (primary orogenic bend vs. secondary orocline) and an intermediate field (progressive orocline). (C) A secondary orocline in which all the curvature postdates the orogen formation (Pastor-Galán et al., 2017).

Understanding the kinematic evolution of oroclines requires a comprehensive analysis of both the timing and rate at which curvature forms within an orogen, as well as determining the extent to which this curvature predates orogenesis. To achieve this, it is essential to gather accurate, statistically robust, and independent directional datasets. Traditionally, paleomagnetic data have been the primary tool for investigating vertical-axis rotations (e.g., Pueyo et al., 2007, 2016; Weil et al., 2013). However, other datasets, such as structural and sedimentological data, including deformation fabrics and paleocurrent directions, have also been employed to study vertical-axis rotations (e.g., (Kollmeier et al., 2000; Li et al., 2012; Malandri et al., 2017; Pastor-Galán et al., 2011; Shaw et al., 2012; van Hinsbergen & Schmid, 2012; Walcott & White, 1998; Yonkee & Weil, 2010 b).

1.1.2 Classifying Methods: Kinematics

The strike test, introduced in the early 1980s by Schwartz and Van der Voo (Schwartz & Van der Voo, 1983) and Eldredge et al. (1985), provides a straightforward yet effective method for evaluating the kinematics of curved orogens. This test analyzes the relationship between regional orogenic strike (relative to a reference direction) and the orientations of specific geological fabric elements. Initially developed for paleomagnetic comparisons between declinations and orogenic strikes, the strike test has since been adapted to accommodate various geological data, including strain data (Yonkee & Weil, 2010 b), fracture data (Pastor-Galán et al., 2011), calcite twin data(Kollmeier et al., 2000), anisotropy of magnetic susceptibility lineations (Weil & Yonkee, 2009), and paleocurrent directions (Shaw et al., 2012; Weil et al., 2013).

Despite its usefulness, the classical orocline test using OLS regression has notable limitations. It assumes no variance in each data point, effectively treating all measurements as perfectly accurate and precise. However, geological measurements are often subject to errors, including instrument precision, operational mistakes, and uncertainties related to the timing of

geological events. These errors introduce variance in both the dependent variable (F) and the independent variable (S), leading to a phenomenon known as regression dilution or attenuation (Draper & Smith, 1998). This causes the regression slope to be biased toward lower values, particularly when uncertainties exist in both variables. Moreover, OLS is asymmetric, meaning that the regression of F on S is not equivalent to the regression of S on F (Frost & Thompson, 2000), reducing the method's robustness for quantifying orogenic kinematics.

To overcome these challenges, Pastor-Galán et al. (2017) proposed a more robust method using Total Least Squares (TLS) regression coupled with bootstrapping on uncertainties. This approach accounts for errors in both dependent and independent variables without introducing bias or arbitrary weighting, providing a more accurate means of analyzing the kinematic evolution of oroclines (Golub & van Loan, 1980; Markovsky & Van Huffel, 2007).

1.1.3 Main tectonic drivers for orocline formation

Oroclines are the largest geological folds on Earth. As such, the mechanisms of formation are typically explained as bending or buckling (e.g. Pastor-Galán et al., 2012) akin to the classical classification of Ramsay (1967).

Orocline bending refers to oroclines that form in response to a stress field applied at a high angle to the orogen's long axis. Models that involve orocline bending include tensile bending caused by the oceanic plate rollback (Cifelli et al., 2007, 2008; Rosenbaum & Lister, 2004; Schellart et al., 2007; Stegman et al., 2006), as well as compressive bending triggered by wrapping around tectonic obstacles or indentors (e.g.(Keep, 2000; Stamatakos & Hirt, 1994; Thomas & Whiting, 1995).

Orocline buckling refers to the orogenic curvature that forms in response to an orogen parallel stress field. Models invoking orocline buckling

involve relative movements ranging from hundreds to thousands of kilometers and operate on a lithospheric scale, impacting both the crust and the lithospheric mantle (e.g.(Johnston, 2001; Krýza et al., 2021; Weil et al., 2013). The only way to account for the large-scale deformation, the involvement of the lithospheric mantle, and the significant translations needed for secondary orocline formation is through subduction processes *sensu lato*.

1.2 The Curvature Problem in NE Mexico.

The American Cordillera runs along the Pacific coast of the Americas (Figure 1.2). It encompasses notable mountain belts like the Rockies, Sierra Madre Oriental, and the Andes, as well as extensive plateaus (Colorado, Atacama). The cordillera includes Pangea derived terranes that have interacted with magmatic arcs, and oceanic plateaus (Guerrero, Baja-BC, Kula Plateau; (Keppie, 2004). It also exhibits several striking changes in its trend, such as in Alaska (Johnston, 2001), Panama (Montes et al., 2012), the Colombian Eastern Cordillera (Jiménez et al., 2014), Bolivia (Eichelberger & McQuarrie, 2015), and Patagonia (Maffione et al., 2010). Unraveling the kinematics of these bends is crucial for understanding the Cordilleran geodynamics (e.g., Johnston, 2001).

This thesis focuses on the broad curvature of the Sierra Madre Oriental located in northeastern Mexico (Figure 1.2). This area covers the Torreon Recess, located near the city by the same name in Coahuila state, the Monterrey Salient, the Concepción del Oro Salient, and the San Luis recess on the central eastern front of the Sierra Madre Oriental. The curvature of the Sierra Madre Oriental in northeastern Mexico has been overlooked in the sense of its kinematics. Although relatively well known in cross-section (e.g. Fitz-Díaz et al., 2018 and references therein), the Sierra Madre Oriental critically lacks data informing about the kinematics of its curvature. Pioneering studies using Paleomagnetism in the area described vertical axis

rotations (Belcher, 1979; Clement et al., 2000; González-Naranjo et al., 2012; Gose et al., 1982; Kleist et al., 1984; Molina Garza, 2004; Nemkin et al., 2019; Nowicki et al., 1993; Warrior, 2008), however, they were not focused on understanding rotations but on obtaining information on paleolatitudes or magnetostratigraphy. Many of the studies of the Sierra Madre Oriental are well versed in the structural, sedimentological and broad geological context of the area(Chávez-Cabello et al., 2004; Eguiluz et al., 2000; Fitz-Díaz et al., 2018; Goldhammer, 1999; Ocampo-Díaz et al., 2012, 2016; Padilla y Sánchez, 1985) but for the most part, they focused on isolated problems. It could be said that the efforts to understand the kinematic evolution of the SMO in NE Mexico began with the structural approach that minded fault slip data and the structural characterization of folded structures to determine paleostresses in the curvature of the Sierra Madre Oriental fold and thrust belt.

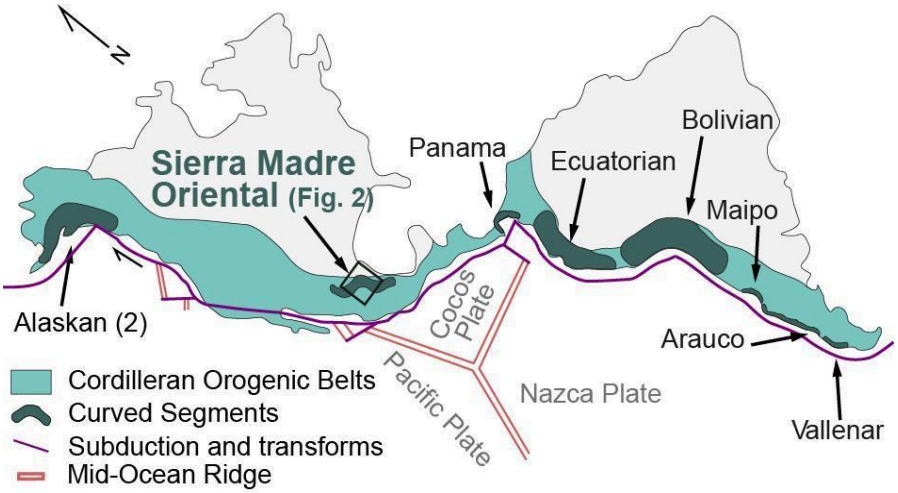

Figure 1.2 The American Cordilleran Orogenic Belt and some of the curved segments along its trace. The black square is the location of the study area (Modified from DeCelles et al., 2009).

1.3 Objectives

The main objective of this work is to resolve the kinematics of the curvature of the Sierra Madre Oriental in NE Mexico. The kinematics of the Sierra Madre Oriental are an important piece of information about the Mesozoic

reconstructions of Mexico and the paleo-Pacific tectonic system, as is the data inferred from them. Orogenic belt systems are the most visible product of subduction, hence, the best candidates on the surface to obtain the information that otherwise is hidden in the mantle by subducted plates. For example, the lack of data in the ongoing discussion about the Mexican Jurassic has led to speculative models that rely on geochemical signatures and current location of the available outcrops of the Jurassic rocks in Mexico to suggest paleogeographic scenarios (e.g.Dickinson & Lawton, 2001; Martini & Ortega-Gutiérrez, 2018; Parolari et al., 2022). On a larger scale, this study is of great importance to the overlapping problem of North and South America during Pangea reconstructions, for it portrays an alternative that has probably been considered but never tested. Also, this thesis in league adds to the intangible advancement of the knowledge of our country's natural resource distribution.

The distinction between primary curvature and oroclines is founded on the kinematic evolution of the structures formed in response to shortening within an orogen and the timing of curvature acquisition (Johnston et al., 2013). Thus, intrinsic data is required to make this distinction. Primarily, it is fundamental to determine vertical axis rotations, and secondly, the timing of such rotations (McCaig & McClelland, 1992). Paleomagnetism is the best method to determine rotations around a vertical axis, for it relies on the geomagnetic field which is independent of the deformation processes.

The study of Paleomagnetism, Rock magnetic properties, and Anisotropy of Magnetic Susceptibility supplemented with structural joint analyses on key lithological elements of the Sierra Madre Oriental allowed the determination of several important aspects of the investigation.

1. The quantification of vertical axis rotations of the studied elements.

2. The determination of remagnetization events that by correlation, will enable the establishment of the relative age of such rotations.
3. The assessment of the reliability of the Paleomagnetic data obtained in this study and previous works.
4. The classification of the curvature of the Sierra Madre Oriental in NE Mexico in the context of oroclines.
5. The determination of the age of the bending process.
6. The proposal of a Tectonic evolution model for the curved segment of the Sierra Madre Oriental in NE Mexico.

The new paleomagnetic data and critically reviewed previous studies along the curved section of the Sierra Madre Oriental will provide the necessary data to:

- Evaluate the kinematics of the curvature in the northeastern section of the Sierra Madre Oriental.
- Assess whether the outcrops of the Nazas Province represent their original location. Hence, allowing for more accurate reconstructions.
- Determine if the Jurassic volcaniclastics rotated in concert with the overlying Upper Jurassic - Cretaceous marine sedimentary cover.

Chapter 2

Geological Setting

True wisdom comes when we realize how little we understand about life, ourselves and the world around us”

— **Socrates**

2.1 The Sierra Madre Oriental

Mainland Mexico is an amalgam of several terrains, including pieces of continental Pangea, submarine fans, inverted marine/continental basins, continental arcs, and accreted submarine arcs. These elements were merged by horizontal shortening generated by subduction of the Kula and Farallon plates and relative motions between the trench and the North American plate during Mesozoic times(T. H. Anderson & Schmidt, 1983; Boschman, van Hinsbergen, et al., 2018; Campa & Coney, 1983; Centeno-García et al., 2008; Dickinson & Lawton, 2001; Eguiluz et al., 2000; Fitz-Díaz et al., 2018; Goldhammer, 1999; Martini & Ortega-Gutiérrez, 2018). The foreland of the Mexican Orogen is the Mexican Fold and Thrust Belt (MFTB). This feature is an orogenic belt composed of a series of salients and recesses that span approximately 2300 km with an orogenic axis trending NW from the Oaxacan Isthmus to the State of Sonora (Fitz-Díaz et al., 2018). The MFTB includes several physiographical elements: the Sierra Madre Oriental, the Mesa Central, Cuencas y Sierras del Norte, The Chihuahua-Coahuila fold belts, and the Sierra Madre del Sur. Also, it is partly intruded and covered by rocks of the Sierra Madre Occidental and the Trans-Mexican Volcanic Belt. “The Sierra Madre Oriental” (Eastern Mother Range) is located in the northeastern section of the MFTB (Figure 2.1). This part of the belt is a sinuous band dominated by folds and thrusts with three major curvatures, the Torreon recess, the Potosi recess, and the Monterrey Salient and the, Concepción del Oro salient (Figure 2.1). These curvatures may potentially reflect the coastline's original geometry and the basement highs' geographic distribution but this has not been yet determined (Chávez-Cabello et al., 2004; Nemkin et al., 2019; Padilla y Sánchez, 1985; Zachary, 2012). In this area, the regional structures show primarily a domain of symmetrical, overturned, detachment-, fault-bend, and fault-propagation folds, ordered by frequency of occurrence from most to least common respectably (Chávez-Cabello et al., 2004; Eguiluz et al., 2000;

Padilla y Sánchez, 1985; Ramírez-Peña & Chávez-Cabello, 2017). The style of contractional deformation is predominantly thin-skinned, characterized by folds and thrust that develop over a regional decollement (Pfiffner, 2006, 2017). Along the trace of the Mexican Fold and Thrust Belt, exposures of Jurassic volcano-sedimentary strata and Paleozoic metamorphic rocks are rare, and are usually enabled by high-angle reverse faults that cut older folds vertically or in the core of regional antiformal structures (Eguiluz et al., 2000; Fitz-Díaz et al., 2018; Guerra Roel, 2019; Pastor-Galán et al., 2012; Ramírez-Peña, 2017; Ramírez-Peña et al., 2019; Williams et al., 2021; Zavala-Monsiváis et al., 2012). In General, aside from the Torreon recess, the other curvatures previously mentioned resemble local disarrays or parasitic curvatures of the main general curvature, this is speculated to be the result of changes in basin geometry (Tardy, 1980; Tardy et al., 1975).

Foreland fold-and-thrust belts hold a narrow relationship to the parent basin they were created from, as close as the very foreland basins they enable and feed (DeCelles, 1994, 2004; DeCelles & Giles, 1996). Sedimentation, basin geometry, materials accumulated, and how stress is transmitted in the lithosphere dictate (for the most part) the geometry, occurrence of regional structures, style of deformation, and trend of the belt to be formed (Molnar & Buiter, 2023; Pfiffner, 2017).

2.2 Mesozoic Stratigraphical Synthesis of North Eastern Mexico

The oldest stratigraphical units exposed in NE Mexico portray a Precambiran-Paleozoic crystalline basement (Alemán-Gallardo et al., 2019; Cameron et al., 2004; Trainor et al., 2011). The units in this metamorphic complex and other Precambrian-Paleozoic metamorphic and magmatic rock (basement) exposures across Mexico are constituents of Pangea-derived continental blocks that are dispersed across Mexico. (Keppie &

Ortega-Gutiérrez, 2010; Ortega-Gutierrez et al., 1995). During the Mesozoic, the progressive breakup of Pangea, the ensuing western subduction, and the opening of the Gulf of Mexico shaped the paleogeography and stratigraphy of Mexico (Fitz-Díaz et al., 2018; Martini & Ortega-Gutiérrez, 2018 and references therein).

During the Late Triassic - Early Jurassic breakup of Pangea, fragments of continental crust were segregated between North and South America and formed various extensional and/or transtensional basins (Busby & Centeno-García, 2022; Centeno-García et al., 2005; Keppie & Ortega-Gutiérrez, 2010; Pindell & Kennan, 2001). The configuration of horsts and grabens influenced changes in the sedimentation environments, fault-bounded structural highs developed carbonate platforms and deep water marine environments developed in structural lows.

In the study area (Figure 2.1), exposures of the Late Triassic lithologies are scarce. They are represented by continental fluvial deposits, and submarine fans (*e.g.,* El Alamar Fm., Taray Fm. and, Potosi fan; Anderson, 2005; Barboza-Gudiño et al., 2010). In the western margin of Pangea/North America, the subduction setting prevailed through the Mesozoic with a hiatus during the Early Jurassic (Parolari et al., 2022).

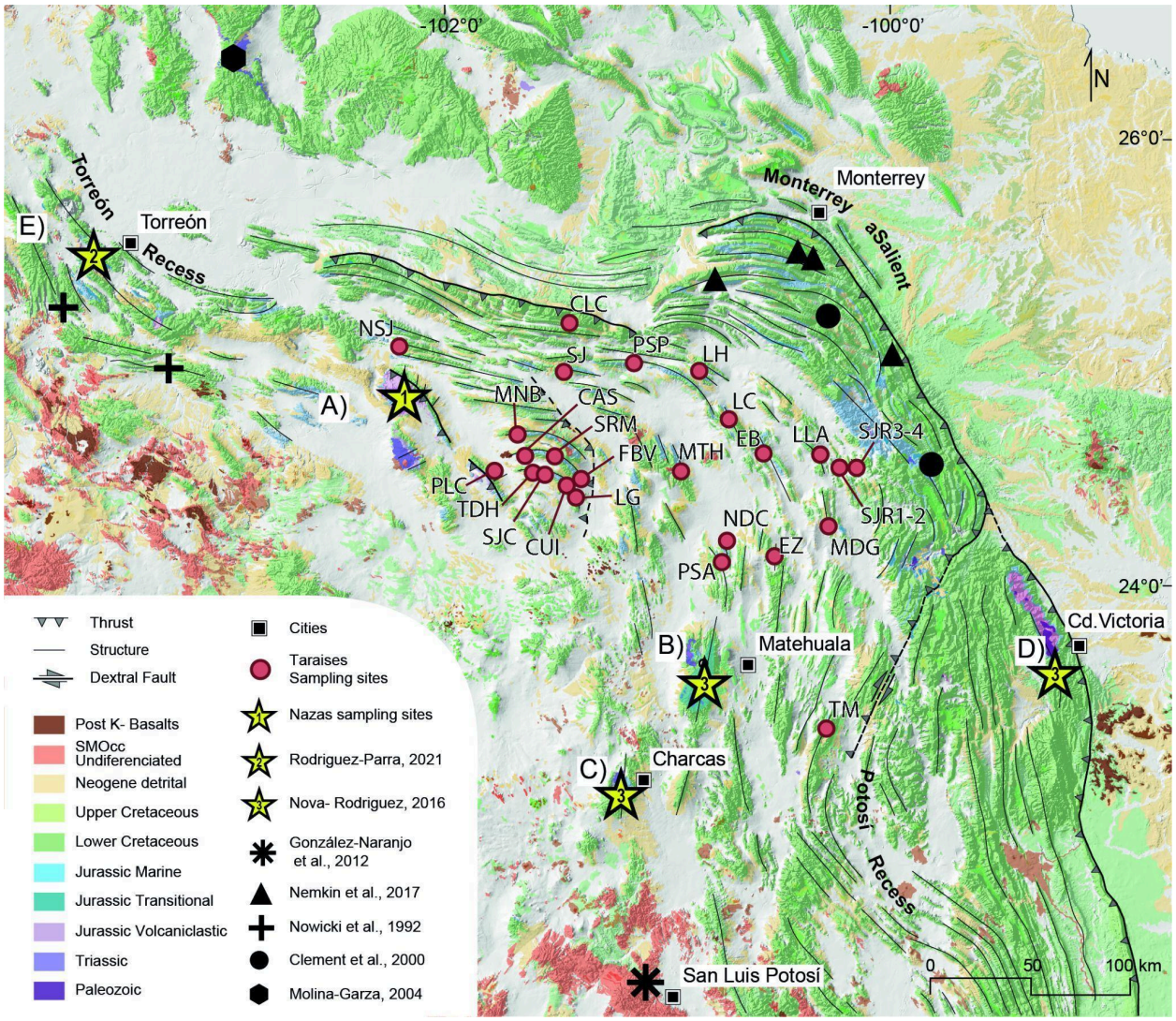

Figure 2.1 Regional Map of the broad curvature of the NE section of the Sierra Madre Oriental. Sampling sites of the Jurassic Red beds and Nazas Fm. are marked by stars, Taraises sampling sites are marked by red circles. Letters signal stared localities as follows: A) San Julian Uplift, B) Real de Catorce, C) Charcas, D) Huizachal Valley and E) Villa Juárez (Modified from Guerra Roel et al., 2024).

2.2.1 The Nazas Formation and Red Beds.

From the beginning of the Jurassic to Bathonian time in the Paleo-Pacific western margin of Mexico several siliciclastic sequences were deposited in structural grabens. The successions were made up of

intermediate-felsic volcanic rocks and epivolcaniclastics termed the Nazas and the La Boca formations.

The Nazas Formation is an Early to Middle Jurassic succession of reddish volcanogenic siltstone, sandstone, and volcanic breccias interbedded with volcanics that include pyroclastic rocks, like ash-fall tuffs and ignimbrites, with intermediate to mafic flows like andesites, dacites, and rhyolites (Barboza-Gudiño et al., 2008, 2012, 2021; Bartolini et al., 2003; Busby & Centeno-García, 2022; Pantoja-Alor, 1972). Outcrops are distributed in localized areas across north, northeast, central, and southern Mexico (Barboza-Gudiño et al., 2021; Bartolini et al., 1999). The Nazas Fm. age has been documented at the beginning of the Jurassic (~200 Ma) to the Callovian (~165 Ma) (Barboza-Gudiño et al., 2008, 2021; Bartolini et al., 2003; Zavala-Monsiváis et al., 2012). The Nazas Fm. changes laterally and is overlain by a Jurassic pre-Oxfordian sedimentary succession of red sandstone, siltstone, conglomerate, breccia, and volcaniclastic reddish beds (Busby & Centeno-García, 2022; Zavala-Monsiváis et al., 2012). These materials were deposited in continental to marginal marine transitional environments. Two formations have been defined: La Joya and La Boca formations which are commonly addressed as Jurassic red beds (Barboza-Gudiño et al., 2008, 2010; Fastovsky et al., 2005; Imlay et al., 1948; Mixon et al., 1959; Rubio Cisneros et al., 2011).

The origin of these volcaniclastic successions is still controversial. Patterns in normalized multi-element and discrimination diagrams suggest a volcanic continental arc origin or back-arc setting mainly linked to a subduction setting (Barboza-Gudiño et al., 2008, 2012, 2021). Recent works support the hypothesis that the lithology of the Nazas Fm. does not resemble a volcano-plutonic continental arc but a rift province constituted of isolated continental rift basins dominated by clastic successions and minor volcanic rocks (e.g. The Nazas Rift Province; Busby & Centeno-García, 2022). This is

founded on several arguments like the absence of Jurassic plutons and the dominance of sedimentary lithologies.

Regardless of the origin of these rocks, their age and lithology are well-constrained and represent an important part of the tectonic evolution of Northeast Mexico. Likewise, the La Boca Formation is a lateral variation of the Nazas Fm. that is occasionally also found overlying the Nazas Fm. by erosional unconformity (Rubio-Cisneros & Lawton, 2011; Zavala-Monsiváis et al., 2012). It has two informal members that are, in turn, separated by an angular unconformity that ranges from a few degrees (10-20°) to 70° locally in the Huizachal Valley, an angle that increases in the vicinity of rhyolite intrusions (Rubio Cisneros et al., 2011; Rubio-Cisneros & Lawton, 2011). The (1) lower member consists of lapilli tuffs, lava flows, volcanic breccias, and ignimbrites interbedded in greater proportion with volcaniclastics and detritus derived primarily from coeval volcanic rocks that represent deposits from the Nazas volcanic activity. The volcanic component in the La Boca Formation gradually decreases towards the top of the stratigraphic unit. The (2) upper informal member of this formation is mostly red siliciclastic strata. These rocks fine upwards in a conglomerate, sandstone, and siltstone succession (Fastovsky et al., 2005). The reported maximum depositional age (youngest detrital zircon) for the La Boca Formation is 184 -183 Ma for the lower member and 167 Ma for the upper member (Rubio-Cisneros & Lawton, 2011). La Boca Formation and the Nazas Fm. are overlain by the La Joya Formation, a siliciclastic unit with a basal fining upward conglomerate to reddish siltstone and mudstone. It was deposited in continental to a marginal marine environment with subordinate freshwater limestone and is overlain by the upper Jurassic-Paleogene marine sedimentary cover that starts with the Oxfordian Minas Viejas evaporites and or with the Zuloaga Fm. (Padilla y Sánchez, 1985; Rubio-Cisneros & Lawton, 2011; Salvador, 1987). The youngest detrital zircon ages of the La Joya Formation are 166.2 ± 1.9 Ma at the top of this unit in Real de Catorce

(Barboza-Gudiño et al., 2012), and 158.36 ±1.2 in the La Ballena area (Wengler et al., 2019) in Huizachal Valley was bracketed as Callovian in age (Rubio-Cisneros & Lawton, 2011).

From the Late Jurassic to Early Cretaceous, the effects of the progressive drifting stage of the breakup of Pangea combined with extension related to the roll-back of the paleo-pacific plates in the western continental margin, formed a series of marine basins such as the Arperos Basin and the Mesozoic Basin of Central Mexico (Centeno-García, 2017; Martini et al., 2011; Martini & Ortega-Gutiérrez, 2018). The Arperos basin was situated between a west-rifted Late Jurassic magmatic arc (Guerrero Terrane) and mainland Mexico. During the Late Jurassic (Oxfordian ~160 Ma) the extensional setting in the Atlantic system of Mexico triggered a large marine transgression responsible for the accumulation of a ~ 5 km thick marine sedimentary succession in the Central Basin of Mexico(Bartolini et al., 1999; Goldhammer, 1999; Gray & Lawton, 2011; Hernández-Romano et al., 1997.

2.2.2 Oxfordian - Cenomanian Marine Shelfal Carbonates.

The Mesozoic Atlantic rifting system had a deeper influence on the lithology of eastern Mexico, especially in the sediments deposited in the Mesozoic Central Basin during the Oxfordian. Carbonate and siliciclastic successions were deposited in the vicinity of basement highs in continental to coastal deposition environments (La Gloria, Minas Viejas Fm. (Michalzik, 1988; Ocampo-Díaz et al., 2012). The vertical succession continues to mud facies of continental shelf and beach deposits of the Zuloaga Fm. and subsequently the Olvido evaporites. The late Jurassic overall is characterized by marginal marine deposits (coastline and deltas *e.g.* La Casita Fm.) that occasionally change laterally to open platforms and to deep basin facies to the West (La Caja Fm).

In the Early Cretaceous, this region underwent cooling and continuous subsidence(Goldhammer, 1999; Goldhammer et al., 1991; Lehmann et al., 1999). During this time more than 2,000 m of shelfal carbonates were deposited around the Paleo-Gulf of Mexico. Three major continental uplifts made up the paleogeography, The Coahuila Block, The Tamaulipas Archipelago, and the Valles-San Luis Potosí Platform (Figure 2.2).

The depositional control that the basement highs exerted in this area was very influential in the Early Cretaceous. In the beginning (Berriasian-mid Hauterivian) a widespread carbonate sequence with an argillaceous component was deposited on open platform facies in a uniform subsidence regimen, the Taraises Fm. (Goldhammer, 1999; Michalzik, 1988, 1991) .

In Mid-Hauterivian up to the end of the Albian two significant periods of carbonate platform development took place. 1) In this period up to the Middle Aptian hemipelagic carbonates of the Tamaulipas Inferior Fm. were deposited in the deep basins surrounding the contrasting basement highs. Simultaneously, Peritidal shelf-lagoon facies of the Cupido formation developed in the Coahuila Block (Goldhammer & Johnson, 2001).

Promptly In Middle to Late Aptian the La Peña Fm. was deposited, a flooding transgressive sequence made up of argillaceous sediments (Shales and laminated foraminiferal mudstones) that divides the two phases. This formation is widespread and outcrops throughout most of the study area. This event marked the peak of flooding and the end of the (1) Cupido platform phase and the start of (2) the Coahuila platform (Lehmann et al., 1999).

2) After the La Peña flooding, carbonate platform development resumed at a higher sea level, retreating the Coahuila ramp's margin further north. By Middle Albian, the evaporitic lagoon on top of the Coahuila Block (Acatita Formation) was replaced by a fully developed carbonate platform system the Aurora Fm. This formation’s subtidal facies grade seaward into hemipelagic

mudstones of the Tamaulipas Superior Formation in the deep basin facies (Eguiluz y de Antuñano, 2022).

Afterward, the Cenomanian Cuesta del Cura Fm. was conformably deposited on top of the Tamaulipas superior in the Monterrey region and interdigitates with it in the Sierra de Parras area. The Cuesta del Cura formation marks the end of the intracratonic marginal marine basin sedimentation. This formation shows explicit evidence of tectonic instability, like, intraformational breccias, disarmonic folds, faults, and onlaps (Eguiluz, 2021; Guerra Roel, 2019). This time-lapse casually correlates in age with angular unconformities in the west (Arperos Basin) that imply an active tectonic setting.

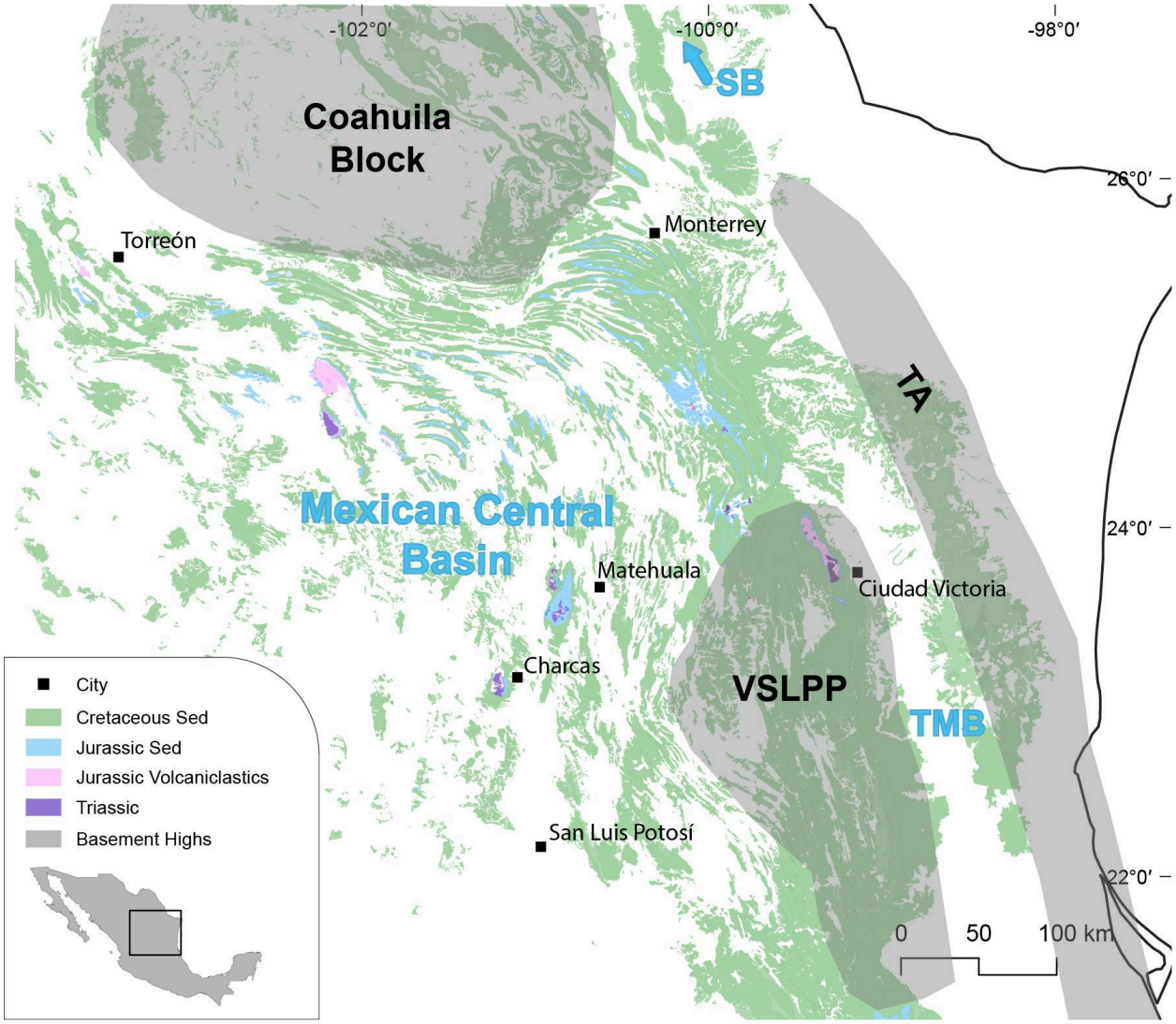

Figure 2.2. Map section of NE Mexico with main geological elements. Carbonate platforms and major basins. SB= Sabinas Basin; TMB = Tampico Misantla Basin; VSLPP = Valles San Luis Potosí Platform; TA = Tamaulipas Arch (Modified from Fitz-Diaz et al., 2018).

2.2.3 Cenomanian - Maastritian Foreland Basin

The closure of the Arperos basin was an effect of the change in the subduction angle and relative motions between the overriding NA plate and the trench, this also caused the accretion of the Guerrero composite terrain during Albian-Cenomanian time (Boschman et al., 2018; Centeno-García et al., 2005; Martini et al., 2011). Relative motions between the overriding plate and the trench generated a change in (Boschman, et al., 2018 b; Boschman, et al.,

2018 a) field causing extensive horizontal shortening and basin inversion resulting in the development of the Mexican Fold and thrust Belt this event was recorded in the succession of the nascent foreland basin of NE Mexico.

By the end of the Cenomanian, there was a significant change in the sedimentation patterns in the Mexican Central Basin, after the deposition of the Carbonate platforms and the Cuesta del Cura Fm. a rhythmic succession of turbidites signal the beginning of the foreland basin successions. In the southern part of the Parras Transversal Sector (Figure 2.1) Erosion during the mountain building process generated deposits corresponding to the Indidura, Concepcion del Oro, Caracol, and Parras formations. As for the Monterrey trough area in the east Agua Nueva, San Felipe, and Mendez formations were deposited (Figure 2.3). The deposition of these turbiditic sequences was diachronic from W to E in function of the advancement of the tectonic wedge into the foredeep up to Maastrichtian time (Ocampo-Díaz et al., 2016).

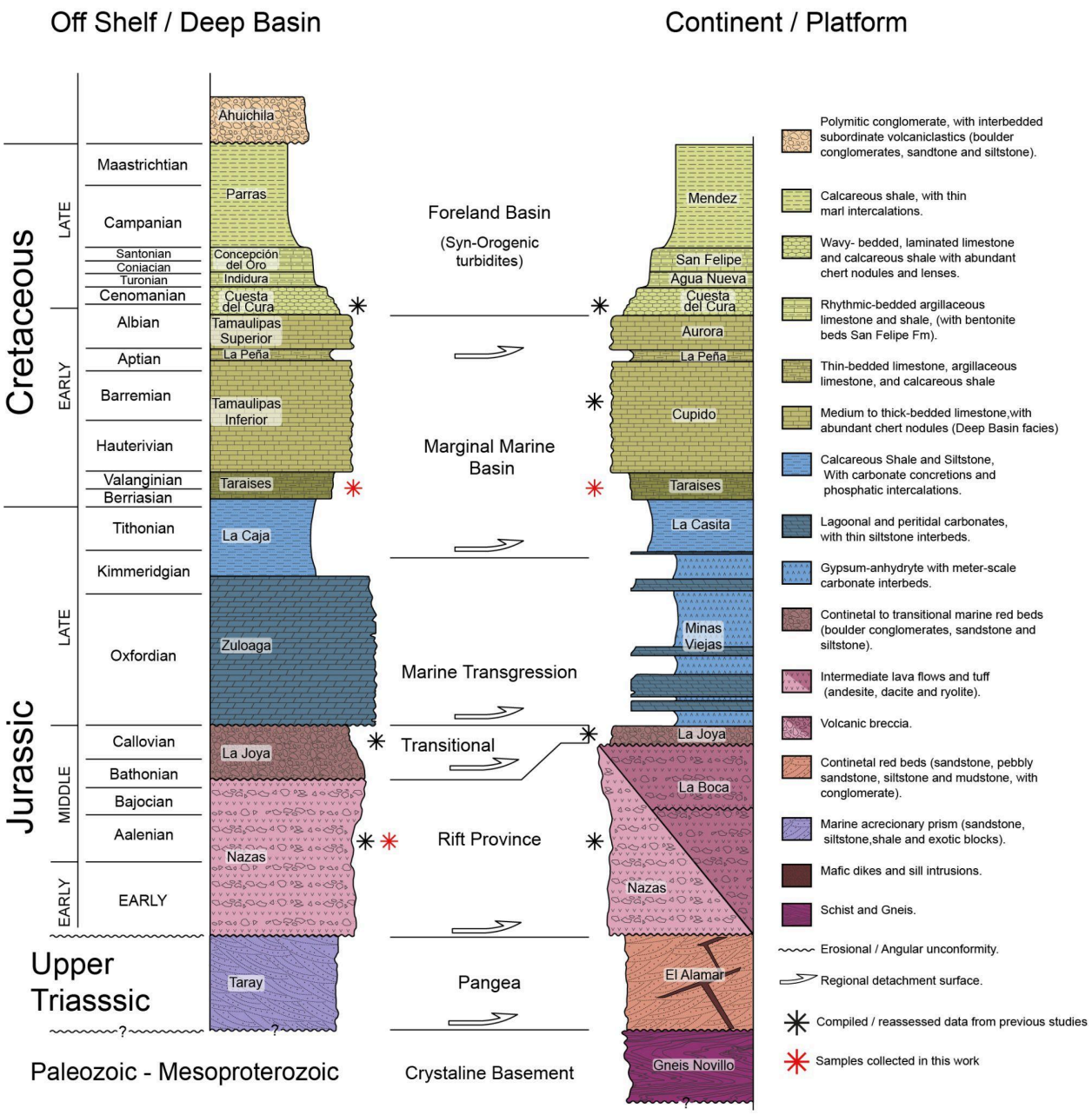

Figure 2.3 Stratigraphic columns that show the correlation between Basin and Platform facies (Modified from (Goldhammer & Johnson, 2001; Michalzik, 1988; Ocampo-Díaz, 2011; Ramírez-Peña, 2017) . Arrows portray weak stratigraphic levels where detachment faults have developed. Red asterisks show stratigraphic levels where samples where collected for this thesis.

2.3 Shortening ages

In North America, the change to flat-slab subduction and the subduction of oceanic plateaus during the cretaceous (Boschman, et al., 2018 a; Dickinson & Snyder, 1978; Liu et al., 2010)generated significant horizontal crustal shortening on the overriding North American plate. Inverting the existing basins with a generalized thrusting vector to the E in the western margin of the continental US and Mexico.

In Mexico, the Mexican Fold and Thrust Belt bears an age of regional folding(Fitz-Díaz et al., 2014, 2016; Gutiérrez-Navarro et al., 2021; Williams et al., 2021), syntectonic magmatism (Teyra and Peñuelo plutons; Ramírez-Peña et al., 2019; Ramírez-Peña & Chávez-Cabello, 2017) and synorogenic clastic sedimentation (Concepción del Oro Formation; (Fitz-Díaz et al., 2018 and references therein; Ocampo-Díaz et al., 2016) to be bracketed between 93 and 42 Ma.

Two main shortening styles of deformation are evident in the MFTB. The thin-skinned deformation style, that is recorded to culminate by the end of the Cretaceous. And afterwards, Thick-skinned structures developed in localized areas, crosscutting the previous folds. The transition from Thin-Skinned to Thick-skinned is documented in several localities, at relatively the same time. 1) San Julián- Concepción del Oro: post-Paleocene, Late Eocene (Ramírez-Peña, 2017; Ramírez-Peña et al., 2019). 2) Potosi Uplift: Eocene (Williams et al., 2021). 3) Real de Catorce: Eocene (Gutiérrez-Navarro, et al., 2021).

2.4 Large scale Tectonic Setting: What We Know and what we don't

The Tectonic evolution of Mexico has been a well-discussed subject due to several controversies. 1) The overlapping of South America with the Mexican

mainland during the reconstruction of Pangea. 2) The kinematics and origin of the Guerrero composite terrain. 3) Distribution of the Jurassic siliciclastic-volcanic rocks in Mexico. Primarily 3 different hypothetical scenarios have been proposed, and each one explains the evolution and distribution of the components of the Sierra Madre Oriental (Figure 2.4).

1)Double arc setting with double subduction of the “Mezcalera” plate (East and West dipping) with a convex trench to the east that generates the volcanism of the Nazas Province, and the western subduction generating the volcanism of the Guerrero terrain (oceanic arc)(Dickinson & Lawton, 2001). This scenario implicitly states that the distribution of the volcaniclastics of the Nazas province is a result of the trench trend and location.

2) A single subduction close to the continental margin that generates the volcanism of the Guerrero terrain that later becomes rifted from the Mexican mainland to posteriorly accrete back to the continent by early late Cretaceous, and at the same time some authors consider the Nazas province as an extensional back-arc rift volcanic system of isolated transtensional basins related to the Pangea breakup extension (Boschman, Molina Garza, et al., 2018; Busby & Centeno-García, 2022; Martini et al., 2011, 2013).

3) A similar configuration of subduction with a set of kilometric transcurrent faults that displace the Jurassic rocks from somewhat a North-South trend volcanic arc to their present position (T. H. Anderson, 2005; T. H. Anderson & Schmidt, 1983; Molina-Garza & Iriondo, 2005).

These three models, however, either assume or disregard that the posterior deformational events minorly affected these lithologies and only displaced the overlying sedimentary cover.

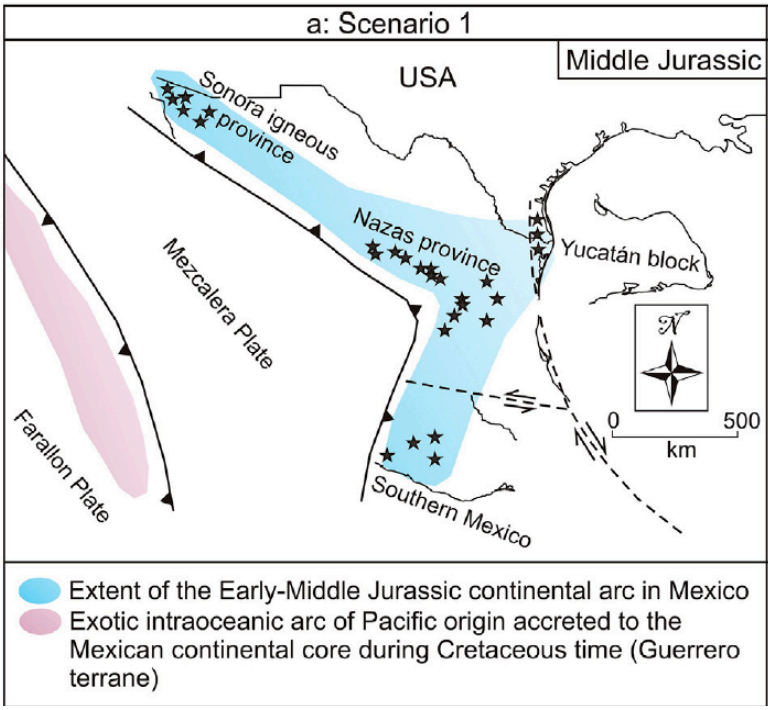

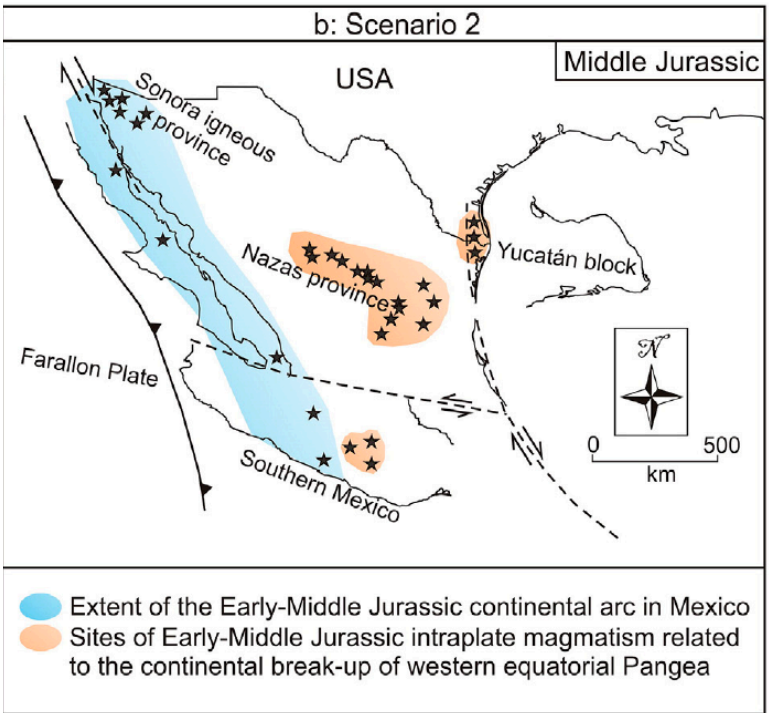

★ Exposure of Lower and Middle Jurassic igneous and metaigneous rocks with arc-signature

Major transform faults producing the displacement of southern Mexico, Yucatán, and Baja California to their present-day positions during Late Mesozoic and Cenozoic times

Subduction boundary

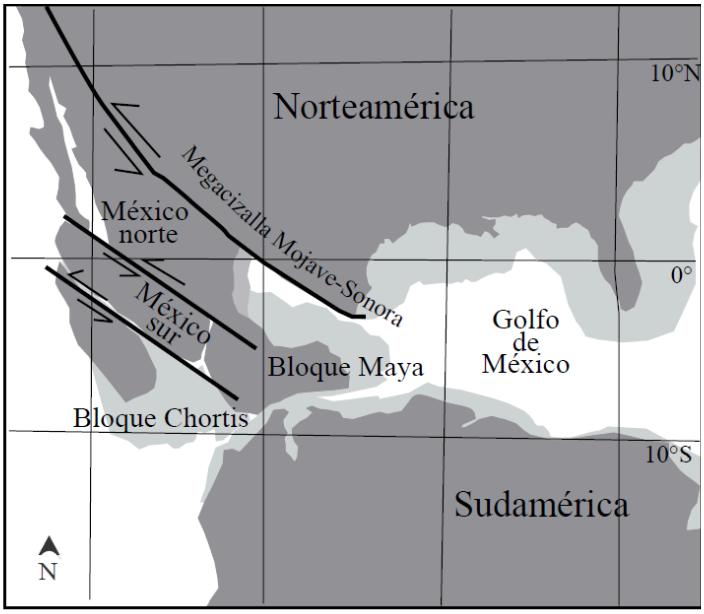

Figure 2.4 Hypothetical models explaining the tectonic evolution of Mexico and its inferences on the distribution of the Jurassic red beds. A) involves a convex trench to the NE (Taken from Martini & Ortega-Gutiérrez, 2018). B) shows a near N-S trench set up (Taken from Martini & Ortega-Gutiérrez, 2018). C) Shows a set of regional transcurrent faults that displaced the continent to its present day position (Taken from Molina-Garza & Iriondo, 2005).

Chapter 3

Methodology

-Hay un tiempo señalado para todo, y hay un tiempo para cada suceso bajo el cielo:
-Un tiempo de lanzar piedras y un tiempo de recoger piedras [...]

-There is an appointed time for everything, and there is a time for every event under heaven:
-A time to cast stones and a time to gather stones [...]

(Ecclesiastes 3:1 & 3:5)

To shed light on the kinematics of the Sierra Madre Oriental Fold and Thrust Belt, three techniques were used, Rock Magnetic Properties, Paleomagnetism, and Joint analysis. Additionally, to complement the rock magnetics analyses SEM imagery of representative samples was applied.

3.1 Paleomagnetism and Rock Magnetism

A rock's natural remanent magnetization (NRM) refers to its inherent magnetic signature. This magnetization can be imprinted during rock formation, resulting in a primary magnetization, or it can develop later through geological processes, giving rise to a secondary magnetization. These magnetic imprints, preserved in rocks, capture snapshots of the Earth's magnetic field, either from their original formation or subsequent events, offering valuable insights into the planet's magnetic history. Rock magnetism is the study of magnetic properties in rocks, controlled by magnetic minerals (e.g. magnetite, hematite, pyrrhotite...). These minerals can acquire and retain a record of the Earth's magnetic field at the time of rock formation or alteration.

The Geocentric Axial Dipole (GAD) hypothesis explains that when averaged over extensive geological timescales, the Earth's geomagnetic field resembles a simple dipole aligned with the rotational axis (e.g.Gubbins, 2007; Hospers, 1954). This hypothesis is fundamental for paleomagnetic studies and its assumption has been crucial for analyzing paleomagnetic data. However, it has been proven that the time-averaged geomagnetic field may also encompass small and yet consistent non-dipolar components (e.g. McElhinny, 2007). Nonetheless, the GAD model is currently a reasonable first-order approximation for the time-averaged field at least for the past 400 Ma (McElhinny, 2007). Paleomagnetism uses this magnetic signature to study the Earth's ancient magnetic field as recorded in rocks, sediments, and

archaeological materials. This field reveals critical information about the Earth's core behavior and magnetic polar wandering including geomagnetic reversals, and it has been instrumental in the development of plate tectonics (Irving, 1988).

When rocks contain ferromagnetic minerals they carry an NRM that may be the result of one or several processes of magnetization. From the NRM, the magnetic component identified in a rock or set of rocks that is distinctive due to its stability and frequency is referred to as the ChRM. Isolating ChRM or other components requires stepwise demagnetization lab procedures that are destructive -i.e. The original NRM can not be restored, and therefore prior knowledge about the rock magnetic properties helps to develop laboratory strategies that increase the chances of a successful isolation of the ChRM and save operation time and resources.

3.2 Sampling Strategy

To constrain the kinematics of the Sierra Madre Oriental in space and time the sampling campaign was divided into two subsets. 1) Samples from the Early Jurassic volcaniclastic Nazas Fm., and 2) from the Early Cretaceous marine Taraises Fm. The sampled formations were selected because of widespread occurrence along the curved belt (Taraises Fm.) and their importance in deeper crustal levels (Nazas Fm.). Structurally the Nazas, La Joya, and La Boca Fm. represent a boundary where the mechanical differences of these rocks allowed for a regional detachment from the overlying Oxfordian marine lithologies. This regional decollement separates the Jurassic volcaniclastics, from the overlying marine sedimentary cover. This sampling strategy covers these two elements to investigate the kinematics of the Sierra Madre Oriental.

For group 1 a total of 256, 2.5 cm in diameter core samples were collected with a gas-powered drill. They were oriented with a Pomeroy orienting fixture and a Brunton Pocket Transit compass. In some cases oriented blocks were collected and later drilled in the laboratory. All the samples from group 1 were collected in the San Julian Uplift. The San Julian Uplift is an exhumed basement block whose geographical location is of great importance to this investigation. This locality is a key complement to the previous paleomagnetic studies carried out in the base lithologies of the SMO (Nova-Rodríguez, 2016; Rodríguez-Parra, 2020).

In group 2 a total of 671 cores were collected from 23 anticlines of the sedimentary cover in the Mexican Fold and Thrust Belt following the trace of the Sierra Madre Oriental (Figure 2.1). Additionally, ~40 joint measurements in each locality were taken (see Engelder & Geiser, 1980; Pastor-Galán et al., 2011) for a total of +1200 measurements (Digital Annex 1). All samples were taken from the Taraises formation since its broad distribution, timing of deposition and deformation are optimal to constrain the orocline kinematics. Localities were coded as acronyms from their anticline name followed by a number that indicates the limb (Digital Annex 1).

3.3 Sampled Localities

3.3.1 *San Julián Uplift (24.837°N, -102.174° E)*

The largest outcrop of the Nazas formation is located in north central Mexico and is part of the San Julian Uplift. This crustal block is the result of an Eocene-Oligocene thick-skinned tectonic event that uplifted the volcanic rocks and volcaniclastics of the Nazas, and la Joya Formations (Guerra-Roel, 2019; Ramírez-Peña, 2017; Ramírez-Peña & Chávez-Cabello, 2017). The high angle reverse faults cut the previous structures and trend of the Cretaceous

'thin-skinned' event (Figure 2.1 A). In this locality, the Nazas Fm. represents the Nazas Province, which is intruded by the Caopas laccolith. Here the Nazas Fm. shows a succession of siliciclastic sediments interbedded with subordinate lava flows, ignimbrites, tuff, and volcanic breccias of andesitic to rhyolitic compositions, also dynamic foliation and low metamorphic grade of greenschist facies with chlorite are present (Figure 3.1 A, B, E, and F). Crystallization ages in this locality are 174 ± 2 Ma (zircon U-Pb Ramírez-Peña, 2017). The Caopas laccolith is a hypabyssal body of intermediate composition and porphyritic texture, and in its upper parts shows evidence of dynamic metamorphism (porphyroblasts and mineral lineation Figure 3.1 C & D). U-Pb zircon age for this intrusion yielded 165 ± 3 Ma (Gómez-Torres et al., 2025; Ramírez-Peña, 2017). In the San Julian Uplift, 256 samples were collected: Mina San Miguel (MSM), Nazas North (ALI, NRN), and the Caopas hypabyssal body (MIC, MIR, MIRN). The samples of MSM and sites MIC1, 2, and 3 of the Caopas body were drilled on site (10-15 samples per site). MIC4 – MIC7 were collected as oriented blocks (one per site) and later drilled in the lab extracting four cores from each block. In the MSM and Nazas North localities, poor outcrop exposure of the lava flow succession and their boundaries, with their thickness (~30 m per flow), weathering, and compositional and textural similarities among flows made it difficult to identify individual flows. In the Mina San Miguel locality, an anticline with a plunge/trend of 10°/142° was sampled, near the eastern border of the San Julián Uplift. The structure is oblique to the main east-west trend of the structures in the Transversal Sector of the Sierra Madre Oriental (Figure 2.1 A).

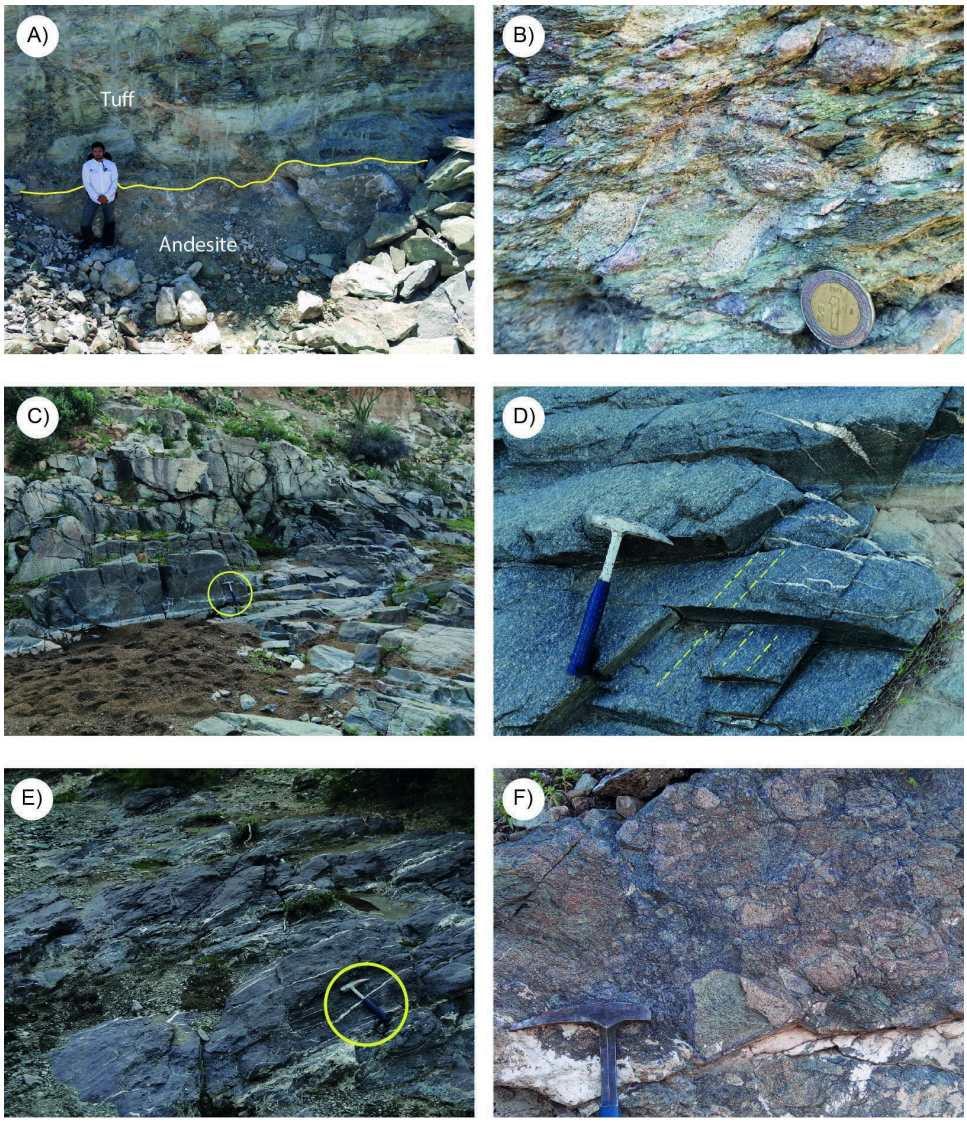

Figure 3.1 Photographs of representative sampling sites of the San Julian Locality. A), B) Andesite overlaid by tuff at the MSM locality. C), D) Caopas laccolith sampling site (Granodiorite), D) shows mineral lineation, E), F) Andesite flows and volcanic Breccias of the Nazas north area. Yellow circle rock hammer for scale.

3.3.2 *Taraises Formation*

Out of the several formations that are part of the sedimentary cover the Taraises formation possesses the best qualities to obtain the information required to perform a paleomagnetic analysis properly. This formation is

Berriasian-Valanginian of age (Figure 2.3) and its outcrops are located in the cores of the majority of the anticline structures across the Sierra Madre Oriental. This marks a broad geographical distribution and timing just before the development of this Fold and Thrust Belt. Approximately ~13 cores were sampled at different stratigraphic levels of the Taraises formation in each limb of every anticline (Figure 3.2), defining two localities per anticline (Figure 2.1 red points) to perform fold tests. The sampling of this formation represents the totality of group 2.

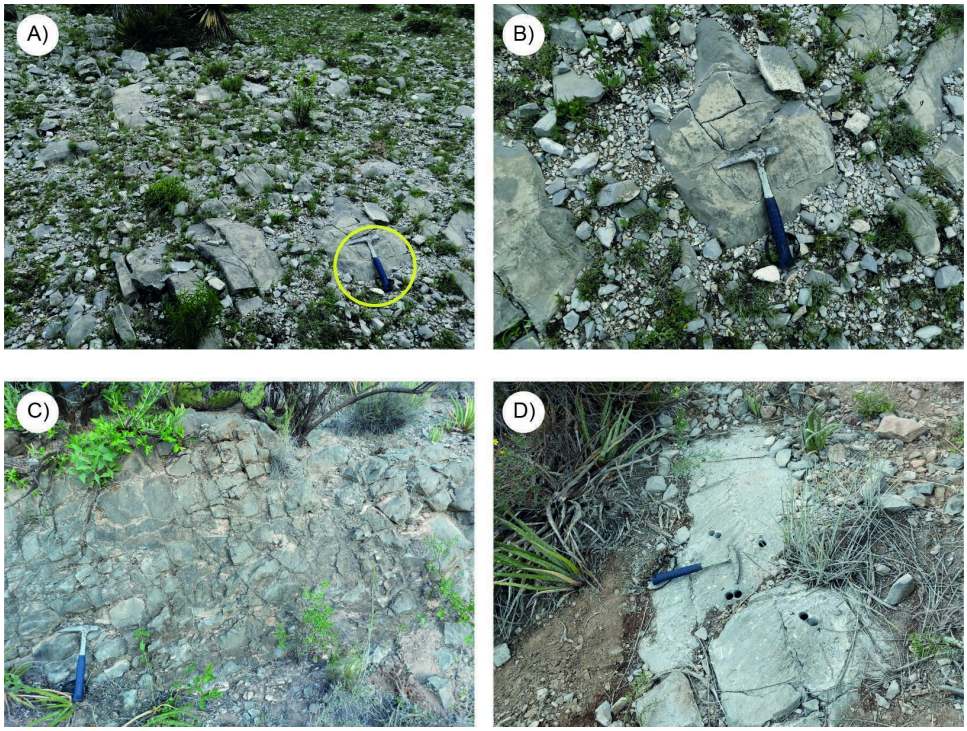

Figure 3.2 Photographs of representative sampling sites of the Taraises formation. These show four different localities with homogenous rock characteristics. A) Tanque del Huerfano locality (TDH). B) La Carbonera locality (LC). C) Mesa de González (MDG) locality and D) Bore holes in the Noria del Cinco locality (NDC). Rock hammer for scale.

3.4 Laboratory work

The Rock Magnetism and Paleomagnetism analyses of the Igneous samples were carried out at the Paleomagnetism and Rock Magnetism

Laboratory of the Instituto de Geociencias, Universidad Nacional Autónoma de México (UNAM, Querétaro; Figure 3.3). The Curie curves were measured in an in-house built horizontal translation type Thermomagnetic balance with a sensitivity of approximately 5 x 10^{-9} Am^2. When the magnetic properties tests were carried out, it was evident that some samples possessed low amounts of magnetic material. The tests were carried out on concentrates separated using hand magnets. Each experiment was executed with 300 to 400 mg of ground sample for each experiment.

The Curie balance was programmed to continuously heat the sample to 700 °C and gradually cool to room temperature at heating and cooling rates of approximately 10 °C min^{-1}. The IRM and the Hysteresis loop procedure were carried out using an in-house built impulse magnetizer (fields up to 5 T) and a Princeton Measurements Corporation Micromag model 2900 with two Tesla magnets, noise level 2 × 10^{-9} Am^2. The Micromag IRM tests were carried out by applying a field of 1 T in 10 mT increments at room temperature. In the hysteresis loops sample mass ranged from 40 to 50 mg and a maximum field of 1 T was applied in 20 mT increments on an average time of 600 ms using a P1 phenolic probe. The magnetization was measured in a JR6 spinner magnetometer from AGICO and demagnetized using thermal stepwise demagnetization.

The magnetically weaker samples (limestone) of group 2 were analyzed in the Paleomagnetic Laboratory 'Fort Hoofddijk, Utrecht University, The Netherlands (Figure 3.3). Here Curie curves were acquired from a translation type curie balance developed at this Laboratory. This balance manages a working temperature between room and 900 °C with a noise level of 2 x 10^{-9} $Am^{2,}$ which is particularly efficient at thermomagnetic analysis of weakly magnetic material (T. a. T. Mullender et al., 1993). Runs included heating and cooling cycles to progressively higher temperatures in each heating step to

distinguish between thermochemical alteration and genuine magnetic behavior.

Figure 3.3 Laboratory equipment used for demagnetization procedures, In Utrecht University Netherlands (left) and Instituto de Geociencias, UNAM Querétaro, México (right).

Paleomagnetic directions were acquired using stepwise progressive thermal demagnetization and alternating field demagnetization. The thermal demagnetization procedure was done manually with a "2G" SQUID magnetometer and a furnace capable of temperatures up to 700 °C. Alternating field demagnetization was carried out with an automated cryogenic magnetometer equipped with horizontal pass-through ''2G'' DC-SQUID magnetometer, an ''in-line'' alternating field (AF) demagnetization, a direct-current bias field coil along the coaxial AF demagnetization coil and a long pulse-field coil for the acquisition of isothermal remanent magnetization (IRM) and an automated pneumatic pick-and-place-unit developed in Fort Hoofddijk (Mullender et al., 2016).

In addition, Anisotropy of Magnetic Susceptibility (AMS) was used as a proxy for describing deformation in slightly deformed rocks (e.g., (Parés, 2015; Weil & Yonkee, 2009). The AMS ellipsoid is represented by its three orthogonal axes ($k_{max} > k_{int} > k_{min}$) and its shape is dependent on several features, for example, mineral grain orientation, compositional layering, crystallographic orientation of individual minerals, distribution, and microfractures size, and the shape and size of individual grains (e.g., Butler, 1992; Tarling & Hrouda, 1993). The analyses of group 1 were conducted in a model KLY-3 Kappabridge in the Instituto de Geociencias, Paleomagnetism and Rock Magnetism Laboratory of the Universidad Nacional Autónoma de México (UNAM) in Juriquilla Querétaro, México. Group 2 (348 samples ~14 per anticline) were analyzed using an AGICO MFK1-FA susceptometer (nominal sensitivity 2 × 10–8 SI) in Utrecht University. AMS ellipsoids were represented in equal-area projections and shape parameter graphs both Flinn (1962) and Jelinek (1981).

As a means of verification, several samples underwent Scanning Electron Microscope (SEM) analysis with a model TM-1000 Hitachi equipped with energy-dispersive X-ray spectroscopy (EDS: Oxford). This procedure was performed in the Laboratory of Crustal Fluids in the Instituto de Geociencias, Universidad Nacional Autónoma de México (UNAM, Querétaro).

3.5 Joint Analysis

Fractures or joints are planar or subplanar discontinuities in rocks that form under brittle deformation process. Three types of fractures are defined in regards to their relative movement (Figure 3.4; Anderson, 1951).

- Tensile Fractures (Mode I): These fractures portray movement that is perpendicular to the fracture plane.

- Shear Fractures (Mode II): displacement is parallel to the fracture plane.
- Tear Fracture (Mode III): displacement is parallel both to the fracture plane and to the edge of the crack.

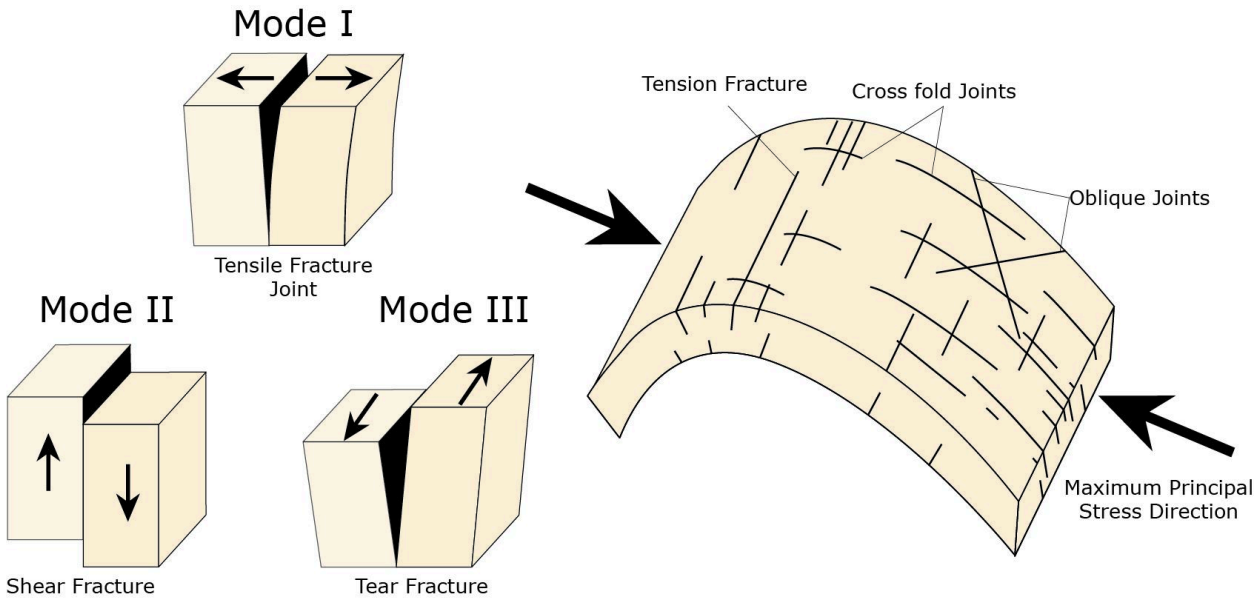

Figure 3.4 Ways of Fracturing according to Anderson (1951).

Fractures with similar orientation and morphology that appear systematically are considered families or joint sets (Figure 3.4). Several sets can occur at the same place with no apparent interaction and conform joint systems.

Joint sets of families with broad distributions are known to be the result of regional stress fields, as for the ones found in small areas or in the vicinity of structures (*e.g.* Plutons or Diapirs) are attributed to local stress fields (Engelder & Geiser, 1980)

Initial joints are parallel to the maximum principal stress. These structures have been found to be a useful tool in tectonic reconstructions (Engelder & Geiser, 1980; Gross et al., 1995; Turner & Hancock, 1990).

Joint systems within rocks subjected to compressional regimes are particularly sensitive to the syn-kinematic stress fields present during deformation (Whitaker & Engelder, 2005). Numerous studies have shown that well-developed tectonic joint sets can serve as reliable indicators of the lithospheric stress field orientation (e.g.,(Pastor-Galán et al., 2011; Whitaker & Engelder, 2006), with examples spanning various regions, such as the Ouachita salient (Whitaker and Engelder, 2006), the Appalachian plateau (Engelder & Geiser, 1980), the Idaho-Wyoming salient (Yonkee & Weil, 2010 a), the Variscan belt in Wales (Dunne & North, 1990), the Pyrenees (Turner & Hancock, 1990), and the Cantabrian Orocline (Pastor-Galán et al., 2014). In certain cases, joint patterns may record cumulative deformation histories, leading to the coexistence of multiple joint sets formed under different temporal stress fields.

To this matter, the existence of more than one joint set in a system reveals information about the tectonic episodes in the geological history of said system, mainly because a joint cannot propagate on a “free” medium (e.g. a discuntiniuty or previous fracture). Ideally this allows us to establish a relative chronology between said systems. For example, If a given joint set is disrupted in a repetitive or systematic way by another joint set it can be determined that the second set predates the first. Consequently, when interpreting tectonic history from joint patterns, it is crucial to consider the potential for successive joint sets (Dunne and North, 1990; Engelder and Geiser, 1980). As tectonic complexity increases, distinguishing between systematic joint patterns and determining whether they reflect regional or local stress field changes becomes increasingly difficult (Fischer & Jackson, 1999).

To study and constrain the stress field in wich the curvature of the Sierra Madre Oriental formed, a spacial analisis of the joinsets present in the study area was conducted. To identify joint sets, 40 measuremets were taken per

folded structure, divided in 2 stations (one per limb). The measurements were taken only on fractures present in the Taraises Fm. giving special attention to crossfold joints. The resulting data was analized in the stereonet software and graphed in rose diagrams. The joints were classified according to their orientations.

3.6 Previous Paleomagnetic studies: the Sierra Madre Oriental

A thorough review of the literature of the Sierra Madre Oriental was performed as the first approach to the problem. Paleomagnetic studies in the curved sector of the Sierra Madre Oriental are not numerous. After reviewing the published literature only eleven research documents containing paleomagnetic directions were identified (Belcher, 1979; Clement et al., 2000; González-Naranjo et al., 2012; Gose et al., 1982; Kleist et al., 1984; Molina Garza, 2004; Nemkin et al., 2019; Nova-Rodríguez, 2016; Nowicki et al., 1993; Rodríguez-Parra, 2020; Warrior, 2008). The studies were focused on Mesozoic to Oligocene rocks (See Table 3.1). Some works are not mentioned because their data is included in the already-mentioned studies. Seven of these studies reported vertical axis rotations of variable magnitudes (Clement et al., 2000; Gose et al., 1982; Kleist et al., 1984; Nemkin et al., 2019; Nova-Rodríguez, 2016; Rodríguez-Parra, 2020; Warrior, 2008). However, some were considered the result of local tectonics (e.g. Warrior, 2008; Nemkin et al., 2019) or spurious (e.g. Clement et al., 2000). Only two studies disclose data at the specimen level (Nova-Rodríguez, 2016; Rodríguez-Parra, 2020). These two studies were re-analyzed and re-interpreted. The rest of the studies could not be faithfully re-interpreted, and therefore the provided statistical parameters were used (Table 3.1). The studies of Nova and Rodíguez-Parra were processed from the raw metadata made available from the authors, and the remaining studies that provided site or locality averages were re-processed and re-interpreted in chapter 4 under the following guidelines.

The presented data sets from previous works were put under scrutiny in order to evaluate the reliability and trustworthiness of each of the presented data sets, for this, a standard of quality criteria was established. This criteria aligns with the most recent paleomagnetic consensus for contemporary paleomagnetic studies(Gerritsen et al., 2022; Meert et al., 2020; Sapienza et al., 2023). Sites/localities were discarded when one of the following criteria was not met: (1) Specimens stepwise demagnetization; (2) principal component analysis of at least 4 points to define directions; (3) Properly documented field tests were provided and structural data (fold, conglomerate, or baked contact test) to establish the magnetization's relative timing; (4) $k > 40$ for sites above three specimens (anything below may not represent an averaged single spot reading); (5) A minimum of seven independent spot readings of the geomagnetic field in each locality; (6) Localities show k between 10 and 85 (higher k values are likely to represent single spot readings, on the other hand poor concentration parameter k may be indicative of structural or magnetization problems). To re-evaluate the effectiveness of the field tests provided by the authors or to average out repetitive localities showed consistent values, in some cases, parametric resampling was performed (Deenen et al., 2011; Koymans et al., 2016).

In 1993, Nowicki et al. sampled Lower Cretaceous limestones near Torreón, Coahuila in the Sierra Madre Oriental. The results show four localities, however, only two passed the criteria (Localities 2 and 4; Figure 2.1).) and showed evidence of remagnetization (failed fold test; Table 3.1). Clement et al. (2000) reported sampling in a series of localities, but only two of them are located in the Sierra Madre Oriental. These two localities show positive fold tests and reversals, by these characteristics they are considered of primary nature (ca. 130 Ma). Although the structural data provided in this study would not be enough to pass the reliability criteria, structural data from the sampled

outcrops was retrieved from another study in the area (Chávez-Cabello et al., 2011). The localities from Clement et al. (2000) that passed display near opposite declinations with similar inclinations. With the information from Chávez-Cabello et al. (2011), It was evident that the difference in the rotation present in the Santa Rosa locality results from a local strike-slip fault reported in this area. Nemkin et al. (2019) report sampling several localities in outcrops of the Cretaceous Cupido Fm. along the trace of the Monterrey salient of the Sierra Madre Oriental. The authors interpreted the magnetizations as post and syn-folding in origin. However, in some of the cases fold axes plunge steeply, this adds errors to the result of the fold test and the declinations. From this extensive dataset, four localities filled the requirements of the criteria. To circumvent the previous interpretations and since the structural data was enough, the directional data was parametrically resampled (Tauxe, 2010; Tauxe & Watson, 1994) and carried out the fold tests (Tauxe and Watson, 1994) again. No significant changes were found except for the fold test containing localities 4 and 6 from Nemkin et al. (2019). This test was better interpreted as post-folding rather than 35% syn-folding. The differences in declination between both analyses were not significant (Table 3.1).

Table 1. All Compiled data from previous paleomagnetic studies in the Sierra Madre Oriental.

REFRENCE	Formation	Locality	AGE	Coordinates		Demag	Ns	N	Geographic		Tectonic		a95	k	Estimated Age Magnetization	SS (RHR)	Field Test		Kmax	D	I	% unfolding	NOTES
				Lat	Long				mDec	mInc	mDec	mInc											
Nemkin et al., 2019	La Peña-Cupido	1 Mty Salient	Cretaceous	24.75	-99.79	~ 500°	8	8	223	-23	217	-74.8	3	349.4	47.5 Ma	316°/52°							
	La Peña-Cupido	2 Mty Salient	Cretaceous	24.73	-99.86	~ 500°			aotic decay No Data Availa						47.5 Ma								k value is not betwen 10 and 85
	La Peña-Cupido	3 Mty Salient	Cretaceous	24.73	-99.94	~ 500°	6	8	305	-16	347	37.5	5.6	146.7	47.5 Ma	60°/124.7°							
	La Peña-Cupido	4 Mty Salient	Cretaceous	24.91	-99.94	~ 500°	7	8	189	-23	152	-41	6.4	89.5	47.5 Ma	333°/56	4/6 Fold Test	post- folding	82	181	-33	35	Post folding after parametrically resampled.
	La Peña-Cupido	5 Mty Salient	Cretaceous	24.91	-99.92	~ 500°	7	8	166	-45	193	-2.6	7.4	67.6	47.5 Ma	143°/65°							
	La Peña-Cupido	6 Mty Salient	Cretaceous	24.91	-99.92	~ 500°	7	8	194	-26	120	-55.1	9.7	40.1	47.5 Ma	320°/72°	5/6 Fold Test	sin folding	50	182	-39	25	The folds plunge too steeply and the unfolding percentage may not be representative this may add spurious rotations.
	La Peña-Cupido	7 Mty Salient	Cretaceous	24.93	-99.90	~ 500°	5	8	122	0.3	181	-35.5	19.7	16.1	47.5 Ma	161°/115°	4/7 Fold Test	sin folding	35	162	-40	80	
	La Peña-Cupido														47.5 Ma		5/7 Fold Test	sin folding	21	153	-50	70	
	La Peña-Cupido	8 Mty Salient	Cretaceous	25.04	-99.99										47.5 Ma								
	La Peña-Cupido	9 Mty Salient	Cretaceous	25.04	-99.99				aotic decay No Data Availa						47.5 Ma								The fold plunges too steeply and the unfolding percentage may not be representative this may add spurious rotations.
	La Peña-Cupido	10 Mty Salient	Cretaceous	25.04	-99.99	~ 500°	5	7	172	-52	118	-14.4	16.7	21.9	47.5 Ma	348°/74°	10/11 Fold Test	sin folding	24	139	-36	40	
	La Peña-Cupido	11 Mty Salient	Cretaceous	25.04	-99.99	~ 500°	6	8	114	-18	164	0	10.7	39.9	47.5 Ma	135°/138°							
	La Peña-Cupido	12 Mty Salient	Cretaceous	25.49	-100.36	~ 500°	5	8	178	-30	72.1	-64.7	11.1	48.8	47.5 Ma	290°/74°							Ns < 7
	La Peña-Cupido	13 Mty Salient	Cretaceous	25.49	-100.36	~ 500°	6	8	164	-60	201	-16	17.4	15.8	47.5 Ma	140°/58°	12-13 Fold Test	sin folding	23	357	49	25	No significant change after after parametrically resampled.
	La Peña-Cupido	14 Mty Salient	Cretaceous	25.55	-100.39	~ 500°	8	8	202	-38	124	-82.3	7.6	54	47.5 Ma	301°/51°							
	La Peña-Cupido	15 Mty Salient	Cretaceous	25.55	-100.39	~ 500°			aotic decay No Data Availa						Chaotic decay No Data Available								
	La Peña-Cupido	16 Mty Salient	Cretaceous	25.65	-100.46	~ 500°	5	9	186	-36	60.9	-59	16.8	21.60	47.5 Ma	297°/78°							Ns < 7
	La Peña-Cupido	17 Mty Salient	Cretaceous	25.65	-100.46	~ 500°	4	8	183	-37	179	44.9	16.6	31.60	47.5 Ma	117°/87°							Ns < 7
	La Peña-Cupido	18 Mty Salient	Cretaceous	25.61	-100.81	~ 500°	5	6	186	9.6	250	65	34	6.00	47.5 Ma	070°/79°							
	La Peña-Cupido	19 Mty Salient	Cretaceous	25.37	-100.30	~ 500°	3	8	357	43.1	271	52.4	45.9	8.3	47.5 Ma	308°/64°	/23 Reg. Fold Te	sin folding	24	292	61	80	k value is not betwen 10 and 85 and spot readings are not sufficient.
	La Peña-Cupido	20 Mty Salient	Cretaceous	25.39	-100.30	~ 500°	9	9	256	37.5	315	51.1	8.3	39	47.5 Ma	117°/54°							
	La Peña-Cupido	21 Mty Salient	Cretaceous	25.39	-100.46	~ 500°	4	8	13.6	-13	4.2	49	42.2	5.70	47.5 Ma	302°/65°							
	La Peña-Cupido	22 Mty Salient	Cretaceous	25.40	-100.25	~ 500°	11	12	241	19.5	304	61.9	9.9	22.30	47.5 Ma	121°/69°							No Field Test
	La Peña-Cupido	23 Mty Salient	Cretaceous	25.39	-100.25	~ 500°	7	8	285	-69	2	-36.3	38	4.10	47.5 Ma	298°/56°							k value is not betwen 10 and 85
	La Peña-Cupido	24 Mty Salient	Cretaceous	25.47	-100.44	~ 500°	5	8	353	-31	339	52	12.5	59.3	47.5 Ma	291°/75°	24/25 Fold Test	Positive	81	338	52	125	No significant change after after parametrically resampled.
	La Peña-Cupido	25 Mty Salient	Cretaceous	25.48	-100.42	~ 500°	5	8	252	8.6	337	52.7	11.4	71	47.5 Ma	129°/79°							
	La Peña-Cupido	26 Mty Salient	Cretaceous	25.39	-100.80	~ 500°	7	7	315	-10	293	47.2	6.2	80.8	47.5 Ma	260°/69°	26/27 Fold Test	Positive	56	288	45	110	No significant change after after parametrically resampled.
	La Peña-Cupido	27 Mty Salient	Cretaceous	25.42	-100.81	~ 500°	6	8	173	9.1	282	41.7	9.1	45.7	47.5 Ma	053°/110°							
	La Peña-Cupido	28 Mty Salient	Cretaceous	25.55	-100.65	~ 500°	5	8	331	-7.6	308	55.9	5.5	155.10	47.5 Ma	266°/67°	28/29 Fold Test	Positive	147	312	57	110	K > 100 on the fold test
	La Peña-Cupido	29 Mty Salient	Cretaceous	25.55	-100.65	~ 500°	6	9	202	17.4	316	57.4	5.3	133.60	47.5 Ma	089°/88°							
	La Peña-Cupido	30 Mty Salient	Cretaceous	25.58	-100.79	~ 500°	8	8	168	-38	199	-71.3	3.4	273.00	47.5 Ma	240°/38°	I/30 Reg. Fold Te	Positive	29	340	72	95	K > 85 at site level.
	La Peña-Cupido	31 Mty Salient	Cretaceous	25.23	-101.03	~ 500°	7	8	300	42.5	215	71.6	7.8	60.60	47.5 Ma	234°/51°	31/32 Fold Test	Sin Folding	38	286	53	30	Ns < 7
	La Peña-Cupido	32 Mty Salient	Cretaceous	25.23	-101.03	~ 500°	3	9	248	55.5	295	4.2	24.6	26.10	47.5 Ma	059°/79°							
	Panalito Ignimbrite	P29	Oligocene	22.40	-101.55	580°-660°	7	9	161	-38	161	-42.5	7.9	59.3	28.5 Ma								
	Panalito Ignimbrite	P30	Oligocene	22.42	-101.59	580°-660°	7	9	162	-37	162	-41.7	4.3	197.9									
	Panalito Ignimbrite	P31	Oligocene	22.49	-101.55	580°-660°	7	10	164	-33	164	-33.3	10.5	34	28.5 Ma								
	Panalito Ignimbrite	P32	Oligocene	22.42	-101.43	580°-660°	7	9	150	-43	150	-48	14.3	18.8	28.5 Ma								
	Panalito Ignimbrite	P34	Oligocene	22.40	-101.68	580°-660°			aotic decay No Data Availa						28.5 Ma								
	Panalito Ignimbrite	P35	Oligocene	22.24	101.16	580°-660°	7	11	161	-24	161	-29.2	7	75.3	28.5 Ma								
	Panalito Ignimbrite	P37	Oligocene	22.23	-101.19	580°-660°	7	11	156	-21	156	-20.8	10.5	34	28.5 Ma								
	Panalito Ignimbrite	P38	Oligocene	22.29	-101.23	580°-660°	6	11	176	-22	176	-22.1	12.9	27.9	28.5 Ma								
	Panalito Ignimbrite	P39	Oligocene	22.29	-101.27	580°-660°	4	9	158	-43	158	-42.7	10.1	83.7	28.5 Ma								
	Panalito Ignimbrite	P40	Oligocene	22.22	-101.21	580°-660°	5	10	160	-35	160	-35	10.8	51.1	28.5 Ma								
	Panalito Ignimbrite	P41	Oligocene	22.23	-101.31	580°-660°	6	10	134	-75	134	-74.5	13.5	25.6	28.5 Ma								
	Panalito Ignimbrite	P42	Oligocene	22.25	-101.30	580°-660°									28.5 Ma								
	Panalito Ignimbrite	P43	Oligocene	22.26	-101.33	580°-660°			aotic decay No Data Availa						28.5 Ma								
	Panalito Ignimbrite	P44	Oligocene	22.32	-101.35	580°-660°									28.5 Ma								
	Panalito Ignimbrite	P45	Oligocene	22.35	-101.34	580°-660°	9	9	150	-45	150	-45.2	8.5	37.6	28.5 Ma								
	Panalito Ignimbrite	P46	Oligocene	22.43	-101.06	580°-660°	6	10	159	-24	159	-24.1	16.3	13.1	28.5 Ma								
	Panalito Ignimbrite	P11	Oligocene	22.41	-101.04	580°-660°	7	9	131	-32	135	-30.3	14.6	18	28.5 Ma								
	Panalito Ignimbrite	P12	Oligocene	22.48	-101.03	580°-660°	7	9	162	-28	166	-23	4.4	189.1	28.5 Ma								
	Panalito Ignimbrite	P13	Oligocene	22.36	-101.05	580°-660°	7	10	158	-35	165	-27	8.8	48	28.5 Ma								
	Panalito Ignimbrite	P14	Oligocene	22.36	-101.04	580°-660°	7	8	153	-31	159	-24.5	3.8	253.2	28.5 Ma								
	Panalito Ignimbrite	P15	Oligocene	22.36	-101.02	580°-660°	7	8	152	-31	158	-24.1	10.9	31.6	28.5 Ma								

Gonzalez Naranjo., et al 2012	Panalito Ignimbrite	P16	Oligocene	22.39	-101.01	580°-660°	7	10	163	-27	167	-18.3	9.1	44.9	28.5 Ma				All accepted localities from this Author were summarized into one direction. The k value criteria here was 40 < k < 100.
	Panalito Ignimbrite	P17	Oligocene	22.46	-101.02	580°-660°	7	9	153	-30	159	-23.6	9.3	43.1	28.5 Ma				
	Panalito Ignimbrite	P18	Oligocene	22.27	-101.12	580°-660°	7	8	161	-28	166	-19.5	10.8	32.2	28.5 Ma				
	Panalito Ignimbrite	P5	Oligocene	22.34	-101.16	580°-660°	7	10	145	-32	-32.4	253	154	3.8	28.5 Ma				
	Panalito Ignimbrite	P6	Oligocene	22.36	-101.16	580°-660°	5	6	132	-35	139	-37.3	48.4	3.5	28.5 Ma				
	Panalito Ignimbrite	P7*	Oligocene	22.35	-101.15	580°-660°	8	8	129	-41	138	-43.4	5.9	89.1	28.5 Ma				
	Panalito Ignimbrite	P8	Oligocene	22.34	-101.12	580°-660°	5	6	157	-37	174	-29.8	6.8	127.5	28.5 Ma				
	Panalito Ignimbrite	P9	Oligocene	22.32	-101.12	580°-660°	5	6	138	-34	148	-32.8	38.4	4.9	28.5 Ma				
	Panalito Ignimbrite	P10	Oligocene	22.32	-101.12	580°-660°	6	8	141	-32	148	-27.8	7.8	74.7	28.5 Ma				
	Panalito Ignimbrite	P19	Oligocene	22.35	-101.13	580°-660°	7	9	139	-47	160	-35.1	14.8	17.6	28.5 Ma				
	Panalito Ignimbrite	P20	Oligocene	22.29	-101.07	580°-660°	5	8	142	-23	154	-23.7	7.9	94.7	28.5 Ma				
	Panalito Ignimbrite	P21	Oligocene	22.31	-101.08	580°-660°	6	9	138	-40	160	-40	11.8	33.2	28.5 Ma				
	Panalito Ignimbrite	P23	Oligocene	22.10	-100.74	580°-660°	7	12	153	-31	167	-25.7	9.1	44.9	28.5 Ma				
	Panalito Ignimbrite	P1	Oligocene	22.14	-100.76	580°-660°	8	10	162	-33	158	-26.5	3.7	219.6	28.5 Ma				
	Panalito Ignimbrite	P2	Oligocene	22.16	-100.83	580°-660°	8	10	163	-27	164	-30.4	3.4	260.4	28.5 Ma				
	Panalito Ignimbrite	P3	Oligocene	22.16	-100.79	580°-660°	9	9	151	-29	153	-26.6	7.1	61.7	28.5 Ma				
	Panalito Ignimbrite	P4	Oligocene	21.96	-100.71	580°-660°	8	11	160	-29	165	-31.3	6.6	104.3	28.5 Ma				
	Panalito Ignimbrite	P24	Oligocene	21.83	-101.09	580°-660°	7	9	163	19	161	22	22.1	26	28.5 Ma				
	Panalito Ignimbrite	P25	Oligocene	21.82	-101.11	580°-660°	4	11	160	-33	165	-26.6	46	8.6	28.5 Ma				
	Panalito Ignimbrite	P26	Oligocene	21.91	-101.17	580°-660°	7	10	147	-28	149	-26.2	8.8	48	28.5 Ma				
	Panalito Ignimbrite	P27	Oligocene	21.82	-101.03	580°-660°	6	10	122	-1.8	122	-2	36.6	4.3	28.5 Ma				
	Panalito Ignimbrite	P36	Oligocene	21.81	-101.03	580°-660°	8	8	169	-33	171	-29.4	9.9	38.1	28.5 Ma				
	Panalito Ignimbrite	P47	Oligocene	21.83	-101.16	580°-660°	8	9	170	-34	170	-33.6	13.5	20.9	28.5 Ma				
	Panalito Ignimbrite	P48	Oligocene	21.83	-101.08				iaotic decay No Data Availa						28.5 Ma				
	Panalito Ignimbrite	P49	Oligocene	21.81	-101.17	580°-660°	5	8	340	36.2	340	36.2	7.3	110.8	28.5 Ma				
	Panalito Ignimbrite	P50	Oligocene	21.82	-100.76	580°-660°	5	8	344	56.6	344	56.6	6.4	143.9	28.5 Ma				
Molina-Garza, 2003	Acatita Valley	1 Delicias	Norian	26.54	-103.03	590°	4	8	Little to no diference with correction with overlying SS data		350.6	-5.4	12.2	57.9	218 Ma	Baked contact test. Paleozoic strata carries (insitu) directions nearly identical to these Triassic Granitoids.			All acepted sites were averaged into one single direction.
	Acatita Valley	2 Delicias	Norian	26.54	-103.03	590°	4	5			326.7	8.9	22.7	17.3	218 Ma				
	Acatita Valley	3 Delicias	Norian	26.54	-103.03	590°	4	5			339.7	1.2	24.8	14.7	218 Ma				
	Acatita Valley	4 Delicias	Norian	26.54	-103.03	590°	4	6			355.0	15.1	11.7	63.1	218 Ma				
	Acatita Valley	5 Delicias	Norian	26.54	-103.03	590°	3	6			328	12.5	66.9	4.5	218 Ma				
	Acatita Valley	11 Delicias	Norian	26.47	-103.01	590°	5	8			142.8	-12.3	19.3	16.7	218 Ma				
	Acatita Valley	12 Delicias	Norian	26.47	-103.01	590°	4	5			348.3	10.0	25.3	14.1	218 Ma				
	Acatita Valley	14 Delicias	Norian	26.264	102.82	590°	5	8			345.2	5.1	12.5	38.4	218 Ma				
	Acatita Valley	15 Delicias	Norian	26.264	102.82	590°	4	8			339.5	-16.7	9.7	89.8	218 Ma				
Nowicki, 1993	Cupido	1 Graceros	Aptian	25.26	-103.8	500-550°	18	30			350	44.3	3.4°	104.7	52.5 Ma	Fold Test Fold axis plunges < 13° on all folds	synfolding		k value is not betwen 10 and 85
	Cupido	2 Mulato	Aptian	25.26	-103.76	550-600°	27	32			338	41.1	5.2°	29.8	52.5 Ma		ate synfolding	30%	
	Aurora	3 España	Aptian	25.3	-103.5	500-600°	20	25			306	56	11.3°	9.3	52.5 Ma		synfolding		k value is not betwen 10 and 85
	Cuesta del Cura	4 Piedra Blanca	Cenoman	24.98	-103.25	650-660°	10	30			328.0	37.8	7.1°	47.5	52.5 Ma		Post-folding	10%	
	Cuesta del Cura	4 Piedra Blanca	Cenoman	24.98	-103.25	650-660°	10	30			328.0	38.6	6.8°	51.6	52.5 Ma		synfolding		
Clement et al., 2000		Cienega del Toro	Aptian	25.29	-100.29	580-640°		47	346	39.7	318.7	42.2	3.2	44.5	120 Ma		Positive		high temperature component shows a positive fold test.
		Santa Rosa Canyc	Aptian	24.74	-99.82	580-641°		91	54.3	-29	53.9	39.2	4.5	11.8	121 Ma	Fold Test			
Warrior, 2008	Zuloaga	Grutas Garcia 1	Oxfordian	25.871	-100.54		4	6	188.3	0	162.2	73.1	24	3		280°/75°	single site		In addition to the values that does not pass our quality filters, Warrior reports negative k values, double figures in some table's cells, colons instead of dots, and values that are not listed within the text. We reproduce Warrior's reported results in this table. We tried to contact the author and got no answer. We feel the results are not
	Zuloaga	Santa Catarina 2	Oxfordian	25.629	-100.45	4 mT	3	9	257.9	53.6	237.5	13.8	5.6	316.59		315°/52°			
	Zuloaga	Santa Catarina 2	Oxfordian	25.629	-100.45	2-14mT	7	9	113.8	86.9	206.9	42.3	11.8	22.9		315°/52°	single site		
	Zuloaga	Santa Catarina 2	Oxfordian	25.629	-100.45	ChRM	6	9	354.3	-14.1	350.1	26	1.5,23	-15.4-2.61		315°/52°			
	Zuloaga	Santa Catarina 2	Oxfordian	25.629	-100.45	ChRM	5	9	174.4	12.3	170.5	-26.2	8.6	64.3		315°/52°			
	Zuloaga	Arteaga 3.1	Oxfordian	25.479	-100.62	30-65mT	10	16	186.4	-33.3	185.2	26.5	10.6	19.63		~ 270°/60°			
	Zuloaga	Arteaga 3.1	Oxfordian	25.479	-100.62	30-65mT	5	16	158.4	-11	152.9	49.7	9.27	55.27		~ 270°/60°			
	Zuloaga	Arteaga 3.1	Oxfordian	25.479	-100.62	ChRM	7	16	176.9	-36	176.1	25.5	6.44	76.04		~ 270°/60°	locality composed of 3 sites		
	Zuloaga	Arteaga 3.2	Oxfordian	25.479	-100.62	ChRM	6	6	235	-70.2	188.1	-18.7	12.9	23.22		~ 270°/60°			
	Zuloaga	Arteaga 3.3	Oxfordian	25.479	-100.62	10-45mT	6	5	178	1.8	188.9	62.4	7.72	63.55		~ 270°/60°			
	Zuloaga	Arteaga 3.3	Oxfordian	25.479	-100.62	ChRM	3	6	189.2	-34.7	187.1	24.5	9.46	113.97		~ 270°/60°			
	Zuloaga	Gomez Farias 4	Oxfordian	25.047	-101.7	10-40 mT	13	16	345.6	62.8	201.1	55.6	6.67	37		262°/62°			
	Zuloaga	Gomez Farias 4	Oxfordian	25.047	-101.7	ChRM	8	16	317	55.3	224	47.8	9.38	31.32		262°/62°			
	Zuloaga	Sombreretillo 6.1	Oxfordian	24.848	-101.58	ChRM L1	5	10	352.7	21.5	353.5	2.9	20.2	12.19		274°/19°	negative fold test, 6.2 is overturned		
	Zuloaga	Sombreretillo 6.2	Oxfordian	24.848	-101.58	ChRM L2	10	17	357.4	12.6	29.1	-12.8	10.2	26.81		291°/26°*			
	Zuloaga	Charcas	Oxfordian	23.13	-101.2	NOT REPORTED,													

	Zuloaga	Real de Catorce	Oxfordian	23.689	-100.88	Low NRM											trustworthy as they are presented and we decided to discard all of them.
	La Joya	Real de Catorce 7	Jurassic	23.689	-100.88	ChRM	10	14	302	37.5	298	18	9	28.1	n/a		
	La Joya	Real de Catorce 7	Jurassic	23.689	-100.88	ChRM	5	5	276	-36.7	278	-16.7	10.5	29.06	n/a		
	La Boca	La Perra 5.2	Jurassic	24.552	-99.89	ChRM	12	15	131	5.8	131	5.8	1.1, 16	-10.46	horizontal	Structure asociated to primary aluvial fan no strctural correction done.	
	La Boca	La Perra 5.3	Jurassic	24.552	-99.89	300°-550°C	15	20	123	-24	123	-24	15,21	4.35, -0.76	horizontal		
	La Boca	La Perra 5.3	Jurassic	24.552	-99.89	300°-550°C	3	20	258	8.1	258	8.1	5.05	111.54	horizontal		
	La Boca	La Perra 5.3	Jurassic	24.552	-99.89	ChRM	7	20	269.2	-8.1	269.2	-8.1	14.9	14.89	horizontal		
	La Boca	La Perra 5.4	Jurassic	24.552	-99.89	ChRM	9	10	86.4	12.9	86.4	12.9	9	25.11	horizontal		
	Zacatecas	San Rafael (CHA)	Triassic	23.076	-101.2	ChRM	13	18	150.1	-35	116	0.9	11.5	12.8	180°/90		
	Zacatecas	San Rafael (CHA)	Triassic	23.076	-101.2	< 6 mT	13	18	147.4	-22.1	128.5	2.9	10.5	15.33	180°/90	vertical bedding	
	Zacatecas	San Rafael (CHA)	Triassic	23.076	-101.2	< 45 mT	15	18	325.9	21.5	130.6	5.3	6, 17	7.59, -0.66	180°/90		
	Red Beds	La Boca Canyon	Jurassic	23.8	-99.2		4		270	-6.1			18.4	26.00			
	Red Beds	La Boca Canyon 2	Jurassic	23.8	-99.2		25		291	-6.3			7.6	15.30			
	Red Beds	La Boca Canyon 3	Jurassic	23.8	-99.2		21		276	-17			5	41.60			
	Red Beds	La Boca Canyon 4	Jurassic	23.8	-99.2		11		93.2	2.4			7.6	36.70			
Belcher, 1979	Red Beds	La Boca Canyon 5	Jurassic	23.8	-99.2		10		271	-18			8.5	32.90			This work does not show stepwise demagnetization.
	Red Beds	La Boca Canyon 7	Jurassic	23.8	-99.2		24		106	1.8			9.9	9.90			
	Red Beds	Caballeros Canyon	Jurassic	23.83	-99.27		20		33	-1.8			10.7	10.40			
	Red Beds	Caballeros Canyon	Jurassic	23.83	-99.27		20		39.9	5.4			5.4	37.80			
	Red Beds	Caballeros Canyon	Jurassic	23.83	-99.27		28		41.3	26			7.4	14.50			
	Red Beds	Caballeros Canyon	Jurassic	23.83	-99.27		4		329	37.3			37.2	7.10			
	Red Beds	Miquihuana	Jurassic	23.7	-99.8		41		30.7	17.7			5.5	17.70			
	La Boca	1 Miquihuana	Jurassic	23.7	-99.8	650°	28	33			30	17.3	6.5	18.4	069°/35°		
	La Boca	Cañon Caballero	Jurassic	23.83	-99.27	650°	14	20			40.8	3.1	13.1	10.2	323°/80°		
	La Boca	Cañon Caballero	Jurassic	23.83	-99.27	650°	15	17			40	3.2	7.5	26.6	323°/80°		
	La Boca	Cañon Caballero	Jurassic	23.83	-99.27	650°	20	24			44.7	27.7	10.1	11.4	323°/80°		
	La Boca	5 Cañon Peregrin	Jurassic	23.77	-99.24	Vector	12	12			229	-25.1	13.9	10.7	323°/80°		
	La Boca	6 Cañon La Boca	Jurassic	23.8	-99.2	650°	18	23			284	-6.4	6	34.4	323°/80°		
	La Boca	7 Cañon La Boca	Jurassic	23.8	-99.2	650°	17	20			276	-18	5.6	41.5	323°/80°		
	La Boca	8 Cañon La Boca	Jurassic	23.8	-99.2	650°	14	15			264	-18.2	8	25.6	323°/80°		
Gose, 1982	La Boca	9 Cañon La Boca	Jurassic	23.8	-99.2	650°	19	25			111	-1.2	9.2	14.2	323°/80°	Fold Test Positive	Stepwise demagnetization provides only 6 steps from NRM to 650° C. This study does not provide vector endpoint diagrams (e.g. Zijderveld plots) and therefore the linearity of the scarce demagnetization steps can't be tested. The paper does not provide PCA or other valid statistical analyses for the demagnetization and linearity. No foldtest is provided, although the paper mentions it is positive. We could not assess the reliability and trustworthiness of the datasets.
	La Boca	0 Cañon Huizach	Jurassic	23.6	-99.2	625°	49	51			141	-4.6	3.5	35.5	314°/79°		
	La Boca	1 Cañon Huizach	Jurassic	23.6	-99.2	625°	39	39			156	-13.3	6.5	13.5	314°/79°		
	La Boca	12 Galeana	Jurassic	24.69	-100.09	625°	17	17			137	-47.9	6	36.1			
	La Joya	3 Cañon Peregrin	Jurassic	23.77	-99.24	Vector		14			124	-34	12.6	10.9	323°/80°		
	La Joya	4 Cañon Huizach	Jurassic	23.6	-99.2	Vector		13			142	-23.3	9.7	19.1	314°/79°		
	Zuloaga	5 Cañon Peregrin	Oxfordian	23.77	-99.24	300°	16	21			181	-37.5	2.3	263.5	323°/80°		
	Zuloaga	6 Cañon Huizach	Oxfordian	23.6	-99.2	400°	10	13			350	44.4	7.5	42.8	314°/79°		
	Cuesta del Cura	5 Cañon Peregrin	Cenoman	23.77	-99.24	400°	19	25			345	43.5	2.8	144.2	323°/80°		
Kleist, 1984	Cupido	Los Chorros	Aptian-Albian	25.39	-100.79	400°	401		294	52.3			7.20	5.2		Fold Test Positive	Stepwise demagnetization provides only 6 steps from NRM to 700° C. The linearity of the scarce demagnetization steps can't be tested. The paper does not provide PCA or other valid statistical analyses for the demagnetization and linearity. The provided fisher statistics show k value is not betwen 10 and 85. There is no cuantitative fold test and, although the paper mentions it is positive, We could not assess the reliability and trustworthiness of the datasets.

N number of demagnetized Specimens, Ns number of specimens that passed the Cutoff, mDec mean declination, mInc mean inclinationg, k recision parameter, a95 radius of the 95% confidence cone about site-mean direction,K precision paramenter of the poles, A95 radius of 95% confidence circle around paleomagnetic pole, A95min and A95max describe the minimum and maximun values of A95 allowed to consider the average representative. ΔDx, uncertainty in declination; ΔIx, uncertainty in inclination. Green/Red shaded fields were accepted/rejected on basis of reliability criteria (section 2.4).

The Majority of the sites studied by Molina-Garza (2004) passed the criteria. They were averaged out as a single locality. A baked contact test supports these directions and they show very similar directions with Paleozoic overlying strata. González-Naranjo et al. (2012) reported sampling 368 oriented cores across 50 sites of an Oligocene ignimbrite (Panalillo Ignimbrite). Only 20 of the 50 sites passed the quality criteria and they were averaged out as a single mean direction.

Nova-Rodríguez (2016) reported sampling from three localities, Real de Catorce (20 sites; Figure 2.1 B), Charcas (10 sites; Figure 2.1 C), and Huizachal Valley (16 sites; Figure 2.1 D). This author provided the sample data at the specimen level, enabling a precise reinterpretation of the data. Here under is a brief description of the sampled localities and the methodologies as described by this author.

3.6.1 Real de Catorce (23.621°N, -100.855° E)

The Real de Catorce locality is described as an antiformal stack that developed between 91-53 Ma (Fitz-Díaz et al., 2018; Gutiérrez-Navarro et al., 2021). In this area the Nazas Fm. unconformably overlies the Triassic Potosí fan (Centeno-García et al., 2005; Silva-Romo et al., 2000). Here the Nazas Fm. yielded a U-Pb zircon age of 174.7 ± 1.3 Ma (Barboza-Gudiño et al., 2012). The La Joya Fm. unconformably overlies the Nazas Fm., and shows evidence that suggests that it acted as a decollement, which was developed in the Late Cretaceous during the thin-skinned deformation event (Gutiérrez-Navarro et al., 2021). In this locality, the author extracted 103 cores, each site in a single fine-grained bed from a 60 m thick succession of sandstones. The sample sites were labeled RC11 - RC26. (Figure 3.5 A).

3.6.2 Charcas, San Luis Potosí (23.131°N, -101.188° E)

In this locality the Nazas Fm. was dated (U-Pb in zircon) 179 ± 1 Ma (Zavala-Monsiváis et al., 2012). This locality has been described as an anticlinorium and it is located in the same crustal block in the vicinity of the Real de Catorce locality. Nova (2016) collected samples along the San Antonio River in an exposed stratigraphic succession of the Nazas Fm. (Figure 3.5 B) approximately 80 m., 60 cores from 10 sites of the Nazas Fm. in four andesitic flows, interbedded tuff, and epiclastic deposits. Each sampled site (CHA-1 to CHA-10) corresponds to separate lava flows no thicker than 2 m, with the exception of sites CHA-1 and 2 which were collected from a single epiclastic deposit.

3.6.3 Huizachal Valley (23.588°N-99.222° E)

In this locality the Nazas Fm. outcrops in the core of a structural dome, the Huizachal-Peregrina anticlinorium, here it's overlain by the Jurassic red beds of the La Boca and La Joya Formations (Figure 3.5 C; Rubio-Cisneros & Lawton, 2011). The La Boca Formation here has a maximum depositional age of ~190 Ma (Detrital zircon; Rubio-Cisneros & Lawton, 2011). 105 samples from La Joya and La Boca Formations were drilled in this locality. Seven sites, (45 samples) labeled HUI42 – HUI48 correspond to La Boca Formation, which locally consists of fine to coarse red sandstones. Samples were collected in the upper member. In the northwestern limb of the anticline, 62 cores distributed in nine sites (HUI28 – HUI40) were collected from the La Joya Formation, in an outcrop that lies approximately 1 km SW from the previously sampled sites. Each site sampled comprises a single bed of about two meters thick.

Rodríguez-Parra (2020) sampled 12 sites in the Villa Juárez locality and several more in Charcas from the Nazas Formation. However, only the sample data from Villa Juárez was obtained.

3.6.4 Villa Juárez, Durango (25.501°N, -103.621° E)

The age of the volcanic rocks of the Nazas Fm. in this locality is 182.9 +- 2.5 Ma (Barboza-Gudiño et al., 2021). 2 - 3 oriented blocks were collected in 17 sites (NA01 - 17) from 4 andesitic lava flows in the limbs of the Villa Juárez anticline (axis' plunge/trend = 18°/315°). The sampled blocks yielded 85 cores. Lava flows are interbedded with volcano-sedimentary rocks, and do not show evidence of penetrative deformation (Figure 3.5 D & E). Although the precise age of the folding is unknown, the structure is attributed to thin-skinned deformation coupled with the buttressing effect of the Coahuila block, an adjacent basement high. Sediments accumulated in this part of the basin were thrust over the southern margin of the continental block during the Late Cretaceous regional shortening (Lawton & Molina Garza, 2014).

All localities that passed the criteria were processed and are listed in Table 3.1 and are shown in Figure 2.1. Any sites that did not pass the reliability criteria were excluded from any further analyses (See Table 3.1 for details).

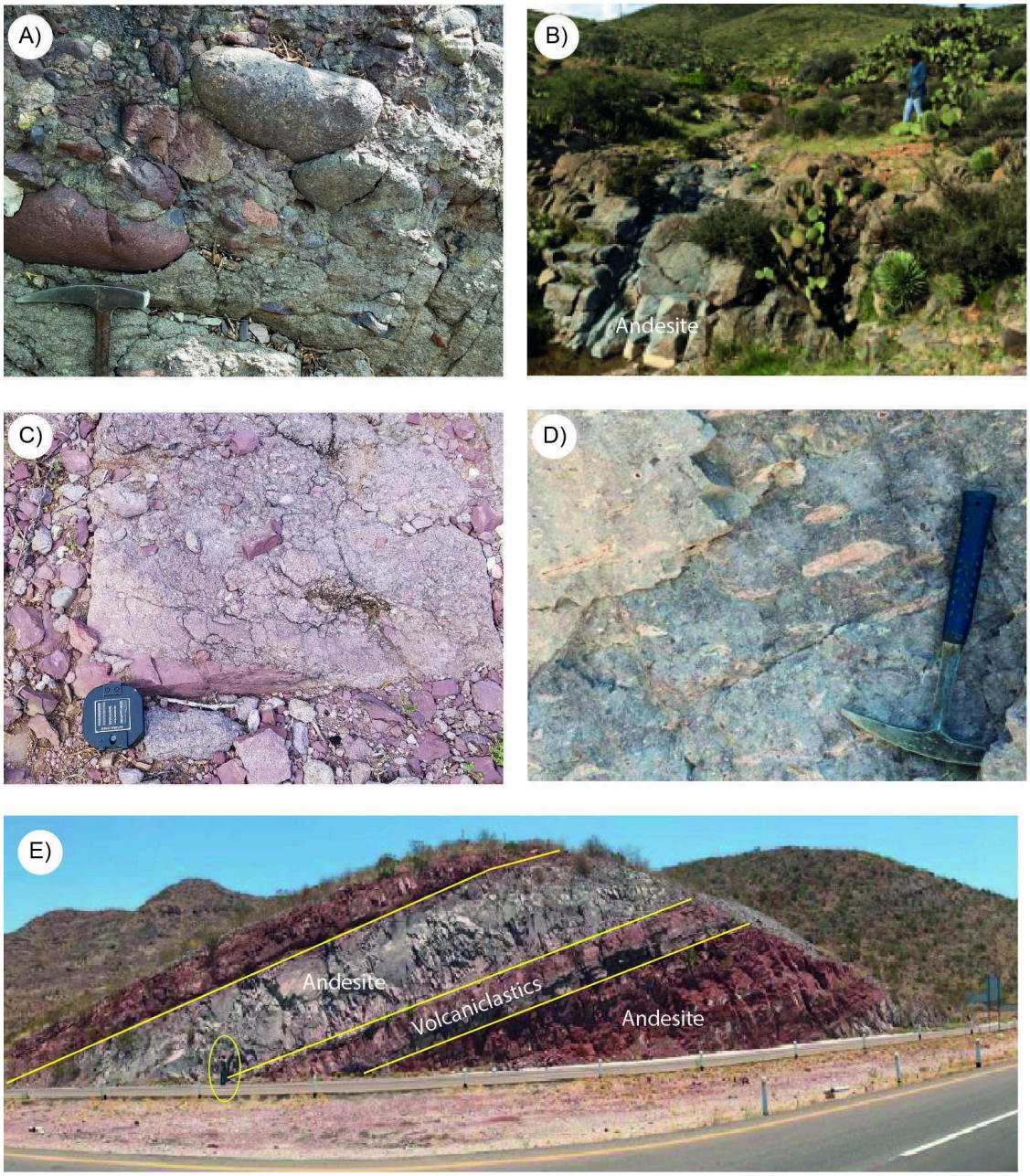

Figure 3.5 Photographs of representative Red Beds and Nazas formation sampling sites from Nova-Rodríguez, (2016) and Rodríguez-Parra (2020). A) La Joya Fm. in Real de 14 locality shows a conglomerate with a fine matrix all clasts are igneous in origin. B) Andesite from the Nazas formation in the Charcas locality (Nova-Rodríguez, 2016), C) Sandstone-Siltstone from La Joya Fm. at the Huizachal Valley, D) Andesite from Villa Juárez Locality, and E) Road cut outcrop at the Villa Juárez locality yellow circle denotes person for scale (Nova-Rodríguez, 2016; Rodríguez-Parra, 2020).

Chapter 4

Results and Interpretations

"Whether you think you can or think you can't – you're right."

– Henry Ford

Part of the results of this chapter have been published in the Journal of Geophysical Research: Solid Earth under the title: "**The Sierra Madre Oriental Orocline: Paleomagnetism of the Nazas Province in NE Mexico**." 129, https://doi.org/10.1029/2024JB029239

The following chapter contains a narrative of the process of obtaining the results of the previous chapter as well as a first-order interpretation of such results. The results are organized in a conventional paleomagnetic hierarchy (Area, site, and specimen) and technique. The complete interpretations of the Tectonic and Geodynamic implications will be contained in the next chapter.

4.1 The San Julian Uplift

4.1.1 IRM and Hysteresis

In the majority of the samples, IRM results show noisy curves. The 26 representative volcanic samples reached saturation below 400 mT suggesting that their remanence is primarily ferrimagnetic phases (probably Ti-magnetite; Gubbins & Herrero-Bervera, 2007). The Caopas laccolith's coarse texture and the scarcity of magnetic minerals resulted in noisy curves (dia-/para magnetic; Figure 4.1). The hysteresis runs did not reach saturation at 1 T, but, interpretable results show loops similar to superparamagnetic magnetite (grain size <10 nm; (Dunlop & Özdemir, 1997) with a possible minor content of a hard phase of hematite (Figure 4.2 A). The NRN sites of the andesites from the Nazas North area show a hysteresis loop with a high coercivity phase that does not saturate at 1 T (Figure 4.2 B), This phase is interpreted as hematite (Gubbins & Herrero-Bervera, 2007).

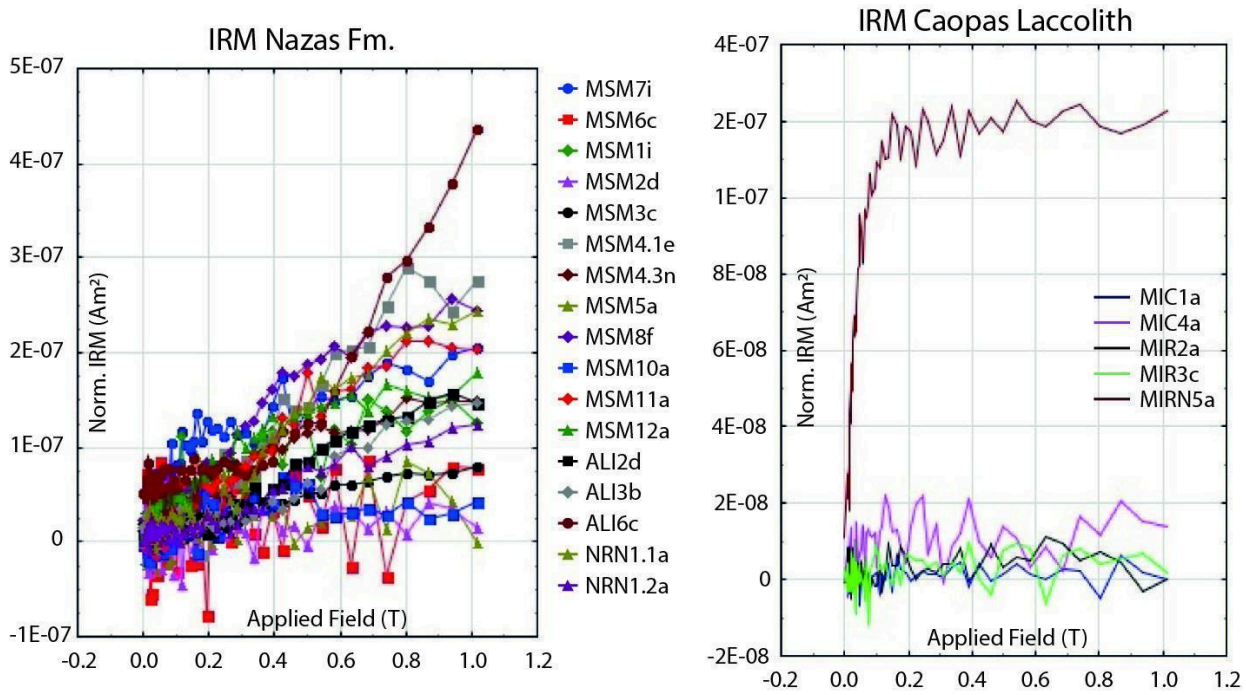

Figure 4.1 IRM results for the Nazas Fm., and the Caopas laccolith in the San Julián area.

4.1.2 Thermomagnetic Curves

The volcanic samples show curves that progressively demagnetize, some samples presented sharp drops in magnetization between 600° and 700° C indicative of hematite (O'Reilly, 1984). Other samples (e.g., MSM3), show a decrease in magnetization around 500 °C (Annex 4.2), which may indicate the coexistence of magnetite and hematite (Dunlop & Özdemir, 1997). Some curves showed a subtle presence of sulfides suggested by a small magnetization increase between 400 and 500 °C (e.g., De Boer & Dekkers, 1998). On all the volcanic samples a major phase with mineralogical alteration during heating was evident, commonly hematite to maghemite due to heating (Dunlop & Özdemir, 1997), and in some cases paramagnetic curves (Gubbins & Herrero-Bervera, 2007). Similar behavior was also observed in the samples from the Caopas intrusive (Figure 4.2 C and Annex 4.3).

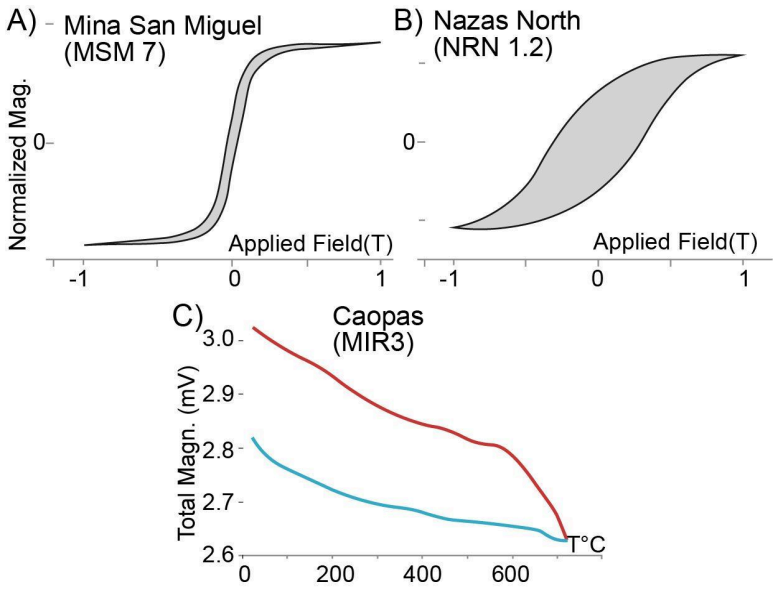

Figure 4.2 Magnetic properties results of representative samples. Hysteresis loops were executed in increments of 20 mT on a time of 600 ms on average and corrected for paramagnetic-diamagnetic phases. The Mina San Miguel samples show a thin waist loop that is interpreted as magnetite (A). The Nazas North loop displays a high coercivity shape, likely the presence of hematite (B). Total magnetization - temperature (°C) graph for the Caopas laccolith, unblocking temperatures are representative of hematite and magnetite (C).

4.1.3 Anisotropy of Magnetic Susceptibility

The AMS results portray uniform anisotropies near the mean (Km ≈ 592.7 x 10^{-9}) in both the Caopas and MSM samples. The MSM shows a low (P) anisotropy value (< 1.02). But in contrast, the Caopas laccolith shows higher and relatively variable values (1.032 - 1.343; Figure 4.3). Both areas show pen-isotropic ellipsoids and no apparent penetrative deformation. The K_{min} axes from the MSM locality show parallelism to the poles of the lava-flow bedding seen on structural data (Figure 4.3 MSM GEO) resembling an antiformal structure. After unfolding, the K_{min} axes follow similar behavior as the bedding poles (grouping on the vertical), suggesting a pre-folding horizontal fabric (Figure 4.3 MSM TEC). In the Caopas laccolith and MSM areas have low anisotropy values and isotropic ellipsoids coherent with undeformed

or weakly deformed medium. The Caopas laccolith K_{min} axes group on the vertical which is representative of an internally undeformed intrusive body that responded to the effects of magmatic flow and gravity (Figure 4.3 Caopas). The general direction of the mineral lineation (NE-SW) observed on the field (Guerra Roel, 2019) coincides with the magnetic lineation obtained in this study (K_{max}).

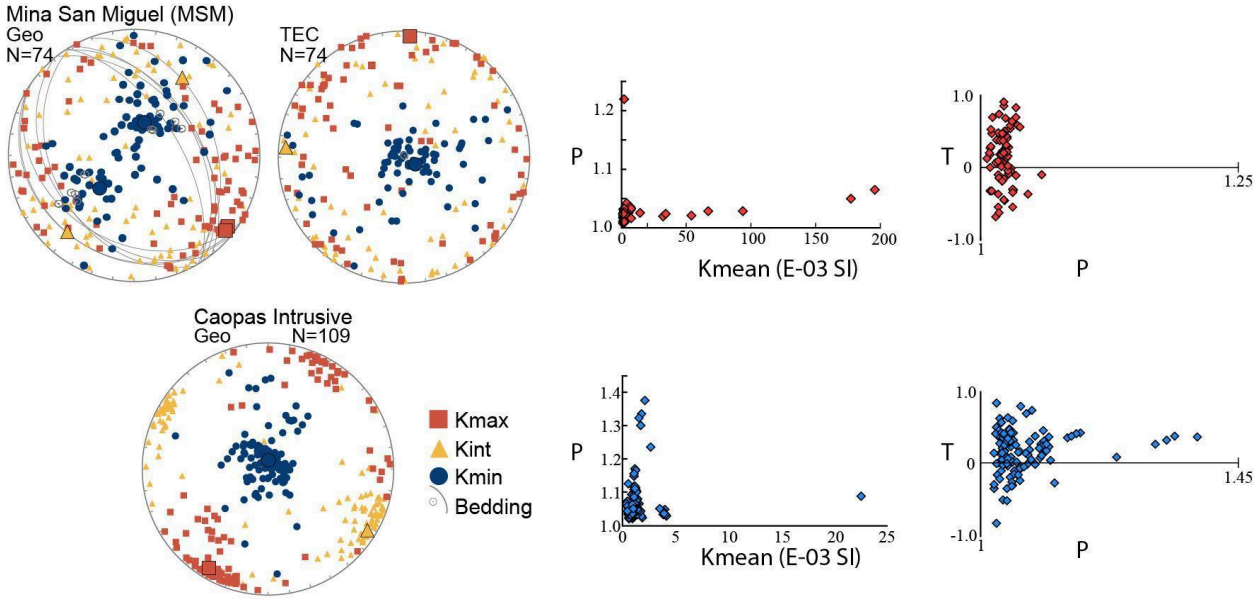

Figure 4.3 Anisotropy of Magnetic Susceptibility of the San Julián Uplift localities (MSM, Caopas). Results are represented in equal area projections for the analyzed sites. Larger symbols represent site mean. Grey lines represent structural data. Graphs are shape parameter (P) vs. Mean magnetic susceptibility and Shape parameter T vs. Anisotropy parameter P show degree of anisotropy.

4.1.4 Scanning Electron Microscopy

The photomicrographs from the MSM locality show anhedral magnetite crystals surrounded by hematite weathering rims (Figure 4.4 A) and present as a secondary mineral that fills fractures. Also, in less proportion, along the crystal cleavages of amphibole phenocrysts (Figure 4.4 B).

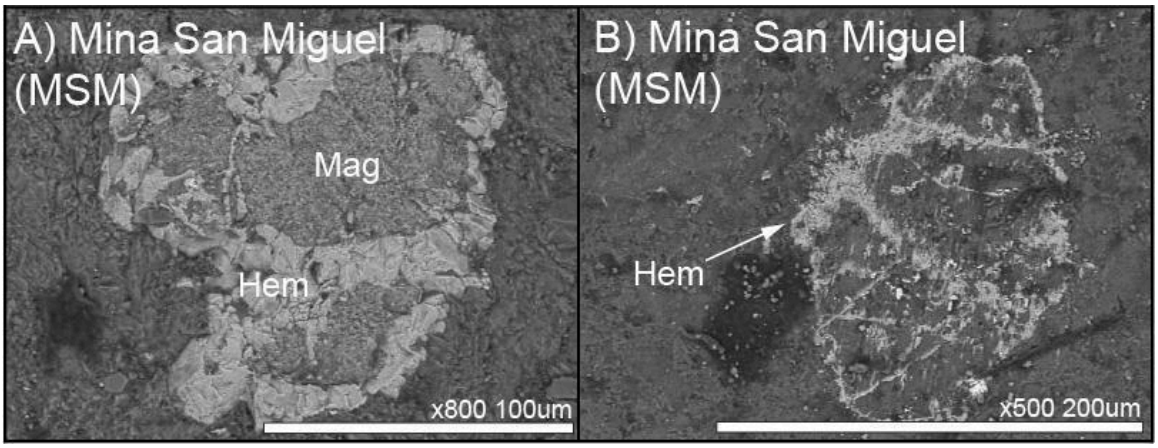

Figure 4.4 Scanning Electron photomicrographs of representative samples of the Nazas Fm. in the Mina San Miguel locality in the San Julián area. Photomicrographs show primary magnetite with alteration rims of hematite and hematite that grew in the fractures of an amphibole crystal.

4.1.5 Paleomagnetism

The samples from this locality did not demagnetize with alternating fields demagnetization due to the presence of hematite, which requires fields higher than the typical of the commercial degaussers. With thermal demagnetization a Characteristic Remanent Magnetization (ChRM) was isolated with a downwards inclination and a west declination, between 500-580 °C and 40-60 mT (Figure 4.5). This component was labeled W (for west). The W component was isolated in 12 sites of the Mina San Miguel (MSM) locality (Figure 4.6 A), 15 sites of the Caopas laccolith (Figure 4.6 B), and 7 sites of the Nazas North (Figure 4.6 C) 129 samples in total (See Table 4.1 for site level data). The MSM area shows a mean downward dec/inc of 285°/21° (geographic coordinates) and single polarity with a concentration parameter k of 10; K = 17.4 and A95 = 3.6 (See Table 4.6 for locality mean parameters). The VGP projection shows a rounded shape and the A95 is within the Deenen

(2011) envelope, suggesting that the distribution scatter present can be explained as a function of the PSV and not from another source of error. At the site level the dispersion (k) ranges between 20-50 with MSM5 and MSM3 over 200 and MSM10 with the lowest (13) (Table 4.1).

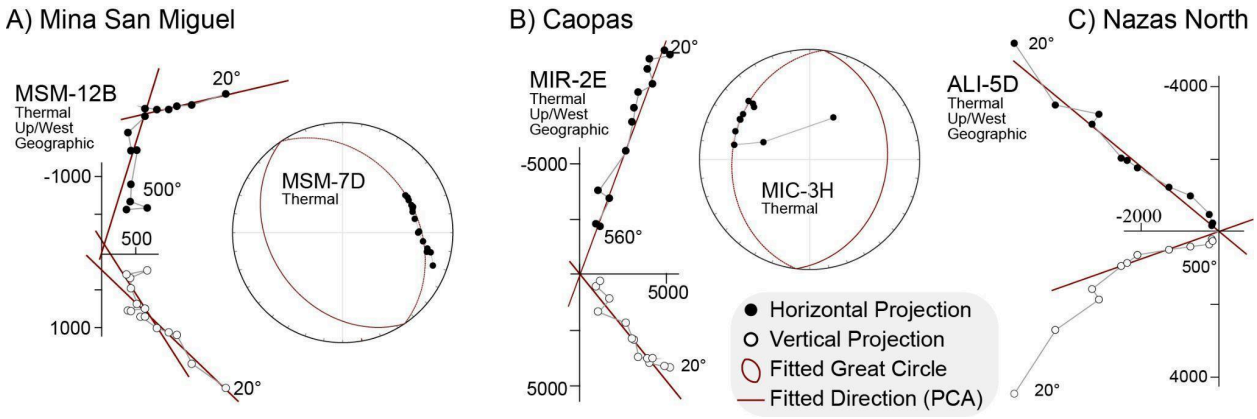

Figure 4.5 Directions obtained from the samples collected are expressed in Zijderveld's (1967) diagrams and fitted great circles. (A) Mina de San Miguel "MSM" locality, (B) Caopas Laccolith "MIR, MIC", (C) Nazas North "ALI" are representative samples from the Nazas Fm. sampled in Geographic Coordinate system. Thermal = Thermal Demagnetization. PC = Principal Component.

The results from the Caopas laccolith show progressive demagnetization and unblocking temperatures between 400° and 560 °C (Figure 4.5 B), with an mean direction of 271°/18° in geographic coordinates (Figure 4.6 B) and a precision parameter of k = 10. The VGPs for this area have a K of 13.40 and an A95 of 5.66 in between the Deenen (2011) envelope (Table 4.6 B). The VGP plot reveals an elongated W-E shape (Figure 4.6 B). Although this result shows to be within Deenen's limits, it's suspected that the elliptical shape indicates another cause of additional scatter separate from PSV. Perhaps an unaccounted structural or magnetic acquisition problem; this result was considered with caution.

The last sampled locality in the San Julián Uplift area is the “Nazas North” (Figure 4.5 C & Figure 4.6 C). This locality has similar results in direction, however, this locality shows a larger dispersion for the W component. It is located in the northern part of the San Julián Uplift and due to poor exposure in the area it lacks reliable structural data for correction. The mean dec/inc of the W component in this locality is 262°/27° and has a dispersion k of 8.3 and an A95 of 11°. The Nazas North directions isolated from the samples of this area show large dispersion in declinations, which becomes especially notorious in the VGP projections. The plots show elongation in the E-W coordinate (Figure 4.6 C). The A95 of 11.21 is larger than Deenen’s $A95_{max}$, which indicates additional sources of scatter. The source of scatter for this locality is unknown, however, it is reasonable to think that is the result of unidentified structural problems or magnetic acquisition. The results of this locality are not of sufficient quality to represent a reliable dataset to quantify vertical axis rotations or latitudinal motion. However, its average direction (dec/inc) is analogous to the results obtained in the MSM and Caopas laccolith areas, which supports the data obtained in such places. The raw and interpreted data at the specimen level can be accessed in this thesis’s digital annex 2 and in the open acces data repository (Guerra Roel, 2023).

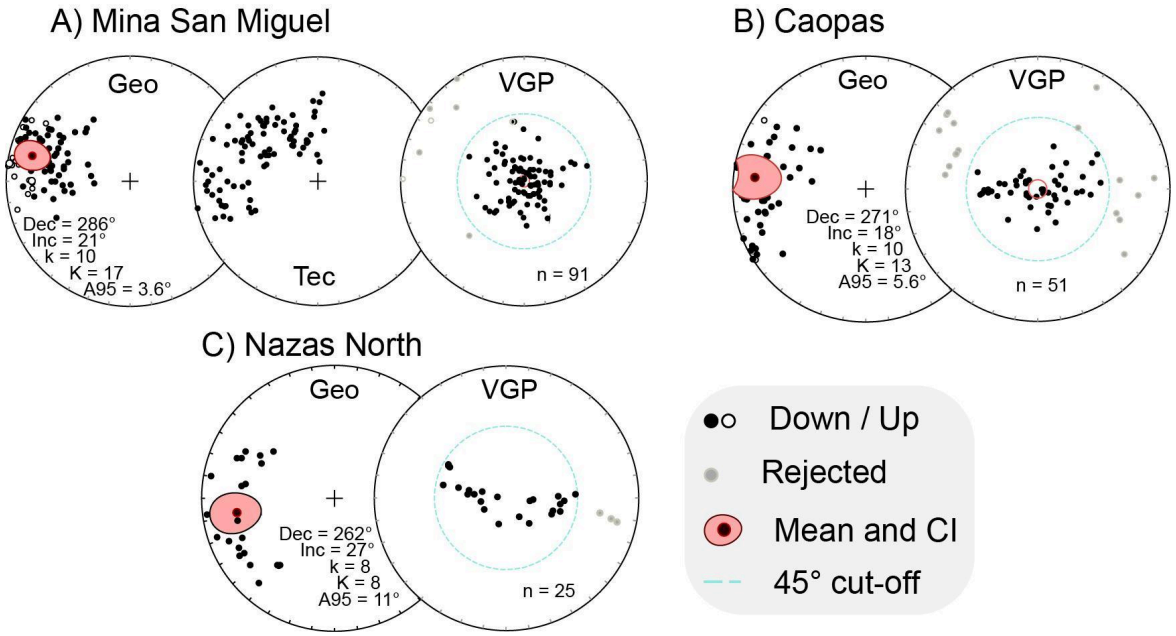

Figure 4.6 Equal area projections of the direction vectors of all the localities sampled in the San Julián area. A) Mina San Miguel, B) Caopas laccolith, and C) Nazas North. All directions are shown as normal polarity. Geo = geographic; VGP = Virtual Geomagnetic Poles (for site level parameters see Table 4.1, for locality mean parameters please see Table 4.6).

Table 4.1 San Julián Uplift site mean directions in geographic coordinate system.

	N	Ns	mDec	mInc	k	a95	K	A95	A95		ΔDx	ΔIx	Pole Lng	Pole Lat	Coordinates	
Geographic									Min	Max					Lat.	Long.
MSM1	9	13	296.2	15.53	26.28	10.23	47.57	7.54	4.98	20.54	7.61	14.27	170.14	9.3	24.906	-102.2
MSM2	7	7	278.4	-2.02	55.17	8.2	166.7	4.69	5.51	24.07	4.69	9.37	163.44	7.19	24.901	-102.2
MSM3	5	5	291.2	8.53	453.9	3.6	591.5	3.15	6.3	29.75	3.16	6.19	162.69	21.02	24.895	-102.1
MSM4-1	5	5	270.1	-21.83	124.3	6.89	122.6	6.94	6.3	29.75	7.08	12.44	157.48	-4.63	24.895	-102.1
MSM4-2	5	5	274	47.56	95.3	7.88	63.78	9.65	6.3	29.75	11.02	11.42	193.1	14.79	24.895	-102.1
MSM4-3	14	14	289.6	35.35	26.35	7.89	22.99	8.47	4.18	15.55	8.99	12.69	178.83	25.76	24.895	-102.1
MSM5	6	6	287.8	18.63	204.1	4.7	263.7	4.13	5.86	26.52	4.19	7.63	169.3	20.15	24.892	-102.1
MSM6	6	6	294.3	12.59	46.92	9.88	94.96	6.91	5.86	26.52	6.95	13.33	163.42	24.78	24.892	-102.1
MSM7	6	6	286.1	-17.23	20.09	15.32	23.89	13.99	5.86	26.52	14.16	26.14	152.63	10.68	24.892	-102.1
MSM8	4	6	190.9	52.36	28.04	17.66	23.64	19.3	6.89	34.24	23.19	20.44	250.51	-20.24	24.888	-102.2
MSM9	6	6	274.6	35.75	18.5	15.99	23.07	14.25	5.86	26.52	15.16	21.2	185.84	12.7	24.888	-102.2
MSM10	4	4	276	49.39	13.97	25.48	10.43	29.87	6.89	34.24	35.21	33.92	195.35	17.21	24.887	-102.2
MSM11	6	6	285.9	34.43	44.59	10.14	42.91	10.34	5.86	26.52	10.94	15.73	179.51	22.04	24.885	-102.2
MSM12	6	6	287.2	37.04	24.39	13.84	20.81	15.03	5.86	26.52	16.09	21.88	180.86	24.21	24.884	-102.1
NRN1-2	4	4	102.1	-5.07	916.2	3.04	2254	1.94	6.89	34.24	1.94	3.85	344.98	-12.07	24.873	-102.2
NRN1-1	3	3	237.6	20.87	239.4	7.99	221.9	8.29	7.73	41.04	8.45	15.01	193.04	-23.48	24.873	-102.2
ALI6	3	3	247.3	23.37	70.48	14.8	75.22	14.32	7.73	41.04	14.65	25.25	188.98	-14.52	24.949	-102.2
ALI5	4	4	249	18.35	12.33	27.26	12.68	26.84	6.89	34.24	27.24	49.69	185.6	-14.07	24.954	-102.2
ALI4-2	3	3	332.9	20.46	100.8	12.34	125.7	11.04	7.73	41.04	11.23	20.06	143.57	60.48	24.953	-102.3
ALI4-1	4	4	273.6	11.61	21.8	20.13	48.59	13.31	6.89	34.24	13.39	25.82	171.81	6.03	24.953	-102.3
ALI3	4	4	217	34.82	336.2	5.02	257	5.74	6.89	34.24	6.08	8.68	215.08	-33.07	24.956	-102.3
ALI1	7	7	297.6	31.76	86.3	6.53	141.9	5.08	5.51	24.07	5.32	8.06	173.44	31.95	24.948	-102.3
MIC1	4	4	245.7	8.57	48.54	13.32	106.6	8.94	6.89	34.24	8.96	17.58	182.65	-19.81	24.818	-102.2
MIC2	8	8	284	26.56	16.84	13.9	21.77	12.14	5.22	22.12	12.52	20.64	176.09	18.72	24.816	-102.2
MIC3	8	8	280.9	8.65	6.89	22.74	8.64	19.98	5.22	22.12	20.04	39.28	167.33	12	24.815	-102.2
MIC4	7	7	266.5	15.8	42.23	9.4	86.07	6.54	5.51	24.07	6.61	12.36	176.74	0.24	24.813	-102.2
MIC6	4	4	213.4	29.03	127.8	8.16	361.8	4.84	6.89	34.24	5.02	7.97	215.47	-38.07	24.8	-102.2
MIC7	4	4	270	17.94	23.32	19.44	27.8	17.74	6.89	34.24	17.98	32.95	176.41	3.62	24.801	-102.2
MIR1	4	6	304.2	-8.69	4.22	50.95	6.46	39.19	6.89	34.24	39.33	77.05	164.17	7.64	24.856	-102.2
MIR2	2	4	281.5	21.37	72.88	29.69	70.67	30.16	9.09	52.99	30.79	54.31	209.43	44.63	24.847	-102.2
MIR3	6	6	294.5	25.32	4.38	36.2	6.69	27.96	5.86	26.52	28.8	48.25	173.38	28.37	24.843	-102.2
MIR4	4	4	193.2	47.84	181.7	6.83	194.8	6.6	6.89	34.24	7.54	7.76	243.76	-34.61	24.836	-102.2
MIR5	2	2	273.9	36.21	15.17	69.36	17.7	63.4	9.09	52.99	72.21	93.62	184.99	12.89	24.831	-102.2
MIRN3	2	2	272.4	24.98	17.04	64.82	22.76	55.03	9.09	52.99	57.29	95.35	179.28	7.22	24.875	-102.2
MIRN4	2	2	331.7	41.24	9.15	95.67	7.2	114.7	9.09	52.99	82.79	154.6	172.71	62.67	24.88	-102.2
MIRN5	4	4	240.5	4.39	477.3	4.21	836.7	3.18	6.89	34.24	3.18	6.33	183.3	-25.48	24.88	-102.2
MIRN7	4	4	300.1	19.92	5.42	43.56	7.73	35.35	6.89	34.24	36.01	64.54	166.27	32.82	24.884	-102.2

N number of demagnetized specimens, Ns number of specimens that passed the Cutoff, mDec mean declination, mInc mean inclinationg, k precision parameter, a95 radius of the 95% confidence cone about site-mean direction,K precision paramenter of the poles, A95 radius of 95% confidence circle around paleomagnetic pole, A95min and A95max describe the minimum and maximun values of A95 allowed to considered the average representative. ΔDx, uncertainty in declination; ΔIx, uncertainty in inclination

4.2 - Taraises Formation

4.2.1 Rock Magnetism

Five thermomagnetic runs were conducted to determine the optimal demagnetization procedures. A more extensive list of runs were scheduled, however, after repetitive results, the runs were canceled. Thermomagnetic curves revealed that samples contained small amounts of magnetite with a mostly paramagnetic behavior (Figure 4.7 A; Annex 4.4)

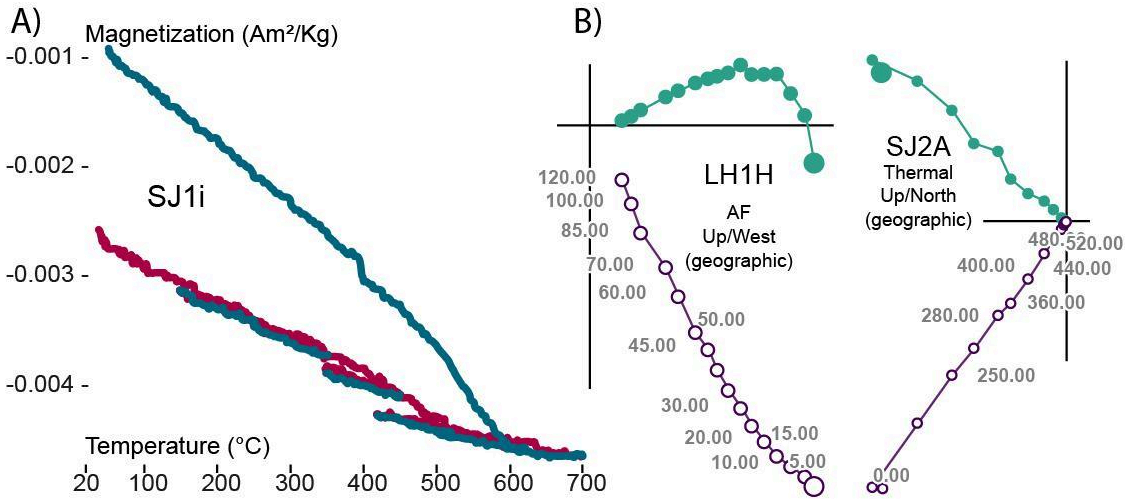

Figure 4.7 A) Magnetization vs. Temperature graph of the thermomagnetic runs. B) Zijderveld diagrams (Zijderveld, 1967) of two representative samples. The curie run (A) shows progressive demagnetization during heating indicating (ti)-magnetite as the main magnetic carrier evidenced by maximum unblocking temperatures of 480–520 °C and alternating magnetic fields of 60–90 mT. B) Example of two representative Zijderveld diagrams. Samples LH1H and SJ2A show a single component that demagnetizes to the origin (Thermal and AF) and the presence of a viscous component that was removed at low coercivities and temperatures <15 mT and <200 °C.

4.2.3 Anisotropy of Magnetic Susceptibility

All sites of the Taraises Fm. samples show low degrees of anisotropy (P < 1.05), and the AMS ellipsoids have poorly defined axes with large uncertainties,

indicating that the rocks did not possess a strong sedimentary fabric nor experienced significant internal deformation. AMS ellipsoids were represented in equal-area projections and shape parameter graphs in both Flinn (1962) and Jelinek (1981) (Annex 4.5).

4.2.4 Joint set Analysis

The spatial distribution of the systematic joint sets from the 23 anticlines (~40 readings per anticline) show no apparent slip indicators, suggesting they originated as Mode I (tensile) fractures that were not reactivated. Joint set orientations that represented less than 4% of the total measured population were not considered ~20 in most cases. Two main joint set families were identified: 1) Vertical and strike-perpendicular ('cross-fold') joint set, which is typical in fold-and-thrust belts (e.g., Hancock, 1985), 2) a strike-parallel set in 3 localities (Figure 4.8), which was insufficient for kinematic analyses (e.g., Engelder & Geiser, 1980). Due to their geometric characteristics (vertical and perpendicular to the fold axis), back-tilting the joint sets did not offer any pertinent information. The strike-perpendicular joint set draws a fan pattern perpendicular to the trend of the Sierra Madre Oriental Orocline in the Cretaceous basin (Figure 4.8 and 5.10).

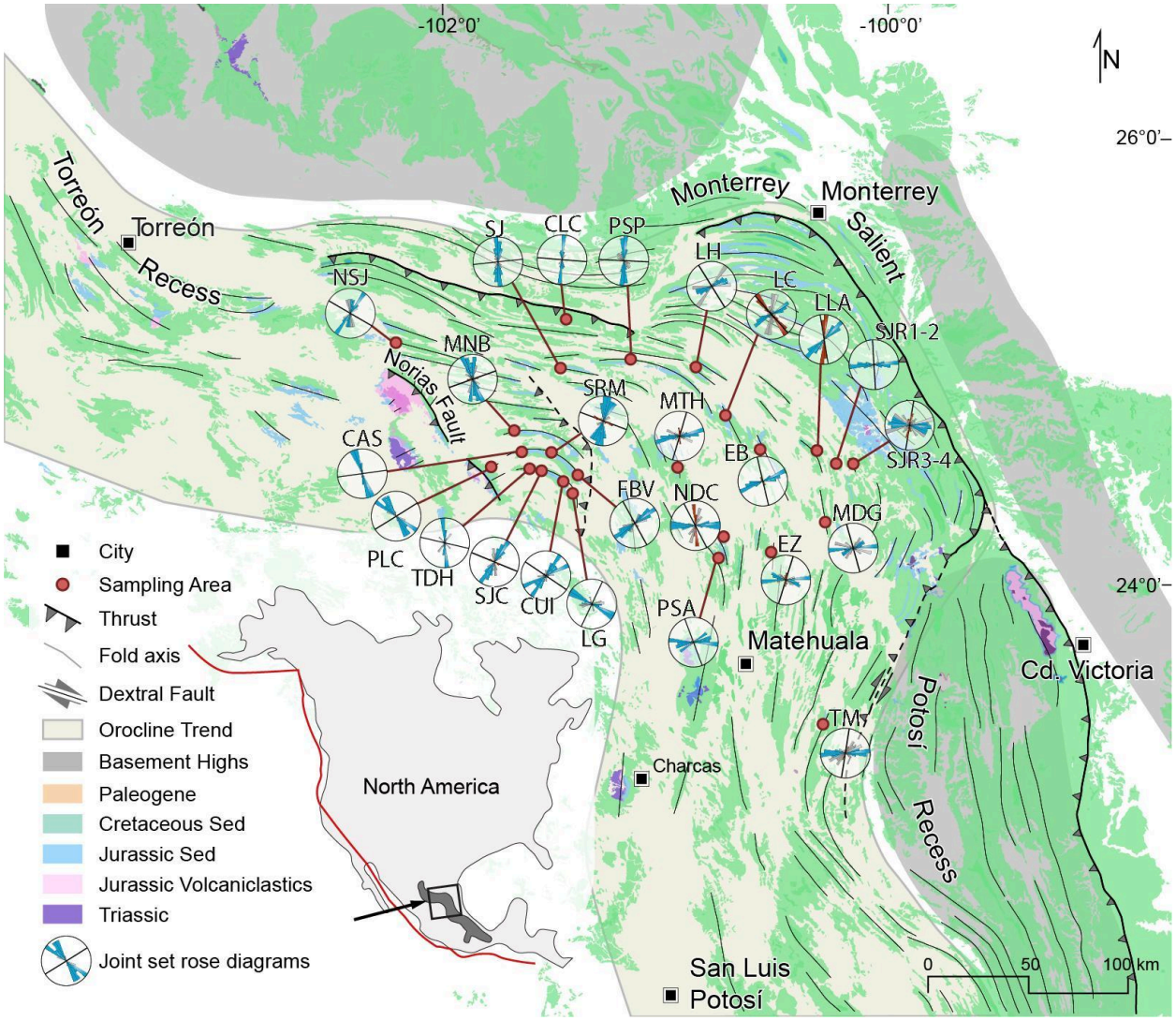

Figure 4.8 Regional map of the joint sets in each sampling site. Note how all jointsets portray a fan-like pattern perpendicular to the structural trend of the orocline.

4.2.5 Paleomagnetism

The demagnetization analyses for the Taraises Fm. indicate that (ti-)magnetite is the magnetic carrier of the ChRM in all samples evidenced by maximum unblocking temperatures of 480–520 °C and alternating magnetic fields of 60–90 mT (Figure 4.9 B). Whereas most samples decay straight or close to the origin, some samples analyzed in AF did not. Recovering any further components was impossible since the behavior

became erratic from 60 mT. All localities show single polarity ChRM. In Geographic coordinates the ChRM component points from west to northeast and points down in all cases but 3 (MDG1, MTH2, SRM2; Table 4.2). One of the limbs of the studied anticlines (SRM2, Table 4.2) did not deliver enough directions (n = 4).

Overall the results from the Taraises Fm. are excellent. Of the 671 sampled cores, 90.6% yielded interpretable ChRM directions, and only 2.1% of the valid directions required great circle fitting using other samples' ChRM as set points. Most of the localities (45 out of 50, or 90%) met the criteria established by Deenen et al. (2011) for sediment localities (at least n = 7 and A95min ≤ A95 ≤ A95max), indicating that the sampled localities are good recorders of the geomagnetic field. The Deenen et al. (2011) VGP distribution criteria showed that four localities (LG1; PLC2; SJC1; SJR1) show parameters consistent with a single spot reading of the magnetic field (A95 < A95min). Those localities were kept for further analyses because when combined with their other limb, their statistical parameters become acceptable and could still inform us about vertical axis rotations. One locality (SRM2) shows a large scatter (k = 6, and A95 > A95max). The SRM2 result is primarily due to its low "n" and high "k" which undermines its meaning. Since I cannot precisely know the adequate structural correction, the full anticline was discarded for further analysis. Table 4.2 contains the statistical synthesis of each locality. The raw and interpreted data at the specimen level can be accessed in this thesis's digital annex 3.

Table 4.2. Taraises site mean directions in geographic coordinate system.

	N	Ns	mDec	mInc	k	a95	K	A95	A95		ΔDx	ΔIx	Pole Lng	Pole Lat	Coordinates	
Collection									Min	Max					Lat.	Long.
CAS1	13	13	291.77	60.65	46.88	6.12	25	8.46	4.3	16.29	11.4	7.28	204.79	31.66	24.6	-101.6
CAS2	13	13	299.54	66.48	51.49	5.83	27.6	8.03	4.3	16.29	12.3	5.93	213.06	36.38	24.6	-101.7
CLC1	15	15	328.79	10.89	58.63	5.04	61	4.94	4.06	14.89	4.96	9.61	140.42	54.23	25.2	-101.5
CLC2	16	17	250.68	48.39	19.48	8.57	14.8	9.93	3.96	14.3	11.4	11.5	200.7	-0.76	25.2	-101.4
CUI1	14	14	290.41	58.98	61.09	5.13	33.2	7	4.18	15.55	9.12	6.29	201.99	30.96	24.5	-101.6
CUI2	8	10	346.58	37.61	17.46	13.63	17.5	13.6	5.22	22.12	14.6	19.6	83.16	84.8	24.5	-101.6
EB1	11	14	359.21	13.72	29.72	8.51	43.4	7.01	4.6	18.1	7.06	13.4	119.96	73.41	24.6	-100.6
EB2	8	10	307.53	35.98	29.66	10.34	29.9	10.3	5.22	22.12	11	15.3	188.58	48.82	24.6	-100.5
EZ1	11	14	331.52	32.77	5.74	20.88	11.3	14.2	4.6	18.1	15	22.2	146.92	56.98	24.1	-100.5
EZ2	14	14	55.98	21.91	47.78	5.81	66.5	4.91	4.18	15.55	5.01	8.79	352.34	35.54	24.1	-100.5
FBV1	13	14	288.71	31.32	23.09	8.81	36	7.01	4.3	16.29	7.33	11.2	180.84	22.99	24.5	-101.4
FBV2	9	9	306.82	49.04	44.91	7.77	39.9	8.26	4.98	20.54	9.54	9.45	188.91	42.96	24.5	-101.4
LC1	11	11	8.09	18.66	10.64	14.68	13.7	12.8	4.6	18.1	13	23.6	53.25	75.03	24.7	-100.7
LC2	9	9	329.28	28.83	47.83	7.52	43.5	7.9	4.98	20.54	8.19	13	157.15	59.87	24.8	-100.7
LG1	15	15	42.50	34.37	134.9	3.3	143	3.21	4.06	14.89	3.39	4.88	347.86	50.33	24.4	-101.4
LG2	12	13	27.93	9.99	17.08	10.81	23.4	9.17	4.44	17.14	9.21	17.9	14.18	55.08	24.4	-101.4
LH1	10	10	265.21	66.81	28.83	9.15	12.7	14.1	4.78	19.22	22	10.3	217.5	16.55	25.0	-100.9
LH2	10	11	340.87	67.59	29.28	9.08	14.8	13	4.78	19.22	20.7	9.32	238.47	66.2	25.0	-100.9
LLA1	6	7	325.06	48.91	17.27	16.59	16.3	17.1	5.86	26.52	19.8	19.7	207.23	63.03	24.6	-100.3
LLA2	6	10	358.64	56.34	11.53	20.6	6.59	28.2	5.86	26.52	36.2	27.1	345.16	55.31	24.6	-100.3
MDG1	11	13	52.43	-12.75	15.5	11.98	22.1	9.94	4.6	18.1	10	19.2	10.75	19.7	24.3	-100.3
MDG2	14	15	256.10	27.90	20.33	9.03	38.4	6.49	4.18	15.55	6.72	10.9	192.29	-3.3	24.3	-100.3
MNB1	15	16	269.07	53.67	107.3	3.71	62.1	4.89	4.06	14.89	5.92	5.02	203.7	11.08	24.7	-101.7
MNB2	15	17	283.27	66.73	48.85	5.53	19.2	8.95	4.06	14.89	13.8	6.57	207.58	23.07	24.7	-101.7
MTH1	14	16	8.71	2.02	4.59	20.9	9.61	13.5	4.18	15.55	13.5	27	61.76	58.39	24.5	-101.0
MTH2	15	17	249.35	-26.84	10.17	12.61	14.7	10.3	4.06	14.89	10.7	17.5	156.88	-21.46	24.5	-101.0
NDC1	9	9	1.90	54.69	76.86	5.91	52.5	7.17	4.98	20.54	8.79	7.18	265.66	78.34	24.2	-100.7
NDC2	11	12	358.81	50.78	21.92	9.97	14.3	12.5	4.6	18.1	14.7	13.7	286	80.37	24.2	-100.7
NSJ1	11	11	171.66	18.76	24.58	9.4	40.4	7.27	4.6	18.1	7.38	13.4	272.06	-53.91	25.1	-102.2
NSJ2	9	11	263.23	65.29	50.86	7.29	27.1	10.1	4.98	20.54	15	7.67	212.71	23.45	25.1	-102.2
PLC1	11	11	286.26	27.00	20.88	10.23	22.3	9.88	4.6	18.1	10.2	16.7	175.17	21.12	24.5	-101.8
PLC2	13	13	299.59	42.93	186.7	3.04	165	3.24	4.3	16.29	3.57	4.22	182.41	35.7	24.5	-101.8
PSA1	11	11	359.67	39.90	52.7	6.35	59.8	5.96	4.6	18.1	6.46	8.24	102.51	88.84	24.1	-100.8
PSA2	9	9	5.88	40.92	27.47	10	21.8	11.3	4.98	20.54	12.3	15.3	352.97	84.96	24.1	-100.8
PSP21	12	13	244.27	32.59	50.97	6.14	68.1	5.3	4.44	17.14	5.56	8.29	196.12	-9.24	25.0	-101.2
PSP21	9	9	298.52	26.42	50.48	7.32	62.4	6.57	4.98	20.54	6.77	11.2	170.55	31.57	25.0	-101.2
SJ1	12	14	286.15	50.25	37.68	7.16	31	7.93	4.44	17.14	9.26	8.82	199.98	30.14	25.0	-101.5
SJ2	16	16	289.46	34.74	6.82	15.25	11.2	11.5	3.96	14.3	12.2	17.4	181.28	27.51	25.0	-101.5
SJC1	13	13	295.76	33.99	151.3	3.38	136	3.57	4.3	16.29	3.77	5.47	176.59	30.53	24.5	-101.5
SJC2	12	12	314.19	19.72	28.71	8.24	38.7	7.07	4.44	17.14	7.18	12.9	159	44.42	24.4	-101.5
SJR1	10	10	44.15	10.03	122.5	4.38	150	3.96	4.78	19.22	3.97	7.74	7.12	43.41	24.5	-100.2
SJR2	11	11	327.52	18.06	12.3	13.56	16.6	11.6	4.6	18.1	11.7	21.5	149.62	56.11	24.6	-100.2
SJR3	12	13	47.95	25.32	38.31	7.1	61.9	5.56	4.44	17.14	5.71	9.6	354.26	39.54	24.5	-100.2
SJR4	7	7	280.48	5.03	22.12	13.12	38.2	9.89	5.51	24.07	9.9	19.7	167.75	10.61	24.5	-100.2
SRM1	8	8	255.63	43.32	22.93	11.82	24.4	11.4	5.22	22.12	12.7	14.8	198.54	-1.4	24.6	-101.5
SRM2	4	4	322.67	-19.72	5.99	41	6.15	40.4	6.89	34.24	41.1	73.8	129.36	39.26	24.6	-101.5
TDH1	15	15	306.65	33.63	19.74	8.83	16.9	9.59	4.06	14.89	10.1	14.8	172.44	40.72	24.5	-101.6
TDH2	13	15	319.73	38.87	7.2	16.61	9.92	13.9	4.3	16.29	15	19.5	179.57	61.6	24.5	-101.6
TM1	14	14	21.26	38.15	46.66	5.88	35.2	6.79	4.18	15.55	7.3	9.7	350.66	70.03	23.4	-100.3
TM2	7	10	345.84	38.34	55.22	8.19	50.9	8.54	5.51	24.07	9.19	12.2	203.84	55.52	23.4	-100.3

N number of demagnetized Specimens. Ns number of specimens that passed the Cutoff. mDec mean declination. mInc mean inclination. k precision parameter. a95 radius of the 95% confidence cone about site-mean direction.K precision paramenter of the poles. A95 radius of 95% confidence circle around paleomagnetic pole. A95min and A95max describe the minimum and maximun values of A95 allowed to considered the average representative. ΔDx. uncertainty in declination; ΔIx. uncertainty in inclination

4.3 Critical Reassessment of the Nazas Province Paleomagnetics

Only two main datasets were acquired at the specimen level from the compiled data (Nova-Rodríguez, 2016; Rodríguez-Parra, 2020). These datasets were re-analyzed and reinterpreted to avoid relying on previous interpretations and to better understand the behavior of the remanence measured. These studies include rock magnetic properties (IRM and Curie curves), AMS data, SEM Micrographs, and Paleomagnetism in three localities Real de Catorce, Charcas, Huizachal Valley (Nova-Rodríguez, 2016), and Villa Juárez (Rodríguez-Parra, 2020). These are my findings.

4.3.1 Real de Catorce

Paleomagnetism

The Data that was obtained from this locality show samples with a single ChRM component that gradually demagnetized to the origin (Figure 4.9 A) These samples show directions that group around two directions, (1) 358°/40° (Dec/Inc) downwards and k=45 (K=41, A95 = 2.79). This direction fits with the expected GAD of the Holocene for México. (2) the second is a reversed polarity dec/inc = 166°/42° with a k of 41 (K=37; A95 = 2.49; Figure 4.8 B). These directions do not share a bootstrapped common true mean direction (Tauxe, 2010) but are very close to it with a difference in the reversed component of <10° (rotated counterclockwise). The VGPs projection shows a round shape indicative of no other sources of scatter (Figure 4.9 B). By flipping the reversed direction, we obtain a mean dec/inc of 346°/43° k = 41, K =37, A95 = 2.49 (Table 1, See also Table 4.3 for site level directions).

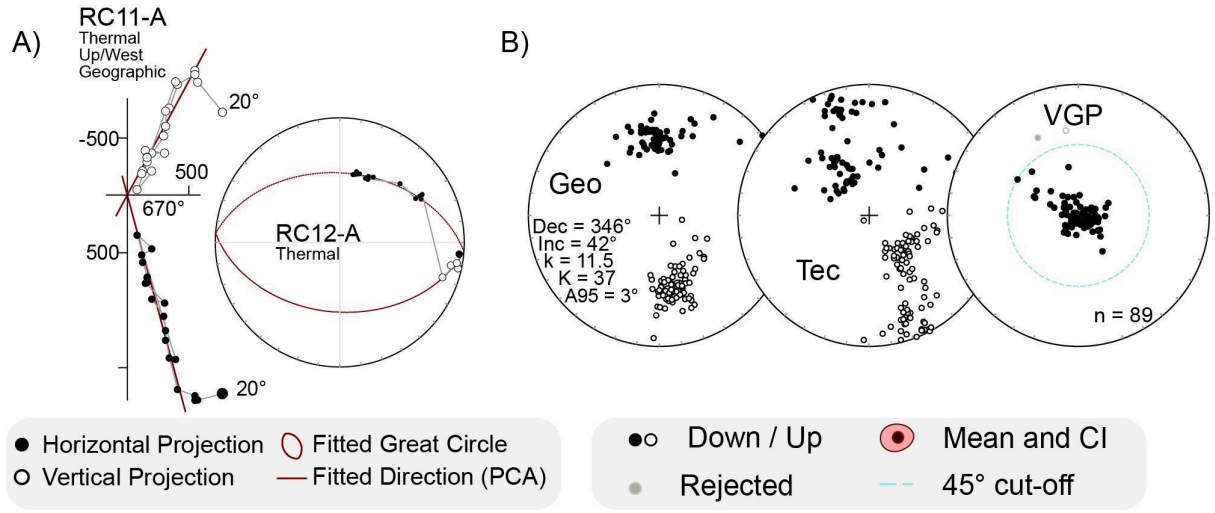

Figure 4.9 (A) Representative direction from the samples collected in Real de Catorce expressed in Zijderveld's (1967) diagram and fitted great circle. (B) Stereogram plots of the directions. (Geo/Tec) = Geographic/Tectonic Coordinate system. VGP= Virtual Geomagnetic Pole. Thermal = Thermal Demagnetization. PC = Principal Component. Site Means are listed in Table 4.3.

4.3.2 Charcas

Anisotropy of Magnetic Susceptibility

In Charcas the susceptibility (km) varies from 1.209 x 10^{-4} to 3.353 x 10^{-4} with a mean value of 2.078 x 10^{-4} and a P = 1.24. Regarding their geometry, sites CHA1, CHA2, CHA4, CHA9, and CHA10 show oblate shapes. CHA3, CHA5, and CHA8 show both prolate and oblate, and CHA6 and CHA7 only show prolate geometries (Figure 4.10). With the exception of sites CHA2, CHA3, and CHA6 K_{min} axes are parallel to the poles of the bedding. This is indicative that the AMS in Charcas responds, at least partially, to loading (Figure 4.10 Charcas).

Table 4.3 Real de Catorce site mean directions in geographic coordinate system.

	N	Ns	mDec	mInc	k	a95	K	A95	A95		ΔDx	ΔIx	Pole Lng	Pole Lat	Coordinates	
Geographic									Min	Max					Lat.	Long.
RC11-R	5	5	162.9	-33	133	6.66	246	4.88	6.3	29.75	5.14	7.59	333.28	-73.12	23.7	-100.9
RC11-N	3	3	354.4	46.44	40.72	19.57	26.7	24.4	7.73	41.04	27.77	29.52	208.76	83.39	23.7	-100.9
RC12-R	7	7	162.8	-40	399.4	3.02	601	2.46	5.51	24.07	2.67	3.4	349.44	-74.25	23.7	-100.9
RC13-R	9	9	171.3	-39.6	217.6	3.5	221	3.47	4.98	20.54	3.75	4.83	342.58	-81.88	23.7	-100.9
RC14-R	5	5	160.5	-42	282.6	4.56	349	4.1	6.3	29.75	4.5	5.45	355.14	-72.09	23.7	-100.9
RC14-N	2	2	22.62	57.54	167.7	19.41	141	21.2	9.09	52.99	27.37	19.76	306.29	65.84	23.7	-100.9
RC15-R	6	6	136.9	-52.6	82.27	7.43	46.9	9.88	5.86	26.52	11.84	10.41	13.33	-50.93	23.7	-100.9
RC15-N	2	2	356.2	29.94	8.77	98.54	11.5	82.3	9.09	52.99	NaN	133.8	116.56	81.67	23.7	-100.9
RC16-R	6	6	151.9	-59	49.98	9.57	29.3	12.6	5.86	26.52	16.47	11.28	31.04	-60.49	23.7	-100.9
RC16-N	1	1	348.4	30.32	0	NaN	NaN	NaN	12	82	NaN	NaN	137.06	76.83	23.7	-100.9
RC17-R	7	7	175.4	-49.4	120.9	5.51	85.3	6.57	5.51	24.07	7.61	7.47	48.74	-82.21	23.7	-100.9
RC17-N	6	6	20.56	26.61	94.73	6.92	160	5.31	5.86	26.52	5.47	9.02	11.61	68.47	23.7	-100.9
RC18-R	6	6	174.1	-46.1	118.3	6.18	104	6.59	5.86	26.52	7.44	8.04	26.92	-83.16	23.7	-100.9
RC19-R	6	7	170.5	-43.7	71.58	7.97	73.2	7.88	5.86	26.52	8.74	10.13	26.1	-74.72	23.7	-100.9
RC21-R	6	6	173.1	-42	511.5	2.97	673	2.59	5.86	26.52	2.84	3.43	356.29	-83.7	23.7	-100.9
RC22-R	5	5	163.8	-44.2	90.86	8.07	71.2	9.13	6.3	29.75	10.16	11.59	1.66	-74.83	23.7	-100.9
RC23-R	6	6	170.9	-36.7	133.1	5.83	135	5.79	5.86	26.52	6.18	8.48	329.79	-81.14	23.7	-100.9
RC24-R	6	6	171.2	-31.7	16.91	16.77	24.3	13.9	5.86	26.52	14.52	22	320.29	-79.43	23.7	-100.9
RC25-R	4	4	169.3	-34.9	128.1	8.15	131	8.04	6.89	34.24	8.52	12.14	327.36	-79.07	23.7	-100.9
RC26-R	5	6	175.8	-40	301.8	4.41	280	4.58	6.3	29.75	4.96	6.32	57.31	-79.94	23.7	-100.9

N number of demagnetized specimens, Ns number of specimens that passed the cutoff, mDec mean declination, mInc mean inclination, k precision parameter, a95 radius of the 95% confidence cone about site-mean direction,K precision paramenter of the poles, A95 radius of 95% confidence circle around paleomagnetic pole, A95min and A95max describe the minimum and maximun values of A95 allowed to consider the average representative. ΔDx, uncertainty in declination; ΔIx, uncertainty in inclination

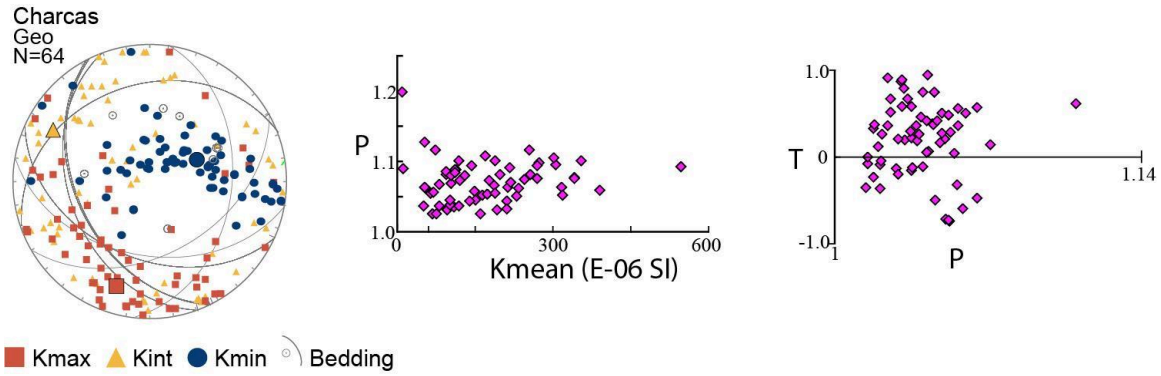

Figure 4.10 Anisotropy of Magnetic Susceptibility of the Charcas locality. Results are represented in equal-area projections for the analyzed sites. Larger symbols represent site means. Grey lines represent structural data. Graphs are shape parameter (P) vs. Mean magnetic susceptibility and Shape parameter T vs. Anisotropy parameter P show degree of anisotropy.

Paleomagnetism

The re-evaluation of the Charcas directions show that some sites demagnetize to the origin with more than 10 demagnetization steps (CHA1, 9, and 10, 17 samples; e.g. Figure 4.11 A; Table 4.4) with low MAD (< 5). Other samples (CHA3, 4, 5, and 6, 22 samples) show little AF demagnetization, due to the presence of hematite, but all of them show tendencies to the origin with analogous directions to CHA9 and CHA10. The characteristic component was isolated between 35 and 90 mT. CHA3 to CHA10 group well with a dec/inc = 22°/-05° and k = 53; K = 76; and A95 = 2.58 (Figure 4.11B; Table 4.4). Samples from sites CHA1 and 2 were discarded by the 45° cut-off (Figure 4.11 B). The dispersion parameter before tectonic correction was > 50 and K > 70 after tectonic correction, in both specimen and site mean averages (Table 4.4). This may suggest that the samples from sites ChA3-10 may have recorded a single spot-reading of the geomagnetic field. Either because all sampled layers represent a single cooling unit (extruded at the same time) or because they were quickly remagnetized later.

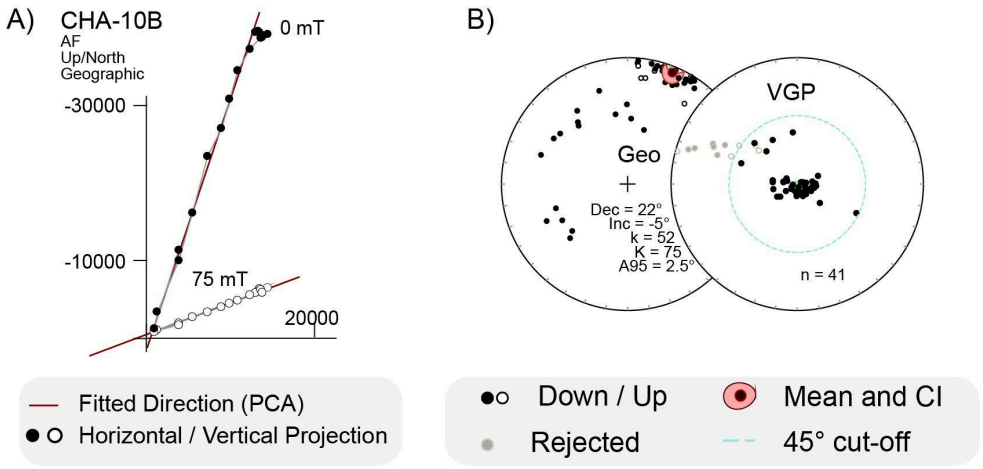

Figure 4.11 A) Representative direction from the data in Charcas expressed in Zijderveld's (1967) diagram. (B) Stereogram plots of the directions. **Geo** = Geographic Coordinate system. **VGP**= Virtual Geomagnetic Pole. **AF** = Alternating Fiends Demagnetization. **PC** = Principal Component (Site Means are listed in Table 4.4).

Table 4.4 Charcas site mean directions in geographic coordinate system.

	N	Ns	mDec	mInc	k	a95	K	A95	A95		ΔDx	ΔIx	Pole Lng	Pole Lat	Coordinates	
Geographic									Min	Max					Lat.	Long.
CHA1	5	6	238.9	38.67	73.98	8.95	62	9.79	6.3	29.75	10.55	13.85	203.9	-16.97	23.11	-101.2
CHA2	7	11	135.5	-33.5	25.19	12.26	21.9	13.2	5.51	24.07	13.9	20.36	347.31	-13.16	23.11	-101.2
CHA3	5	5	9.97	3.86	245.2	4.9	278	4.59	6.3	29.75	4.6	9.16	52.84	66.73	23.1	-101.2
CHA4	6	6	23.31	-4.8	66.8	8.26	106	6.54	5.86	26.52	6.55	13.02	34.07	55.83	23.1	-101.2
CHA5	6	6	26.44	-10.1	91.94	7.02	155	5.4	5.86	26.52	5.42	10.55	33.03	51.68	23.1	-101.2
CHA6	4	5	25.92	-2.79	123.9	8.29	191	6.67	6.89	34.24	6.68	13.32	15.17	45.93	23.1	-101.2
CHA7	6	6	26.54	-5.54	114	6.3	207	4.67	5.86	26.52	4.67	9.27	30.36	53.4	23.1	-101.2
CHA8	4	4	29.92	-1.81	265.1	5.65	373	4.76	6.89	34.24	4.77	9.52	24.23	52.28	23.1	-101.2
CHA9	5	6	13.48	-14	79.25	8.65	89.1	8.15	6.3	29.75	8.21	15.58	37.92	53.34	23.1	-101.2
CHA10	5	5	20.63	-2.85	53.48	10.56	82	8.5	6.3	29.75	8.5	16.96	36.69	58.3	23.1	-101.2

N number of demagnetized specimens, Ns number of specimens that passed the Cutoff, mDec mean declination, mInc mean inclinationg, k precision parameter, a95 radius of the 95% confidence cone about site-mean direction,K precision paramenter of the poles, A95 radius of 95% confidence circle around paleomagnetic pole, A95min and A95max describe the minimum and maximun values of A95 allowed to considered the average representative. ΔDx, uncertainty in declination; ΔIx, uncertainty in inclination

4.3.3 Huizachal Valley

Paleomagnetism

The Paleomagnetic data from the Huizachal Valley shows a component isolated in the temperatures between 450 °C and 650 °C (e.g. Figure 4.12 A). That by combining 57 directions with 33 great circles (McFadden & McElhinny, 1988) the component shows a mean dec/inc of 157°/-21° upwards with a k = 14, K = 22, and A95 = 3° (Flipped in Figure 4.12 and Table 1, Supplementary Table 5). The VGPs projection shows a roughly circular shape with a slight ellipticity W-E possibly indicating tectonic-induced scatter (Figure 7D).

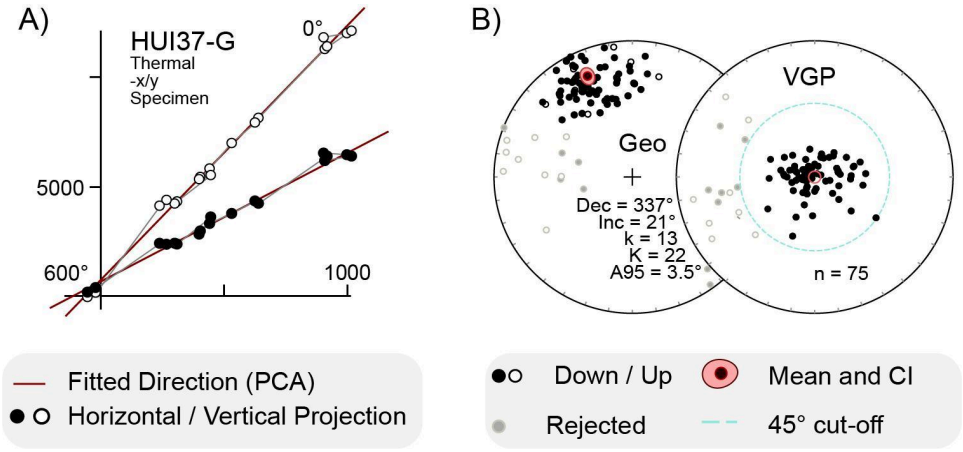

Figure 4.12 A) Representative direction from the data in Huizachal Valley expressed in Zijderveld's (1967) diagram. (B) Stereogram plots of the directions. **Geo** = Geographic Coordinate system. **VGP**= Virtual Geomagnetic Pole. **AF** = Alternating Fields demagnetization. **PC** = Principal Component (Site Means are listed in Table 4.5).

Table 4.5. Huizachal site mean directions in geographic coordinate system.

	N	Ns	mDec	mInc	k	a95	K	A95	A95		ΔDx	ΔIx	Pole Lng	Pole Lat	Coordinates	
Geographic									Min	Max					Lat.	Long.
HUI28	5	5	155.1	-26	22.97	16.31	31.9	13.8	6.3	29.75	14.17	23.55	333.94	-64.25	23.59	-99.22
HUI29	6	6	98.71	3.74	21.35	14.84	28.6	12.8	5.86	26.52	12.76	25.42	345.59	-7.23	23.59	-99.22
HUI31	5	5	147.6	-30.6	54.51	10.46	55.7	10.3	6.3	29.75	10.79	16.67	343.73	-59.13	23.59	-99.22
HUI32-5	6	7	113.2	-1.76	4.42	35.98	10.5	21.7	5.86	26.52	21.71	43.38	331.83	-18.81	23.59	-99.22
HUI35	7	7	121	20.77	8.6	21.83	13.5	17.1	5.51	24.07	17.37	30.9	326.22	-22.56	23.59	-99.22
HUI36	7	7	86.12	7.99	9.54	20.6	18.1	14.6	5.51	24.07	14.61	28.72	348.02	5.31	23.59	-99.22
HUI37	6	6	158.6	-33.7	88.31	7.17	127	5.96	5.86	26.52	6.29	9.16	340.85	-69.65	23.59	-99.22
HUI38	7	7	164.5	-36.3	25	12.31	24.2	12.5	5.51	24.07	13.36	18.45	341.48	-75.58	23.59	-99.22
HUI40	7	7	86.05	12.42	18.67	14.34	26.2	12	5.51	24.07	12.09	23.2	346.44	6.55	23.59	-99.22
HUI42	6	7	357	60.25	24.69	13.75	12.9	19.4	5.86	26.52	26.21	16.88	254.54	65.25	23.58	-99.23
HUI43	4	4	149.9	-10.7	70.77	11	138	7.84	6.89	34.24	7.87	15.28	323.53	-55.76	23.58	-99.23
HUI44	5	5	175.7	-29.8	46.94	11.28	52.1	10.7	6.3	29.75	11.13	17.44	291.7	-81.44	23.58	-99.23
HUI45	5	5	357.4	43.1	56.51	10.27	58.8	10.1	6.3	29.75	11.12	13.07	209.67	86.42	23.58	-99.23
HUI46	5	5	150.6	-21	38.28	12.52	38.7	12.5	6.3	29.75	12.68	22.51	331.42	-59.31	23.58	-99.23
HUI47	5	6	164.9	-21.4	39.98	12.25	53.4	10.6	6.3	29.75	10.77	19.03	312.25	-66.06	23.58	-99.24
HUI48	6	7	161.6	-17.6	12.27	19.91	19	15.8	5.86	26.52	15.99	29.42	323.85	-65.65	23.58	-99.24

N number of demagnetized Specimens, Ns number of specimens that passed the Cutoff, mDec mean declination, mInc mean inclination, k precision parameter, a95 radius of the 95% confidence cone about site-mean direction,K precision paramenter of the poles, A95 radius of 95% confidence circle around paleomagnetic pole, A95min and A95max describe the minimum and maximun values of A95 allowed to considered the average representative. ΔDx, uncertainty in declination; ΔIx, uncertainty in inclination

4.3.4 Villa Juárez

Thermomagnetic Curves

The Data retrieved from this locality show irreversible curves in the Thermomagnetic runs, these results are indicative of mineralogical alterations during heating a drop in susceptibility is noticed in most of the curves around the Curie temperature for low Ti-magnetite (~580 °C, Annex 4.6). In some cases a subtle drop around the Néel temperature of hematite is also observed (~700 °C; Figure 4.13 A).

IRM

In the Villa Juárez locality eleven samples were analyzed to obtain IRM acquisition curves. Four samples were composed of andesitic and tuff (NA01, NA02, NA05, and NA10), and the samples labeled NA04, NA06, NA07, NA08 were of volcano-sedimentary composition. The Gradient Acquisition Plots (GAP) show a component with a mid-saturation value log $B_{1/2}$ between 2.85 and 3 (Figure 4.13 B), and a second one between 1.7 and 2 (Figure 4.13 C). The majority of the results show a gradual increment towards 1 T and higher but do not reach saturation at 3 T. The main contribution to the coercivity spectra is given by the log $B_{1/2}$ >100 mT and <1000 mT. This is usually accredited to phases of hematite, which is present in both volcanic and volcano-sedimentary rocks of this locality. The complete set of the IRM unmixing graphs is available in Annex 4.7.

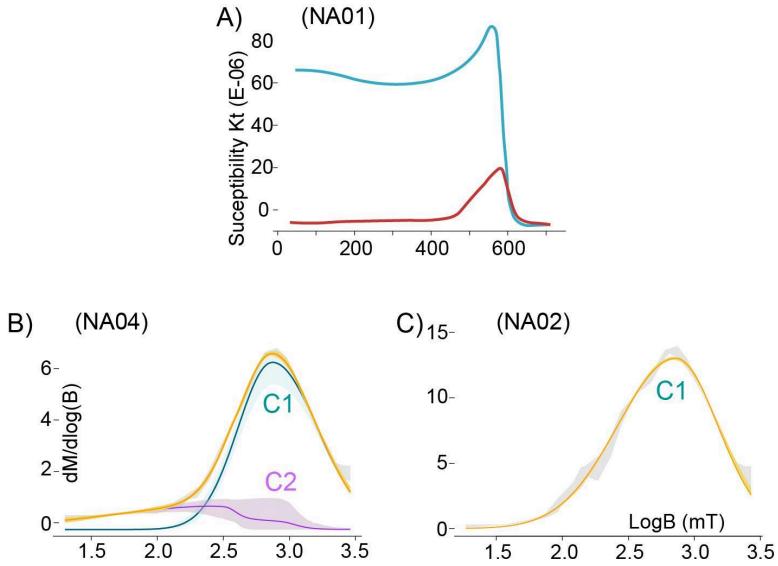

Figure 4.13 A) Magnetic susceptibility (Kt) versus temperature (°C) graph from Villa Juárez locality data that shows Hematite magnetic carrier red/blue line represents heating/cooling runs, respectively. B) and C) graphs are Gradient Acquisition plots of the IRM acquisition curves also from the data acquired from the Villa Juárez locality using MAX UnMix (Maxbauer et al., 2016). Smoothed IRM data and modeled coercivity distribution are represented by the gray dots and the yellow curve, respectively. 95% confidence intervals associated with each component are represented by the shaded areas. The plots show mid saturation (B1/2) of 1.7 for (B) and 2.85 for (C), indicative of magnetite, and hematite phases, respectively.

Anisotropy of Magnetic Susceptibility

The AMS results in this locality show anisotropy values that vary per site from 1.95 x 10^{-05} to 1.59 x 10^{-04} with mean values of 7.36 x 10^{-05}. The majority of the sites show oblate shapes and low degrees of anisotropy (P = 1.026; Figure 4.14). The AMS ellipsoid projections show widespread distribution and poor grouping (Figure 4.14), this behavior is indicative of faintly or undeformed volcanic rocks, which is consistent with field observations.

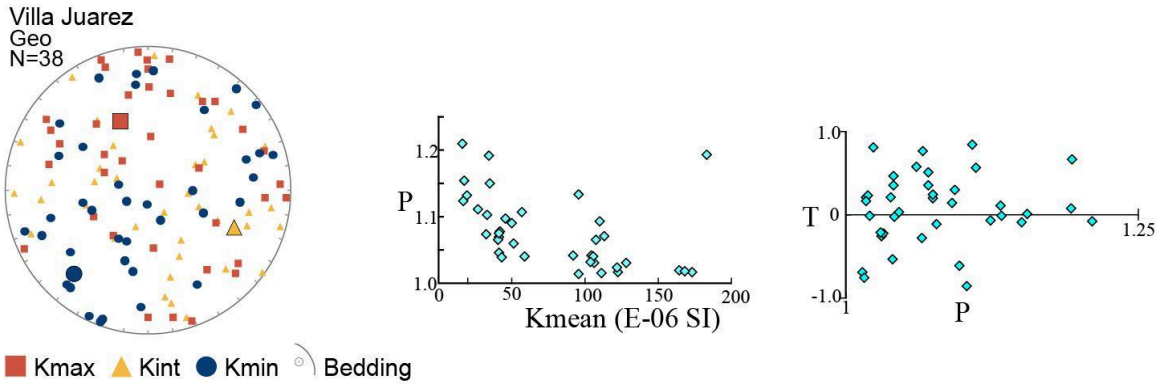

Figure 4.14 Anisotropy of Magnetic Susceptibility of the Villa Juárez locality. Results are represented in equal-area projections for the analyzed sites. Larger symbols represent site means. Graphs are shape parameter (P) vs. Mean magnetic susceptibility and Shape parameter T vs. Anisotropy parameter P show degree of anisotropy.

Scanning Electron Microscopy

The data contained SEM images with EDS (Energy Dispersive Spectroscopy). The images for this locality show the presence of Ti-Magnetite in a non-conductive granular matrix and lamellar hematite crystals (Figure 4.15).

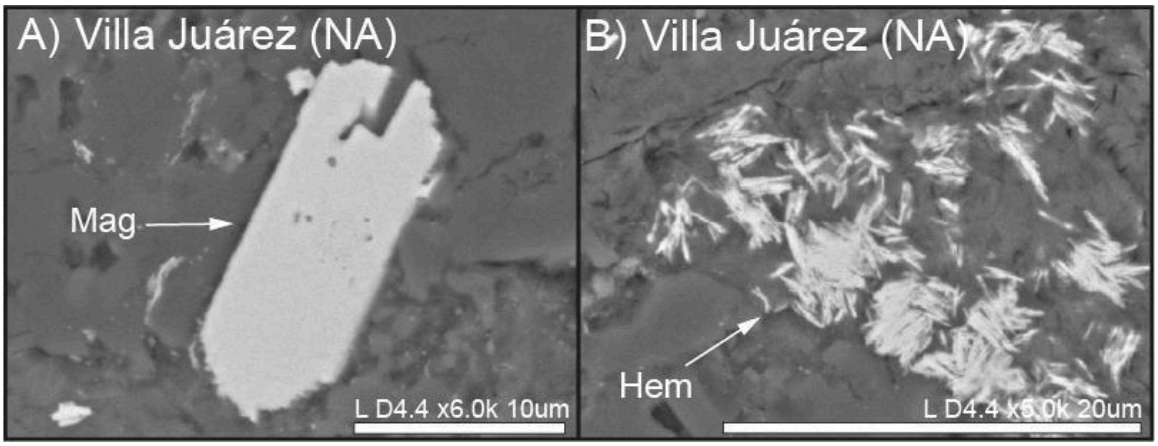

Figure 4.15 Scanning Electron photomicrographs of representative samples of the Nazas Fm. from the Villa Juárez locality. Samples show compositions and texture of primary magnetite, Ti-magnetite, and hematite.

Paleomagnetism

In this locality the Paleomagnetic directions in the Zijderveld diagrams show a single component that progressively demagnetizes to the origin (Figure 4.16 A). The ChRM components were isolated at temperatures of ~450 – 700 °C. At the site level, 5 out of 10 sites show k > 100 with n > 3 samples. The majority of the directions show high precision parameters but three (k > 45). All sites in this locality were considered spot readings of the geomagnetic field. However, none of the site averages concentrate in a reliable direction (Figure 4.16 B) (k < 2, without a cut-off and k = 13 after discarding more than half of site averages). This dataset is too scarce to confirm whether some site directions may represent reversed chrons or not. For this reason, no mean dec/inc was obtained from this locality (See Table 4.6)

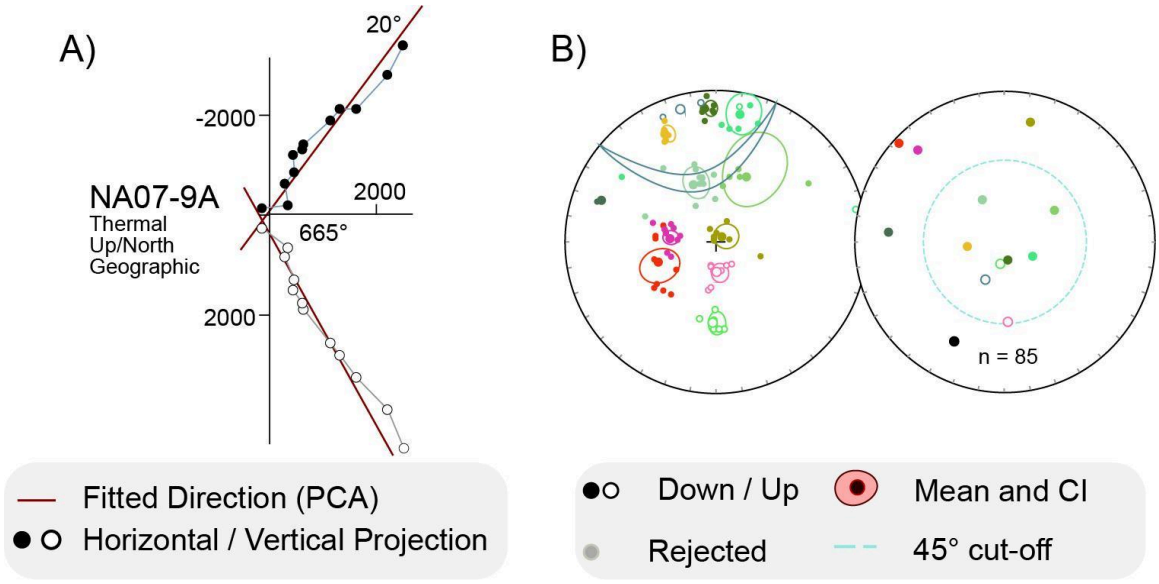

Figure 4.16 A) Representative direction from the data in the Villa Juárez locality expressed in Zijderveld's (1967) diagram. (B) Stereogram plots of the directions in Geographic Coordinate system. Note that there is no preferential grouping in this locality. VGP= Virtual Geomagnetic Pole. Thermal = Thermal Demagnetization. PC = Principal Component (Site Means are listed in Table 4.6).

Table 4.6 Villa Juarez site mean directions in geographic coordinate system.

	N	Ns	mDec	mInc	k	a95	K	A95	A95		ΔDx	ΔIx	Pole Lng	Pole Lat	Coordinates	
Geographic									Min	Max					Lat.	Long.
NA-01	10	10	241.3	52.53	32.09	8.66	19.35	11.26	4.78	19.22	13.49	11.89	208.42	-6.39	25.495	-103.6
NA-02	11	11	263.1	62.28	136.1	3.93	67.28	5.61	4.6	18.1	7.75	4.62	209.16	12.61	25.495	-103.6
NA-03	8	8	152	-78.43	125.2	4.97	39.32	8.94	5.22	22.12	24.23	5.01	62	-44.09	25.495	-103.6
NA-04	6	6	175	-51.85	167.5	5.19	127.5	5.96	5.86	26.52	7.06	6.39	46.98	-81.64	25.497	-103.6
NA-05	6	8	9.6	10.73	29.75	12.49	72.54	7.92	5.86	26.52	7.95	15.43	48.58	68.79	25.492	-103.6
NA-06	7	7	0.02	30.98	156.7	4.84	345.1	3.25	5.51	24.07	3.4	5.22	76.2	81.35	25.498	-103.6
NA-07	12	12	305.1	65.84	36.52	7.28	20.82	9.74	4.44	17.14	14.68	7.32	211.14	42.42	25.519	-103.6
NA-08	5	5	14.41	58.14	18.9	18.06	11.78	23.26	6.3	29.75	30.45	21.35	289.06	73.02	25.511	-103.6
NA-10	8	8	257.4	83	58.89	7.28	17.26	13.72	5.22	22.12	83.97	7.16	241.6	21.96	25.508	-103.6
NA-12	2	2	344.6	24.8	46.6	37.45	47.4	37.12	9.09	52.99	38.27	64.44	128.09	71.04	25.526	-103.6
NA-13	1	1	277.4	12.98	0	NaN	NaN	NaN	12	82	NaN	NaN	169.15	9.51	25.544	-103.6
NA-17	5	5	331.9	33.15	224.3	5.12	404.8	3.81	6.3	29.75	4.01	5.91	156.34	62.89	25.516	-103.6

N number of demagnetized specimens, Ns number of specimens that passed the Cutoff, mDec mean declination, mInc mean inclinationg, k precision parameter, a95 radius of the 95% confidence cone about site-mean direction, K precision paramenter of the poles, A95 radius of 95% confidence circle around paleomagnetic pole, A95min and A95max describe the minimum and maximun values of A95 allowed to consider the average representative. ΔDx, uncertainty in declination; ΔIx, uncertainty in inclination.

4.4 Data Summary

13 robust directions were obtained after the rigorous depuration of the data found in the literature and the critical reassessment of the data obtained from Nova-Rodríguez (2016) and Rodríguez-Parra (2021), and the contribution of this thesis summarises a total of 66 mean directions within the contemporary consensus criteria of modern paleomagnetic studies. The final directions used in the final calculations and interpretations are listed in Table 4.2 and Table 4.7.

Table 4.7. Final Mean directions used for interpretation in geographic and tectonic coordinate systems.

	N	Ns	mDec	mInc	k	a95	K	A95	A95 Min	A95 Max	ΔDx	ΔIx	Pole Lng	Pole Lat	Coordinates Lat.	Coordinates Long.	R	ΔR
Geographic																		
A) Mina San Miguel	91	101	285.76	20.95	10.15	4.9	17.5	3.65	1.97	4.78	3.72	6.6	175.72	16.44	24.8939	-102.15	-60.653	5.48967
Caopas*	51	69	270.73	17.59	10.1	6.61	13.4	5.66	2.49	6.89	5.73	10.54	180.79	5.38	24.8343	-102.2	-75.337	6.67636
Nazas North*	25	37	272.53	21.41	11.56	8.9	12.61	8.49	3.31	10.79	8.65	15.28	186.14	0.17	24.9367	-102.24	-73.937	9.53666
B) Real de Catorce	89	91	346.91	42.95	41.41	2.36	37.13	2.49	1.99	4.85	2.75	3.25	185.05	77.02	23.7007	-100.89	3.10891	3.44578
C) Charcas	41	41	22.02	-5.05	52.98	3.1	75.96	2.58	2.72	7.9	2.58	5.13	36.02	56.55	23.0956	-101.17		
D) Huizachal	75	89	337.07	20.87	13.8	4.57	22.65	3.52	2.13	5.4	3.58	6.36	151.59	57.74	23.5873	-99.227		
NEM4-6	21	21	3.39	31.1	29.17	5.99	37.23	5.28	3.55	12.05	5.51	8.45	60.92	82.04	24.91	-99.927		
NEM-12/13	15	15	356.91	49.29	25.87	7.66	20.89	8.57	4.06	14.89	9.92	9.75	233.61	83.45	25.49	-100.36		
NEM-24/25	10	10	343.61	54.16	79.55	5.45	49.51	6.93	4.78	19.22	8.44	7.03	207.46	72.93	25.48	-100.42	2.50432	8.7913
NEM-26/27	13	13	287.84	44.68	69.29	5.02	73	4.88	4.3	16.29	5.45	6.15	188.07	26.21	25.39	-100.8	-53.092	6.96927
CLE-SR	86	91	55.31	37.58	13.87	4.25	14.47	4.16	2.02	4.96	4.45	5.99	339.11	41.19	25.1	-100.22	72.0859	4.47024
CLE-CT	47	47	317.06	45.44	50.96	2.94	43.72	3.18	2.57	7.25	3.57	3.94	182.96	51.66	25.1	-100.33	-25.705	4.28506
NOW-LOC2	27	27	336.79	44.16	31.24	5.05	26.91	5.46	3.21	10.28	6.07	6.94	175.02	69.03	25.27	-103.77		
NOW-LOC4	10	10	328.16	37.89	41.47	7.59	47.4	7.09	4.78	19.22	7.61	10.17	167.17	61.09	24.98	-103.25		
MG	8	9	341.63	3.94	30.79	10.14	49.41	7.96	5.22	22.12	7.96	15.86	110.53	60.65	26.5	-103	-7.3518	10.6421
GN	22	22	339.73	31.62	52.83	4.3	69.16	3.75	3.49	11.7	3.93	5.96	159.26	70.36	22.1	-101		
Tectonic																		
A) Mina San Miguel	73	101	294.81	35.17	7.45	6.53	8.79	5.94	2.16	5.49	6.3	8.92	185.79	32.91	24.8939	-102.15		
Caopas*	51	69	270.73	17.59	10.1	6.61	13.4	5.66	2.49	6.89	5.73	10.54	180.79	5.38	24.8343	-102.2		
Nazas North*	25	37	262.96	27.46	12.89	8.39	14.45	7.89	3.31	10.79	8.15	13.26	195.26	-9.64	24.9367	-102.24		
B) Real de Catorce	85	91	326.73	39.72	9.81	5.17	13.52	4.34	2.03	4.99	4.7	6.02	182.15	56.07	23.7007	-100.89		
C) Charcas	41	41	20.35	30.7	52.74	3.1	75.87	2.58	2.72	7.9	2.69	4.15	3.04	69.79	23.0956	-101.17	25.4401	3.89997
D) Huizachal	78	89	333.16	27.02	10.17	5.29	15.86	4.16	2.1	5.27	4.29	7.03	162.1	57.42	23.5873	-99.227	-10.736	6.47731
NEM4-6	14	21	9.83	-22.27	30.39	7.33	66.48	4.91	4.18	15.55	5.01	8.76	110.55	59.37	24.91	-99.927	14.5632	7.0272
NEM-12/13	15	15	356.91	49.29	25.87	7.66	20.89	8.57	4.06	14.89	9.92	9.75	233.61	83.45	25.49	-100.36	8.47855	10.5744
NEM-24/25	10	10	343.61	54.16	79.55	5.45	49.51	6.93	4.78	19.22	8.44	7.03	207.46	72.93	25.48	-100.42		
NEM-26/27	13	13	287.84	44.68	69.29	5.02	73	4.88	4.3	16.29	5.45	6.15	188.07	26.21	25.39	-100.8		
CLE-SR	86	91	55.31	37.58	13.87	4.25	14.47	4.16	2.02	4.96	4.45	5.99	339.11	41.19	25.1	-100.22		
CLE-CT	47	47	317.06	45.44	50.96	2.94	43.72	3.18	2.57	7.25	3.57	3.94	182.96	51.66	25.1	-100.33		
NOW-LOC2	27	27	336.79	44.16	31.24	5.05	26.91	5.46	3.21	10.28	6.07	6.94	175.02	69.03	25.27	-103.77	-6.8588	7.61847
NOW-LOC4	10	10	328.16	37.89	41.47	7.59	47.4	7.09	4.78	19.22	7.61	10.17	167.17	61.09	24.98	-103.25	-16.841	10.8618
MG	8	9	341.63	3.94	30.79	10.14	49.41	7.96	5.22	22.12	7.96	15.86	110.53	60.65	26.5	-103		
GN	22	22	339.73	31.62	52.83	4.3	69.16	3.75	3.49	11.7	3.93	5.96	159.26	70.36	22.1	-101	-10.794	6.87648

*N number of demagnetized specimens, Ns number of specimens that passed the Cutoff, mDec mean declination, mInc mean inclinationg, k precision parameter, a95 radius of the 95% confidence cone about site-mean direction,K precision paramenter of the poles, A95 radius of 95% confidence circle around paleomagnetic pole, A95min and A95max describe the minimum and maximun values of A95 allowed to consider the average representative. ΔDx, uncertainty in declination; ΔIx, uncertainty in inclination, R observed rotation in reference to the asumed time of magnetization adquisition. + (- Counter) Clockwise. A,B,C,D are referenced in Figure 2.1 * Locality shows high VGP elongation see text for detail.(* **NEM** *Nemkinet al., 2017; **CLE** : Clementet al.,2000; **NOW** = Nowicki et al.,1992; **MG** = Molina-Garza, 2004; **GN** = González-Naranjo et al.,2012.*

Chapter 5

The Sierra Madre Oriental Orocline: Significance & Kinematics

"Excellence is never an accident. It is always the result of high intention, sincere effort, and intelligent execution; it represents the wise choice of many alternatives – choice, not chance, determines your destiny."

— **Aristotle**

OVER the lifespan of mountain building processes, there are many mechanisms that can alter the physical-chemical properties of the rocks, and consequently their magnetic properties. These events are called remagnetizations and are a common phenomenon in orogens worldwide (e.g. the Alps (Pueyo et al., 2007), the Himalayas (Huang et al., 2017), the Variscan belt (Pastor-Galán et al., 2017). In a remagnetization event, a physical and/or chemical geological process completely or partially overprints the original natural remanent magnetization (NRM). Remagnetizations hinder the information that a rock can provide about its previous geological history, but it can offer crucial insights into orogenic kinematics (Weil et al., 2002; Gong et al. 2009; Izquierdo-Llavall et al. 2015).

5.1 Magnetizations Timeframe

Establishing the timing of such magnetization is of utmost importance to investigate the kinematics of vertical axis rotations. The Mesozoic and Cenozoic geological history of México includes many tectonic processes that directly or indirectly affected the Sierra Madre Oriental such as subduction, terrain accretion, large-scale deformation, and magmatism (Please see Centeno-García, 2017; Martini and Ortega-Gutiérrez, 2018; Fitz-Díaz et al., 2018). Each of these processes have the capability of overprinting the original magnetizations of the studied rocks. As of today, we do not have the means to obtain absolute dates for magnetizations, it is possible to establish a relative timing following field relationships between the magnetizations and geological features. For example, the Fold test also known as the “Tilt” test (Tauxe & Watson, 1994) evaluates timing of magnetization with regard to folding time. In general terms this procedure compares paleomagnetic direction data to determine the percentage of folding in which grouping is highest, thus, determining the time of magnetic acquisition. The tests

conducted are based on the eigenvector method described by Tauxe and Watson (1994), which involves calculating the maximum eigenvalue of the data's orientation matrix at each step within a defined unfolding range (typically from -50% to 150%). The highest eigenvalue found within this range is taken to indicate the greatest clustering of directions at the site, and the corresponding unfolding percentage is noted. This process is repeated for a chosen number of nonparametric bootstrap samples, each using N randomly selected directions from the original dataset. For each bootstrap, the unfolding percentage that produces the maximum eigenvalue is identified and the results are presented as a cumulative distribution function. The 95% confidence interval (shaded area) is determined by discarding the lower and upper 2.5% of sorted unfolding percentages for all bootstraps.

In the following chapter, we explore the magnetization timing of the studied datasets.

5.1.1 Jurassic Primary Magnetization

From the reviewed data sets, the Villa Juárez locality exhibits traits characteristic of a primary magnetization. Sample collection in this locality, as reported by Rodíguez-Parra (2020) was conducted by sampling an individual lava flow per site. In comparison to intrusive rocks, lava flows cool very quickly due to extrusion. This drives lava flows to capture snapshots of the geomagnetic field. The majority of the sampling sites from Villa Juárez show high concentration parameters ($k > 100$) that resemble a spot-reading of the geomagnetic field (Deenen et al., 2011; Gerritsen et al., 2022; Figure 4.16 and Table 4.6). It is arguable that some remagnetization processes could produce high concentration parameters like the ones seen in this locality (e.g., Pastor-Galán et al., 2021). However, If this was the case the remagnetization would affect all lava flows as a whole at the same time in a rather small area such as the one sampled in Villa Juárez. The average paleomagnetic direction

obtained from each individual lava flow in this locality differs noticeably (Figure 4.16). At the same time, despite the strong consistency within each lava flow, site averages do not group around VGP in a way close to resembling the GAD's PSV. Certainly this peculiar result may be the consequence of a primary magnetization acquired during this lava flow's initial extrusion , (193.3 ± 1.5 (U-Pb LA-ICP-MS in zircon; Barboza-Gudiño et al., 2021; Busby & Centeno-García, 2022 and references therein) that coincides with a time period when the earth's magnetic field was unstable and reversed and excursed frequently (e.g., Ogg, 2020). According to Deenen et al. (2011) and Gerritsen et al. (2022) multiple spot-readings of the geomagnetic field over a "sufficient" period of time are required to average out paleosecular variation (PSV). Unfortunately, the data acquired from this locality did not include a large enough number of sampled lava flows to "average out" such a highly variable paleosecular variation. For these reasons the Villa Juárez locality does not meet the contemporary reliability criteria (e.g., Gerritsen et al., 2022; Meert et al., 2020). Magnetite and hematite were identified as the magnetic carriers in this locality (Figure 4.13 A, B and C). SEM images (Figure 4.15 A and B) show well-formed euhedral to subhedral crystals of magnetite and hematite with no signs of alteration, weathering, neo-forming minerals, nor apparent penetrative deformation, which supports the premise of a primary magnetization for the Villa Juárez locality. The age of the magnetization in this locality is interpreted as Early Jurassic (195 ± 7 Ma) corresponding with the lava cooling age (Barboza-Gudiño et al., 2021). This locality was not considered in the final calculations.

5.1.2 Late Jurassic Remagnetizations

A Fold test (Tauxe & Watson, 1994) was performed in one of the sampled areas in the San Julian Uplift (MSM). The results show that this area´s

directions group in the Geographic coordinate system with a maximum Tau between 1 and 31% unfolding and disperse at tilt correction (Figure 5.1). This suggests that the “W” component from the MSM is the product of a remagnetization after folding. In this locality, the similarity of the “W” component between all three areas in geographic coordinates and the observed absence of geomagnetic field reversals recorded in the samples (Figure 4.6) support the proposition that the other two sampled areas in the San Julian Uplift (Caopas and Nazas N) were also (re)magnetized at the same time as the MSM area. Likewise, the inclination of all three areas in this locality show shallow inclinations (Figure 4.6 and Table 4.7) that match with the expected inclinations for Mexico during the Jurassic (Vaes et al., 2023). In the same manner, SEM imagery shows the presence of neo-forming hematite that fills fractures in other crystals, attesting to the secondary nature of this hematite, as well as weathering rims composed of hematite and magnetite minerals (Figure 4.4 A and B). Rock magnetic properties of the samples in all three areas of the San Julian Uplift exhibit the presence of hematite and magnetite (Figures 4.1 and 4.2 and Annexes, 4.2 and 4.3).

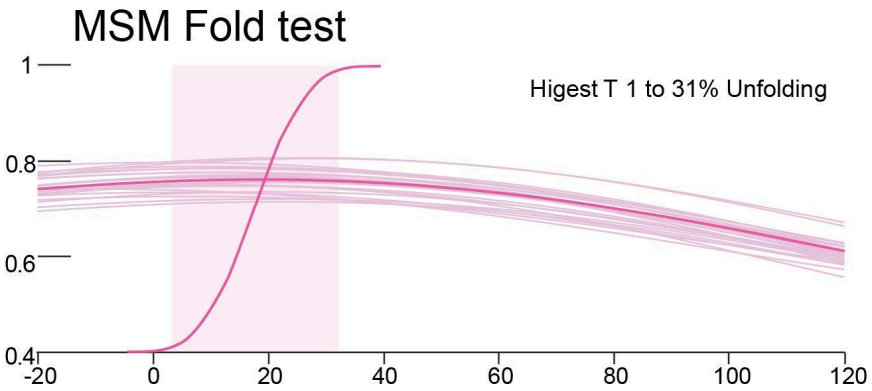

Figure 5.1 – Foldtest result. The unfolded data is represented by the bold curve and the first 25 bootstraps by light lines. The maximum eigenvalue at a particular unfolding percentage is recorded and shown with 95% confidence limits for 1000 bootstraps (Tauxe & Watson, 1994) The results from the MSM locality show a maximum Tau between 1 and 31% unfolding. The negative fold test signifies that the W component in MSM is the product of a remagnetization after folding.

As revealed by the fold test, SEM images and rock magnetic properties, magnetization in this locality is post-folding. However, folding in the Mina de San Miguel area is unknown. Previously, studies have interpreted the MSM anticline as a result of the thick-skinned tectonic event in this area . Pursuant to this interpretation, the anticline would have formed as a drag structure product of the fault that exhumed the San Julián Uplift during the Eocene (Guerra Roel, 2019; Patiño-Mendez, 2022; Ramírez-Peña & Chávez-Cabello, 2017). However, inclinations observed in the directions of the MSM area in geographic coordinates are not concordant with a post-Eocene remagnetization (Figure 5.2). One possibility that could explain the shallow inclinations is a rapid post-Eocene remagnetization that yielded a biased shallow inclination due to insufficient PSV averaging. However, this hypothesis is weak since the VGP shape and k parameters are compatible with correct averaging of the PSV. This data aligns better with a Late Jurassic remagnetization driven by the emplacement of igneous rocks (Anderson et

al., 1991; Guerra Roel, 2019; Jones et al., 1995; Ramírez-Peña, 2017; Ramírez-Peña & Chávez-Cabello, 2017).

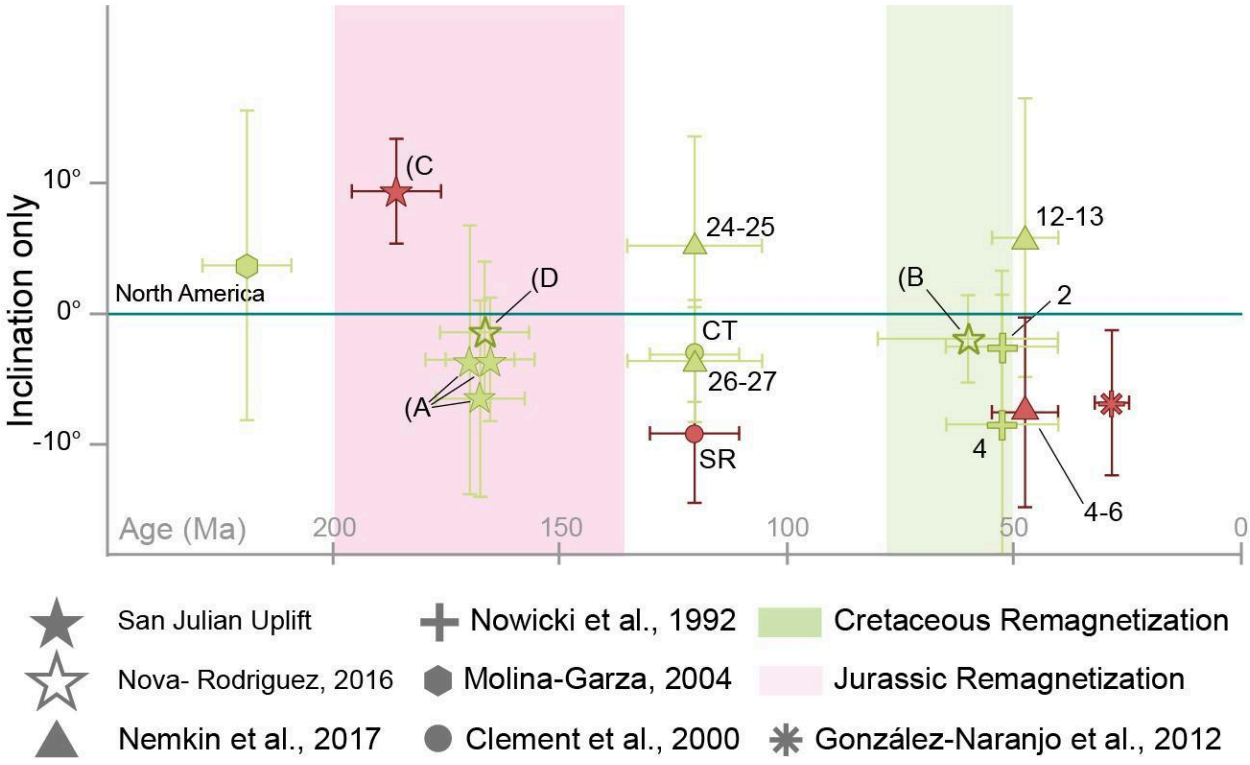

Figure 5.2 Observed inclinations from sampled and compiled localities compared to Global Apparent Wander Path of the study area for North America (Vaes et al., 2023). All localities are represented in geographic coordinates. (A) San Julián Uplift (MSM, Caopas, and Nazas North), (B) Real de Catorce, (C) Charcas, (D) Huizachal Valley. Red/Green colored directions are not/ concordant with stable North America. Showing probable remagnetization windows.

The hypothesis of a Late Jurassic remagnetization is weakened by the fact that no previous studies have suggested a Late Jurassic origin for the MSM anticline. Despite that, the emplacement of other minor bodies associated with a Late Jurassic magmatic pulse at the Huizachal Valley (Figure 2.1) has been attributed causing angular unconformities between sub-members of La Boca and in the contact between La Boca and La Joya

Fms. (Fastovsky et al., 2005; García-Obregón, 2008; Rubio Cisneros, 2012; Rubio Cisneros et al., 2011). I support the idea that the emplacement of the Caopas laccolith (165 Ma) generated enough deformation during emplacement to at minimum be responsible for part of the local antiformal structure in the MSM area around 165 Ma, in a similar manner to that described in Bunger & Cruden (2011) and Wilson et al. (2016). In addition to this, the ensuing cooling of the Caopas laccolith and the post-emplacement fluid circulation might be responsible for the remagnetization.

Additionally I think that the Huizachal locality was remagnetized during the Jurassic. The result of the fold test from this locality is inconclusive (Figure 5.3), and the data from this locality does not account for any other field test to establish a relative timing for the magnetization. However, the data does not show reversals, whose time of formation accounts for over 18 million years of the Jurassic (184 – 166 Ma). A remagnetization in this locality can better explain this result, as the geomagnetic field during that time in the Jurassic was highly variable (Ogg, 2020). Furthermore, this locality shows inclinations (Figure 4.12), similar to the other Jurassic samples reinforcing the idea of a Late Jurassic remagnetization, no younger than 140 Ma, as the results from the San Julian Uplift locality. The data from this locality was used with caution.

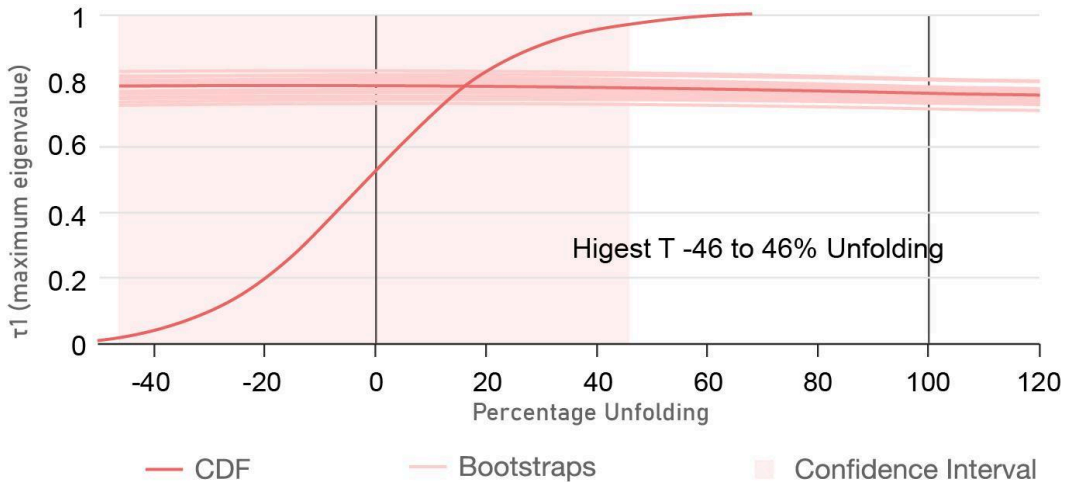

Figure 5.3 Huizachal Fold test results. Does not display a conclusive percentage of best fit of unfolding.

The data from the Charcas locality shows eight sites (CHA3 to CHA10) with a good directional consistency with a "k" of 53 at specimen level and a "k" of 87 when considering the average of the site means. These results indicate that the samples from CHA3 to CHA10 sites correspond to a single cooling unit or all sites were remagnetized at the same time (Figure 4.11 and Table 4.4). Samples from sites CHA-1 and CHA-2 yielded very different averages (Figure 4.11 and Table 4.4). This inconsistency can be explained by two scenarios: 1) an extreme paleosecular variation event at the time of magnetic acquisition (either primarily or during a remagnetization), or 2) by several different magnetization events. Unfortunately, this dataset does not support any of these or alternative hypotheses.

5.1.3 Cretaceous Remagnetizations

The data compiled from the Real de Catorce locality results in a negative fold test (Figure 5.4). Folding in Real de Catorce has been dated between 91 and 60 Ma (Ar-Ar in illite, Gutiérrez-Navarro et al., 2021). Whereas the San Julián Uplift matches Jurassic expected inclinations, Real de Catorce's

inclinations resemble those expected for Cretaceous and younger rocks (< 140 Ma; Vaes et al., 2023; Figure 5.2). The presence of double polarity in this locality (Figure 5.4) is indicative that the samples did not remagnetize, or at least not completely, during the Cretaceous Superchron that lasted ~43 ma from ~126 ma to ~83 Ma (Ogg, 2020). Defining a relative age of remagnetization in this locality is challenging but considering the post-folding nature and the post-superchron character of the magnetization, Paleocene to Early Eocene is the most fitting time for a remagnetization to have taken place.

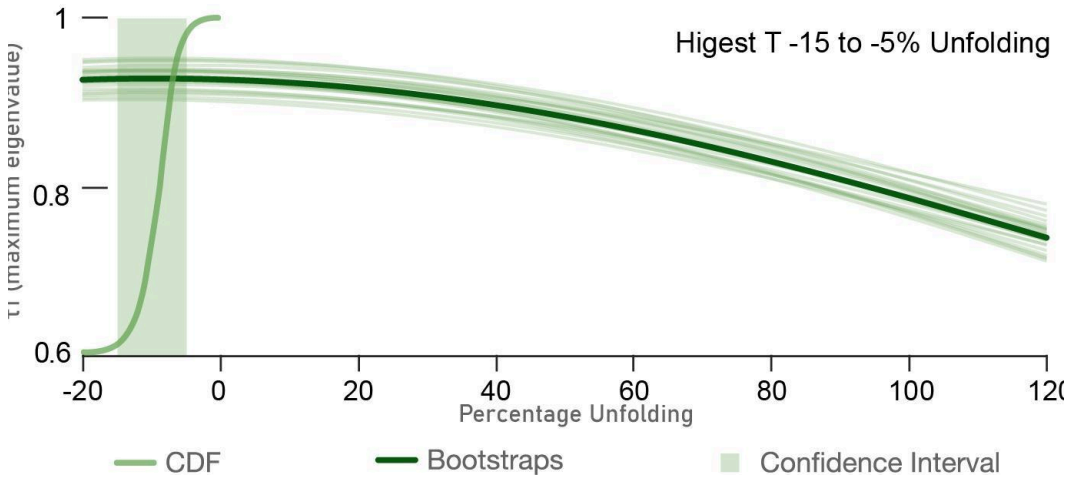

Figure 5.4 Negative Fold Test (Tauxe & Watson, 1994) for the Real de Catorce locality. Note that maximum grouping is between -15% to -5% indicating a Post-Folding Magnetization.

5.1.4 Taraises Formation Magnetizations

From the sampled localities across the northeastern curvature of the Sierra Madre Oriental I conducted 25 fold-tests (Tauxe and Watson, 1994) to establish the relative age of remanence with respect to the anticline structures. The results indicate the presence of pre-folding, syn-folding, and post-folding magnetizations in different parts of the SMO (Table 5.1). The majority of the fold tests yielded conclusive results as shown in Figure 5.5, 5.6

and 5.7. Only four anticlines showed anomalous results. The MTH anticline yielded an inconclusive fold-test, due to the fact that the declinations of each limb did not concentrate at any point during unfolding (from -150% to +150% correction), for this reason this anticline was not considered for further analysis. The other three anomalous fold-tests produced two tau maxima at both geographic and tilt-corrected coordinates (LH, MDG, and SJR3-4). In the cases of MDG and SJR3-4, the fold test generated an artificial tau maximum in geographic coordinates, where directions are close to antipodal. However, these directions are in the same hemisphere, not opposite, and the inclinations in geographic coordinates are too shallow (around ~0°) to represent a post-folding magnetization (Late Cretaceous or younger) when Mexico was at a similar latitude to today (Vaes et al., 2023).

The case of LH is the opposite: after tilt correction, two close-to-antipodal but same-hemisphere shallow inclinations produce a high Tau. However, in geographic coordinates, it fits well with a Cretaceous inclination. If we consider the paleomagnetic directions coordinates minimizing the dispersion best fit of each fold-test (i.e. geographic, tilt corrected, or a given percentage of unfolding), all localities present single polarity, down directed inclinations, and W to NE declinations with the exception of the NSJ anticline, which shows two polarities (Table 5.1).

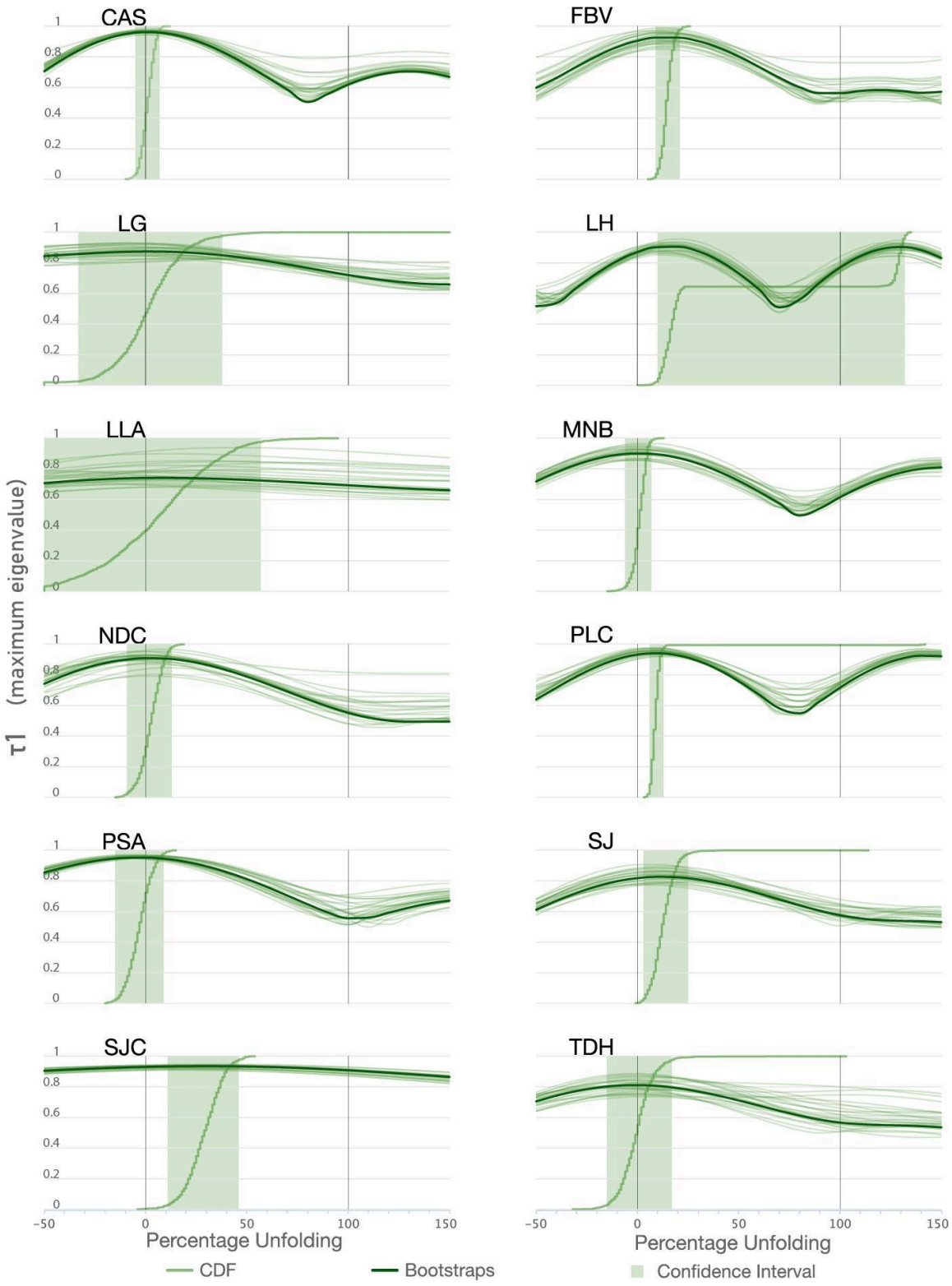

Figure 5.5 Fold tests (Tauxe & Watson, 1994) results showing pre-folding magnetizations. Note all grouping is close to 0% unfolding. For mean directions at % of highest Tau see Table 5.1.

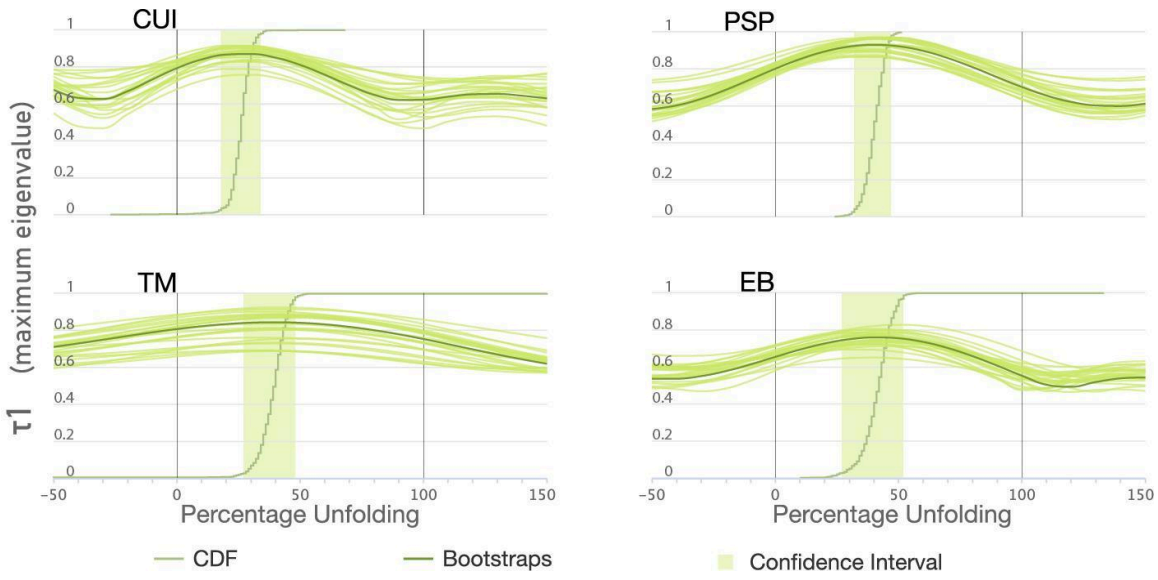

Figure 5.6 Fold tests (Tauxe & Watson, 1994) results showing syn-folding magnetizations. Note all grouping is close to 50% unfolding. For mean directions at % of highest Tau see Table 5.1.

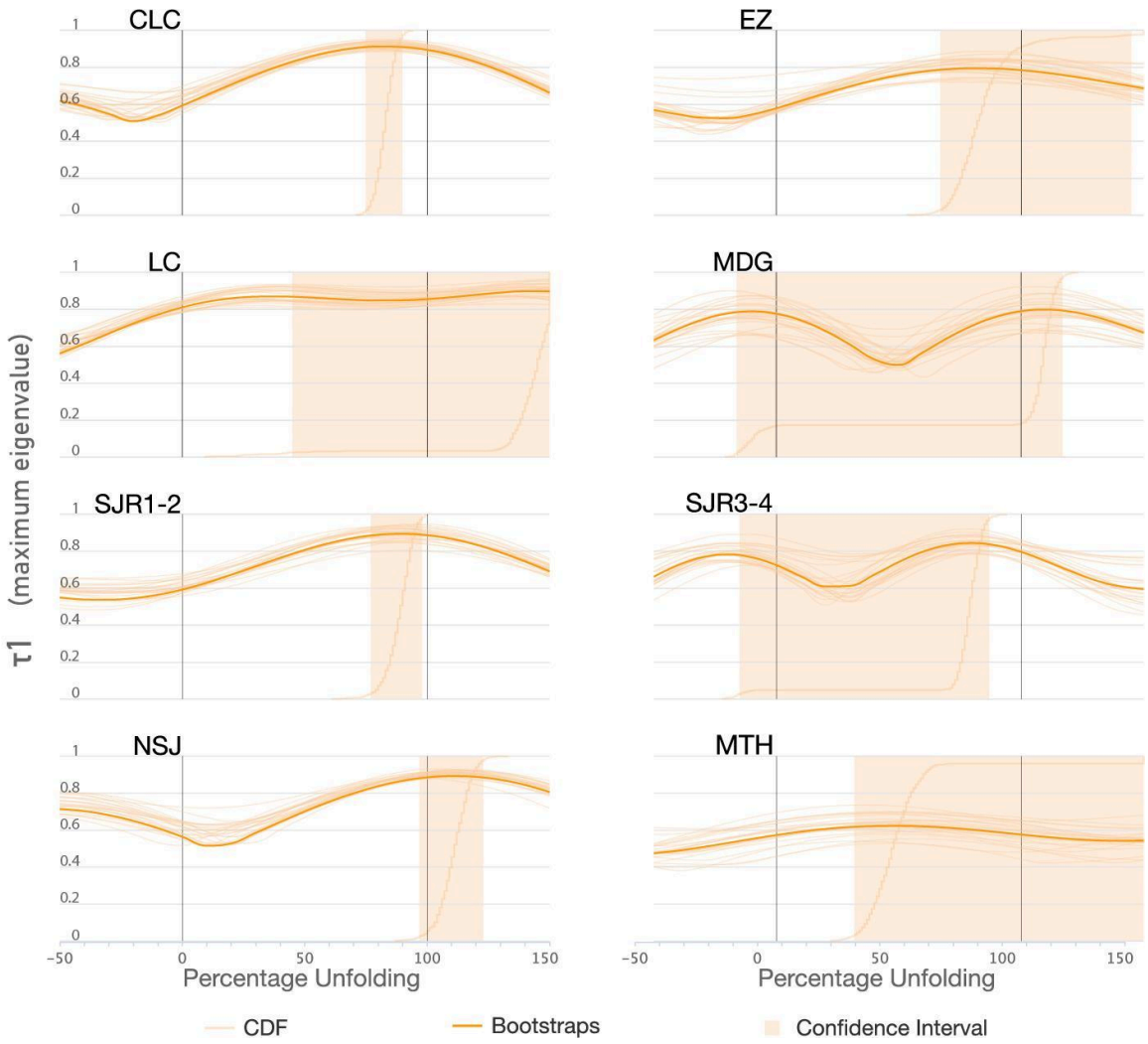

Figure 5.7 Fold tests (Tauxe & Watson, 1994) results showing Post-Folding Magnetizations. Note all results show a high Tau close to 100% unfolding. For mean directions at % of highest Tau see Table 5.1.

The average inclination was calculated for the pre-folding localities and the syn- and post-folding ones with inclination only statistics (Aarason and Levy, 2010). The results show an average inclination of all pre-folding inclinations of 44.6° ± 5° and a slightly higher 46.4° ± 2° for the syn- and post-folding ones (Figure 5.8).

Table 5.1 Taraises Fold Test mean directions.

Collection	Foldtest	Range (%)		Dec	ΔDx	Strike	Coordinates	
							Lat.	Long.
CAS	Negative	-5.00	7	295.26	8.15	255	24.6	-101.7
FBV	Negative	9.00	21	297.48	5.5	317	24.5	-101.4
LG	Negative	-40.00	36	35.56	5.57	8	24.4	-101.4
LH	Negative (1)	10.00	130	308.21	24.29	319	25.0	-100.9
LLA	Negative	-50.00	50	336.16	16.85	325	24.6	-100.3
MNB	Negative	-6.00	7	272.97	7.92	274	24.7	-101.7
NDC	Negative	-9.00	13	0.16	8.51	345	24.2	-100.7
PLC	Negative	6.00	13	292.96	5.75	239	24.5	-101.8
PSA	Negative	-15.00	9	2.42	6.16	336	24.1	-100.8
SJ	Negative	3.00	25	288.14	8.03	265	25.0	-101.5
SJC	Negative (2)	11.00	46	305.07	5.31	320	24.4	-101.5
TDH	Negative	-15.00	17	312.27	8.19	269	24.5	-101.6
CUI	Negative (Syn-30%)	19.00	34	328.32	6.97	284	24.5	-101.6
PSP	Negative (Syn-40%)	32.00	47	281.34	4.87	273	25.0	-101.2
TM	Negative (Syn-40%)	27.00	48	9.61	8.87	10	23.4	-100.3
EB	Negative(Syn-40%)	27.00	51	335.94	7.42	340	24.6	-100.6
CLC	Positive	75.00	90	302.86	6.51	282	25.2	-101.4
EZ	Positive	67.00	144	27.02	7.1	25	24.1	-100.5
LC	Positive (3)	39.00	150	329.55	7.09	318	24.7	-100.7
MDG	Positive (4)	-16.00	117	330.06	10.75	356	24.3	-100.3
SJR1-2	Positive	77.00	98	6.92	7.85	343	24.6	-100.2
SJR3-4	Positive	-15.00	87	8.11	12.51	350	24.5	-100.2
NSJ*	Positive	97.00	123	356.21	7.57	281	25.1	-102.2

ΔDx uncertinty in Declination, (1) Foltest generates artificially two peaks because the directions get closer to antipodal, but with the same inclination not opposite. (2) Foldtest looks non-conclusive but k is better in Geo. (3) k and K concentrate better in TC. (4) Foldtest generates artificially two peaks because the directions in geo are near to antipodal but with the same inclination not opposite. (*) It is the only site that does not follow the pattern and we consider it an outlier

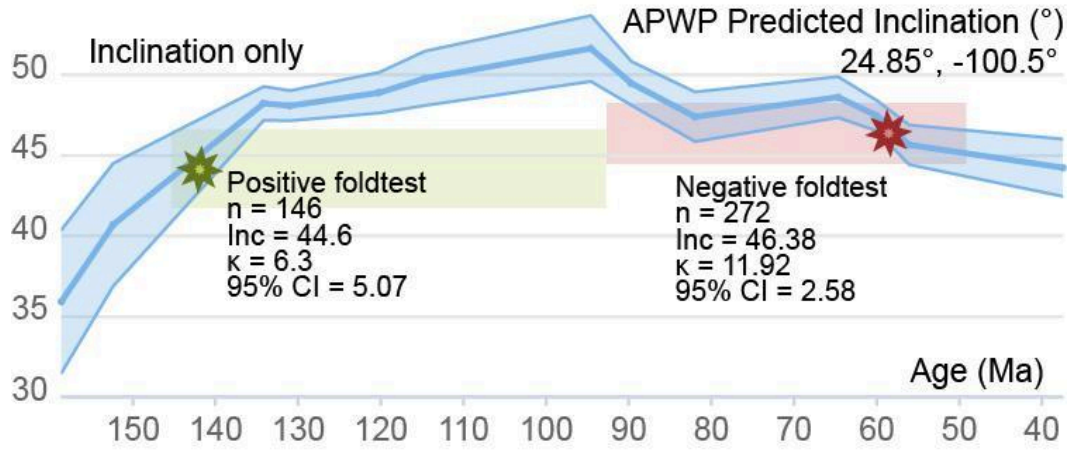

Figure 5.8 GAPWaP (Vaes et al., 2023) showing average inclination of pre-folding localities and the syn- and post-folding with inclination-only statistics (Aarason and Levy, 2010). The results show the average inclination of all pre-folding inclinations 44.6° ± 5° and 46.4° ± 2° for syn- and post-folding.

When compared with the GAPWaP (Vaes et al., 2023) those inclinations are consistent with a primary magnetization of 145 to 130 Ma for the pre-folding cases and 90 Ma to 55 Ma for the syn- and post-folding. The paleomagnetic analysis indicate three groups of anticlines based on the timing of their magnetization: (1) pre-folding, with likely primary magnetization acquired around 140 Ma (Figure 5.5); (2) syn-folding, with magnetization acquired after 90 Ma (Figure 5.6); and (3) post-folding, with magnetization younger than approximately 70 Ma (Figure 5.7). Additionally, joint sets develop very early in the deformation process (e.g., Engelder & Geiser, 1980), so we can consider the joint set data as faithfully representing conditions around 90 Ma (Figure 5.10) time when initial deformation is dated (Fitz-Diaz et al., 2018).

In summary and by chronological order the data shows:

1. A primary magnetization of the Triassic Acatita intrusives (Molina Garza, 2004).
2. A secondary magnetization product of a Late Jurassic remagnetization that affected the localities of the San Julian Uplift, Charcas, and Huizachal Valley.
3. Primary magnetizations of the pre-folding Taraises samples (145-130 Ma) and the CT locality of Clement et al., (2000).
4. NRM product of a remagnetization dated at 90 - 50 Ma that is present in Real de Catorce locality also present in the syn-folding results.
5. Post folding results of the Taraises Fm. younger than approximately 70 Ma.
6. Finally, the remaining data show magnetizations post 50 Ma. Localities 2 and 4 from Nowicki et al. (1992), foldtests 4-6 and 12-13 from Nemkin et al. (2019). As well as the ignimbrites from González-Naranjo et al. (2012).

5.2 Vertical axis rotations:

To quantify the potential vertical axis rotations it is standard practice to compare the observed declination from each locality with their expected declination according to Vaes et al. (2023) CAPWaP for stable North America for the inferred time of magnetization acquisition. The results of this section will be listed in chronological order.

The rocks that (re)magnetized before 120 Ma show significant rotations except ones from Molina-Garza's (2004) data. The Data retrieved from the study seem to be collected in an area that was not affected by the Mexican Fold and Thrust Belt's deformation for its part of the older litologies of the Coahuila Block (Figure 2.2). This data shows no apparent rotations when compared with the Vaes et al. (2023) CAPWaP for stable North America (Figure 5.9).

The San Julian Uplift, as well as, the critically reviewed datasets of (Clement et al., 2000; Nemkin et al., 2019; Nova-Rodríguez, 2016) revealed significant counterclockwise rotations of up to 75° in the northern limb of the Sierra Madre Oriental and up to 30° clockwise rotations in the southern limb. These rotations are illustrated in Figure 5.9 (also listed in Table 4.7).

From the results of the Taraises Fm. after the structural correction that allows for the best concentration of the paleomagnetic directions specified in Figures 5.5, 5.6, and 5.7 the declinations of the localities notably vary from ~W to ~NE (Figure 5.10; Table 5.1). This is consistent with vertical axis rotations due to orocline bending/buckling. Only NSJ1 and NSJ2 do not follow this curved trend. Inclinations are always downwards with one exception (NSJ1; Table 5.1). The anticline NSJ represents an outlier both in declination behavior with respect to the orogen strike and in its dual-polarity ChRM (Figure 5.11).

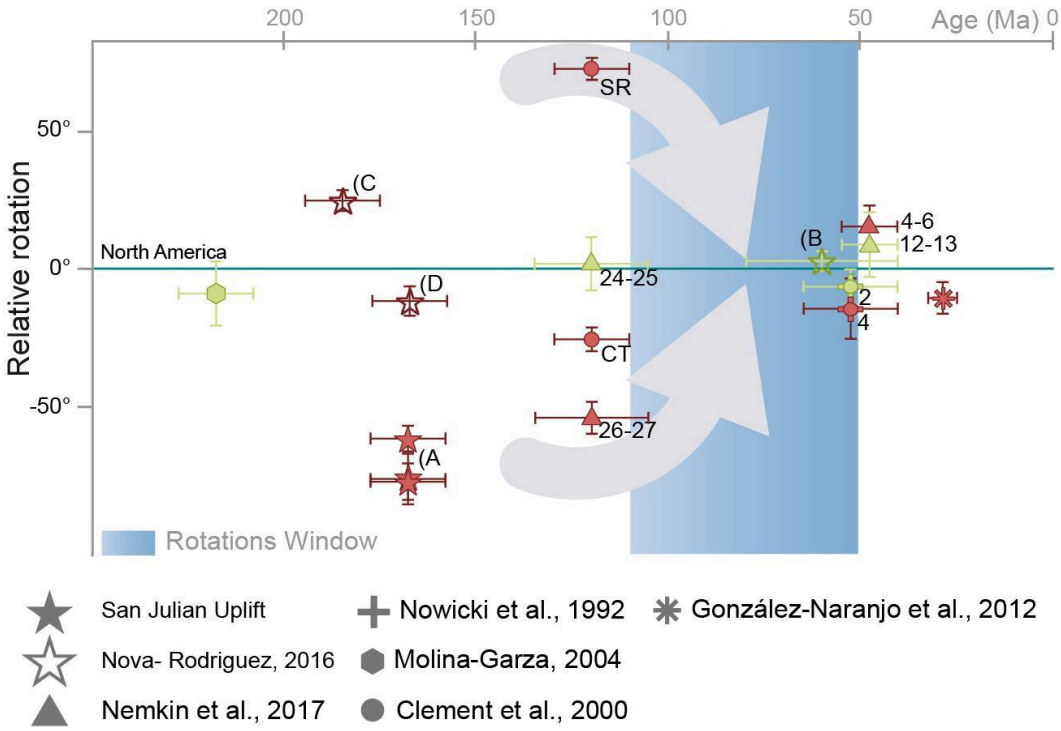

Figure 5.9 Relative rotations of previous studies and the San Julian Uplift in geographic coordinates compared to Global Apparent Wander Path of the study area for North America (Vaes et al., 2023). (A) San Julián Uplift (MSM, Caopas, and Nazas North), (B) Real de Catorce, (C) Charcas, (D) Huizachal Valley. Red/Green colored directions are not/ concordant with stable North America.

The field data of limb 2 of the NSJ locality shows the expected rotation in geographic coordinates if all NSJ declinations follow the same pattern as the rest. However, NSJ1 shows a direction not found in any of the studied sites, regardless of the strike orientation. NSJ1 is one of the few localities where a second component was identified (mid-temperature and mid-coercivity). It is reasonable to believe that the NSJ1 ChRM component might not have been properly resolved due to partial remagnetization, resulting in a mixture of both components.

The structural corrections for the samples of the Taraises Fm. are as follows: a) geographic coordinates for sites with a negative fold-test: CAS, FBV, LG, LH, LLA, MNB, NDC,PLC, PSA, SJ, SJC, and TDH. The tilt corrected (Tectonic coordinates) declination in the cases of a positive fold-test CLC, EZ, LC, MDG, SJR1-2, and SJR3-4; and the declination corresponding to the tightest grouping in the case of syn-folding remagnetizations CUI, PSP, TM, and EB. Figure 5.11 illustrates the directions in equal area projections.

Regardless of the time of magnetization the observed declinations from the Jurassic and the Cretaceous (165 - 70 Ma) seem to follow the trend of the Sierra Madre Oriental with NSJ (perpendicular to the trend) as the only exception (Figure 5.10; Table 5.1). I hypothesize that the curvature of the Sierra Madre Oriental (Figures 2.1 and 5.10) is an orocline "*sensu*" Sussman & Weil, (2004) and Pastor-Galán et al. (2017).

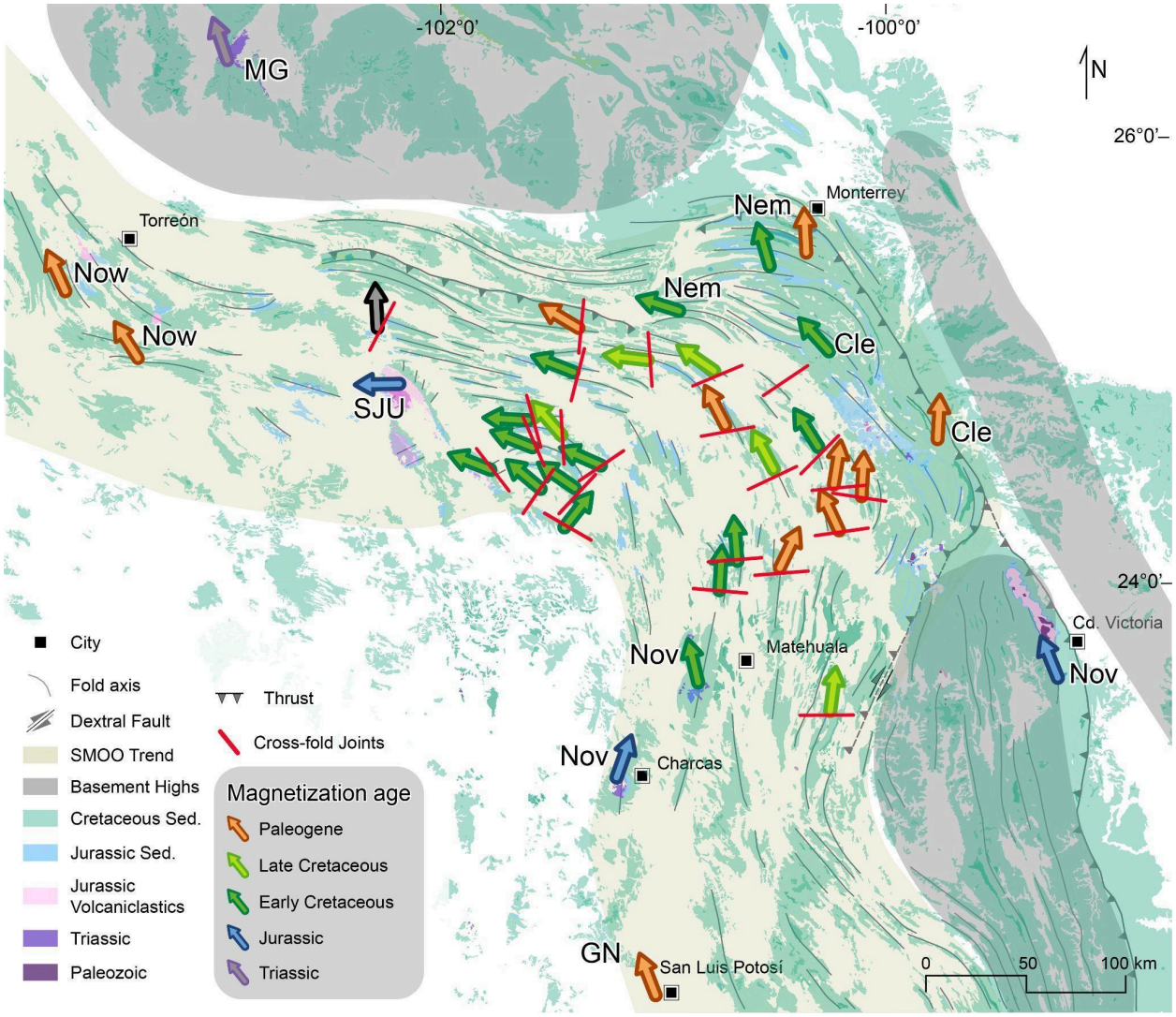

Figure 5.10 Schematic geo-structural map of the study area showing directional data and cross joints across the Sierra Madre Oriental. Joint and directional Jurassic and Cretaceous data follow the trend of the SMO Orocline. Note how the trend of the SMO Orocline follows the perimeter of the basement highs. SJU: San Julian Uplift, Now: Nowicki et al. (1993); Cle: Clement et al. (2000, Nem: Nemikin et al. (2019); Nov: Noval-Rodriguez (2016); GN: Gonzalez-Naranjo (2012). Gray arrow is NSJ. Directions are graphically represented in equal area projections in Figure 5.11.

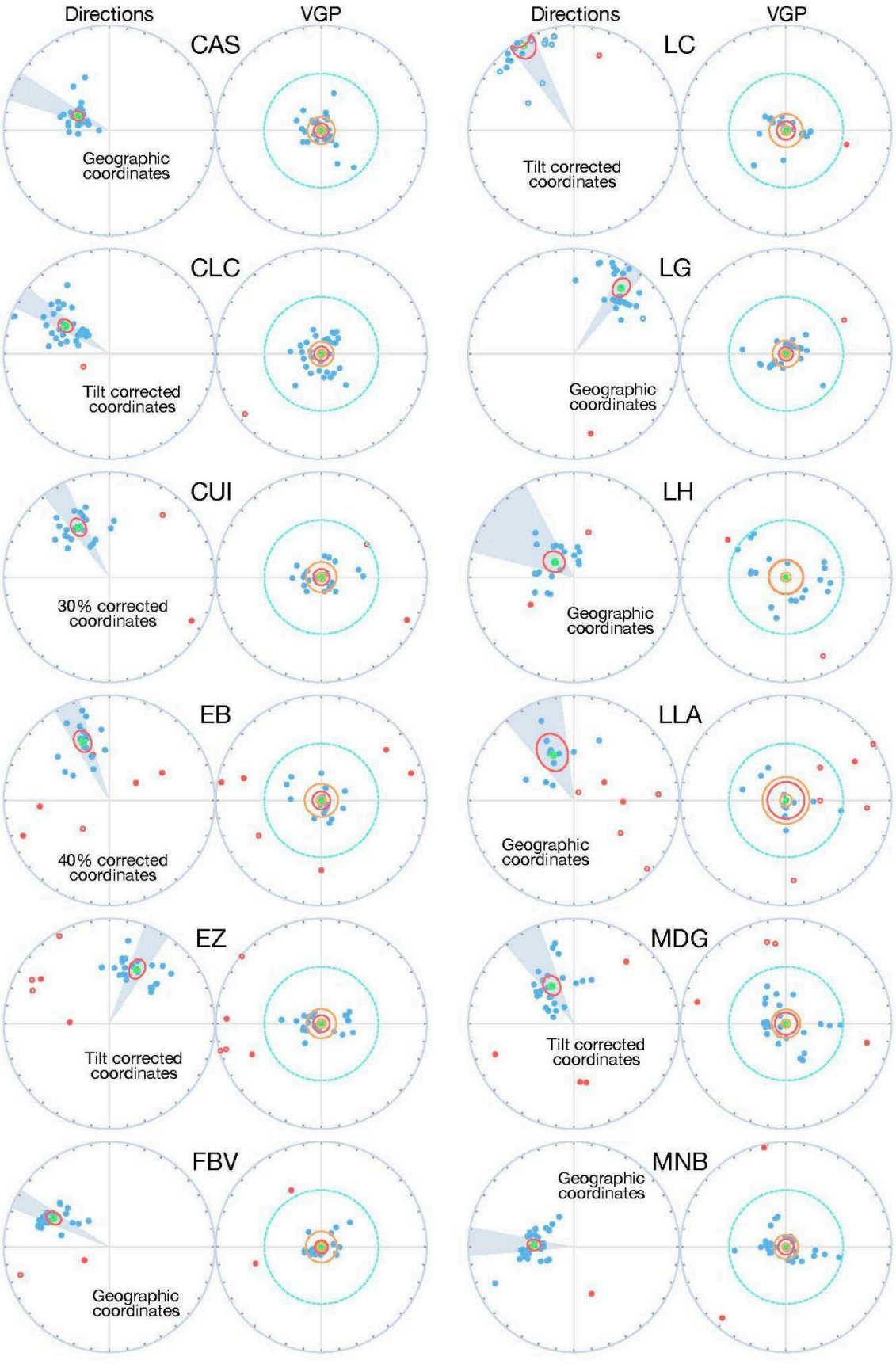
Directions
VGP
CAS
Geographic coordinates
LC
Tilt corrected coordinates
CLC
Tilt corrected coordinates
LG
Geographic coordinates
CUI
30% corrected coordinates
LH
Geographic coordinates
EB
40% corrected coordinates
LLA
Geographic coordinates
EZ
Tilt corrected coordinates
MDG
Tilt corrected coordinates
FBV
Geographic coordinates
MNB
Geographic coordinates

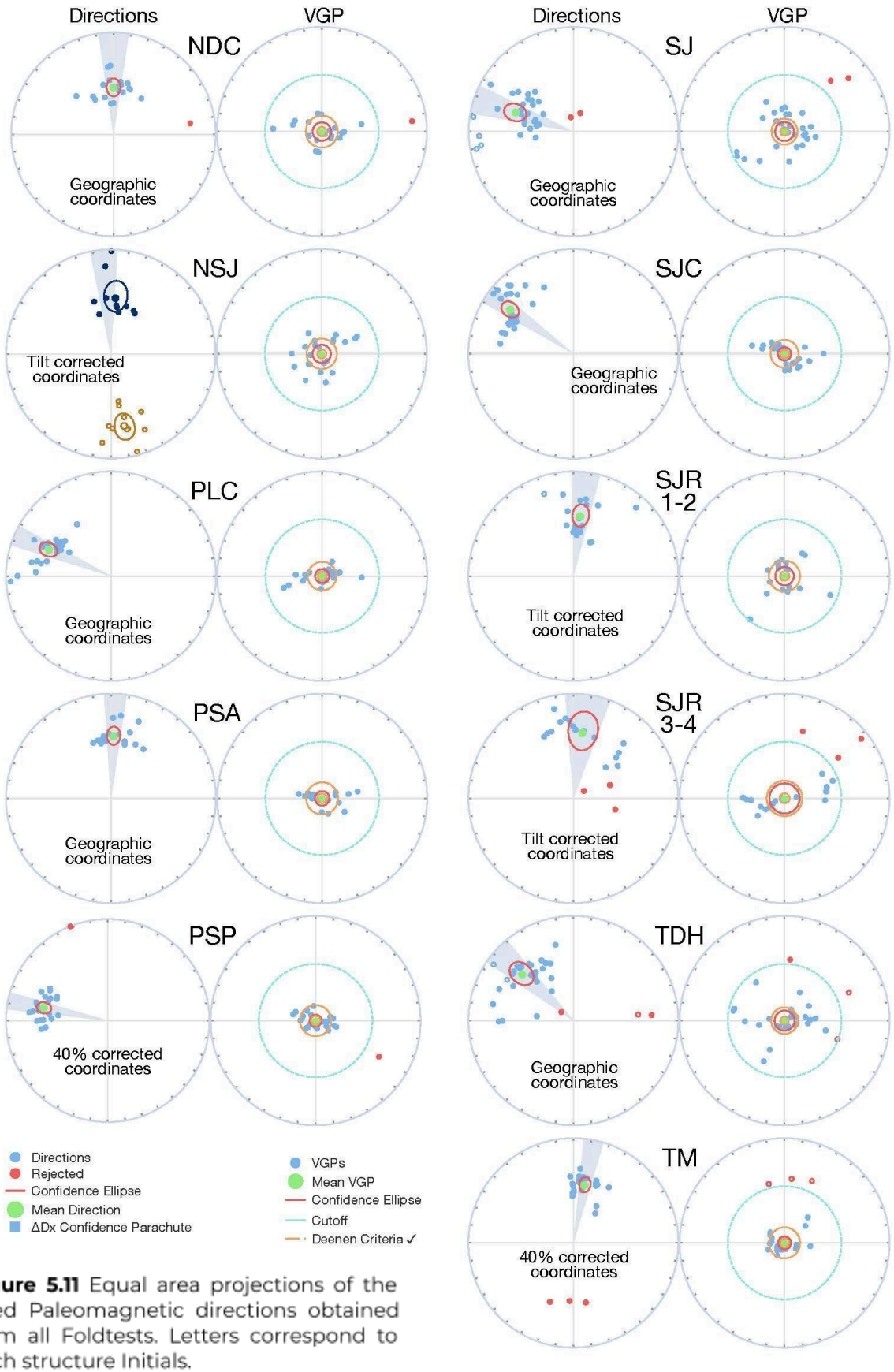

Figure 5.11 Equal area projections of the used Paleomagnetic directions obtained from all Foldtests. Letters correspond to each structure Initials.

5.3 The Twisted Kinematics of the Sierra Madre Oriental

The orocline test is an effective tool for studying the kinematics of curved mountain belts (e.g., Meijers et al., 2015; Yonkee & Weil, 2010). With the temporal framework described in the previous section, we can consider several scenarios for the formation of the curvature:

a) **A Primary feature:** If the curvature is a primary feature, such as an inherited physiographic shape like an embayment, the slope would be ~0 in all orocline tests (Pastor-Galán et al., 2011, 2017; Sussman & Weil, 2004; Yonkee & Weil, 2010).

b) **A Progressive orocline:** If the Sierra Madre Oriental (thin-skinned) bent concomitantly with the 'Sevier' event, orocline tests should show progressively decreasing slopes, starting at close to 1 for the pre-folding and joint sets and ending around 0 for the post-folding localities.

c) **A Secondary orocline:** If all orocline test results are similar, it would indicate a vertical axis rotation after the formation of the thin-skinned fold-and-thrust belt. If that slope were less than one, the difference would represent a percentage of primary curvature.

The Bootstrapped Total Least Squares Orocline Test (Pastor-Galán et al., 2017) was used to evaluate the curvature of the Sierra Madre Oriental Orocline with respect to paleomagnetic declinations and strike-perpendicular joint sets. This method incorporates measurement uncertainty in paleomagnetic analyses (ΔDec) and an estimated uncertainty for joint analysis layer parallel shortening directions (typically ± 10° (Pastor-Galán et al., 2011)). The anticlines' structural trend was estimated from the fold axis trend and local bedding strike, with a typical uncertainty of 10°. At least 25 localities are required to

perform an accurate orocline test in a 110° curvature as the Sierra Madre Oriental Orocline (Pastor-Galán et al., 2017). However, seven different tests were performed on various subsets of the data to evaluate potential differences in vertical axis rotation depending on the magnetization timings. Some of the tests have as little as 4 localities, so their confidence interval might be too large to be considered quantitative. These tests are as follows: (a) four tests considering paleomagnetic declinations separately based on their magnetization timing relative to folding (two pre-folding tests one including NSJ and other without it, one syn-folding test, and one post-folding test); (b) one test considering all declinations together (Figure 5.12); (c) one test considering all declinations together, including those critically reviewed previous studies; and (d) one test comparing the strike of the orogen with the cross-fold joint set (Figure 5.13). The slope results of the tests (summarized in Table 5.2) range from 0.59 (pre-folding including NSJ) to 1.01 (cross-fold joints). The confidence intervals for all orocline tests overlap except for the pre-folding test with NSJ, where the outlier critically affects the result (0.59 with NSJ, 0.84 without it).

Overall the results show that all but one of the orocline tests (Table 5.2) support a nearly 1:1 correlation between the strike and the studied fabrics (paleomagnetic declinations and cross-fold joint sets). Ironically, the exception is the pre-folding magnetization (~140 Ma), which shows the smallest slope (m = 0.59). This result indicates that 60% of the rotation occurred from 140 Ma onwards. In contrast, post-folding magnetizations yield a slope of 0.89, suggesting that ~90% of the orocline formation happened after 70 Ma. This apparent contradiction disappears when we discard the outlying declination of the NSJ anticline from the orocline test (see section 5.2). Once removed, the slopes of the pre-folding (0.84 ± 0.18), joint sets (1.01 ± 0.09), syn-folding (0.77 ± 0.19), and post-folding (0.89 ± 0.06) orocline tests are within confidence

intervals (Table 5.2). The small differences can be attributed to the limited number of data points (~25) for the 110° curvature in the Sierra Madre Oriental (see Pastor-Galán et al., 2017).

Table 5.2 Orocline test results for diferent data subsets.

Orocline tests	n	Total Least Squares	Average Bootstrap	Confidence Interval
Prefolding (with NSJ)	7	0.59	0.59	0.44 - 0.76
Prefolding*	6	0.83	0.84	0.68 - 1.03
Synfolding*	4	0.77	0.77	0.61 - 0.96
Postfolding*	12	0.89	0.89	0.77 - 1.03
Cross-fold joints	25	1.01	1.01	0.92 - 1.10
All*	22	0.83	0.83	0.75 - 0.92
All and literature*	30	0.89	0.89	0.83 - 0.95

NSJ excluded from the analysis, n = number of localities

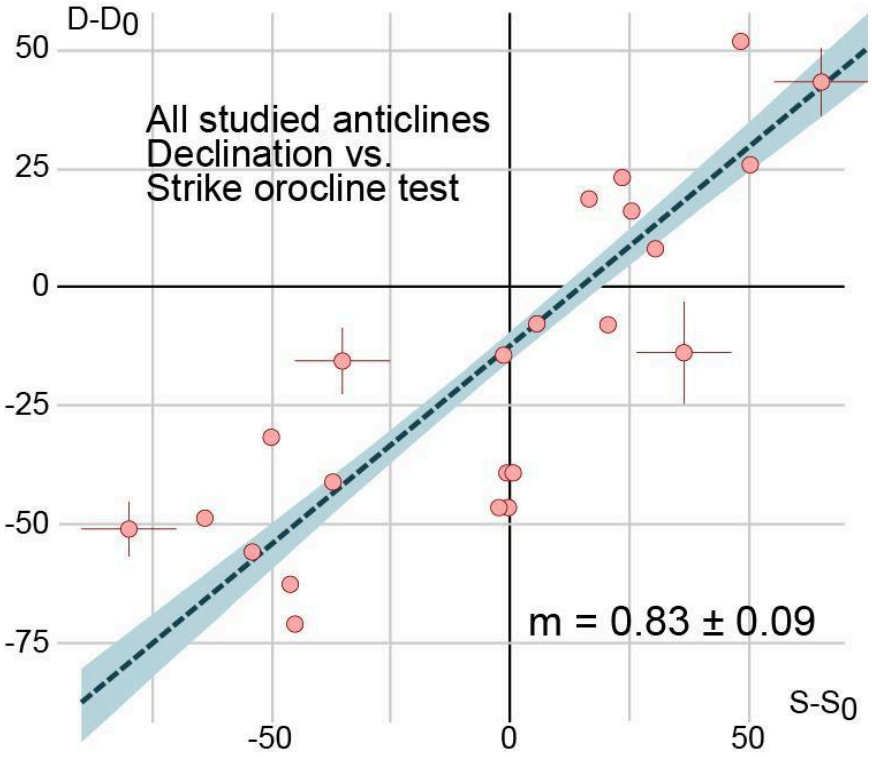

Figure 5.12 Bootstrapped Total Least Squares Orocline Test (Pastor-Galán et al., 2017) Orocline test of all studied structures D-Do = Declination; S-So = Strike.

Due to the similarities between the individual strike vs. declination orocline tests, we can confidently perform a test with all paleomagnetic data but NSJ from this study (n = 22). Combining all results allows us to get a more accurate and precise orocline formation kinematics estimation from paleomagnetism (Figure 5.12; Table 5.2; Pastor-Galán et al., 2017). This orocline test has a slope m = 0.83 ± 0.09 (Table 5.2). An orocline test with these anticlines and the compiled data yields m = 0.89 ± 0.06. These two orocline tests together with the joint sets (1.01 ± 0.09) establish that the Sierra Madre Oriental was originally a near-rectilinear fold-and-thrust belt that subsequently bent or buckled to form the Sierra Madre Oriental Orocline.

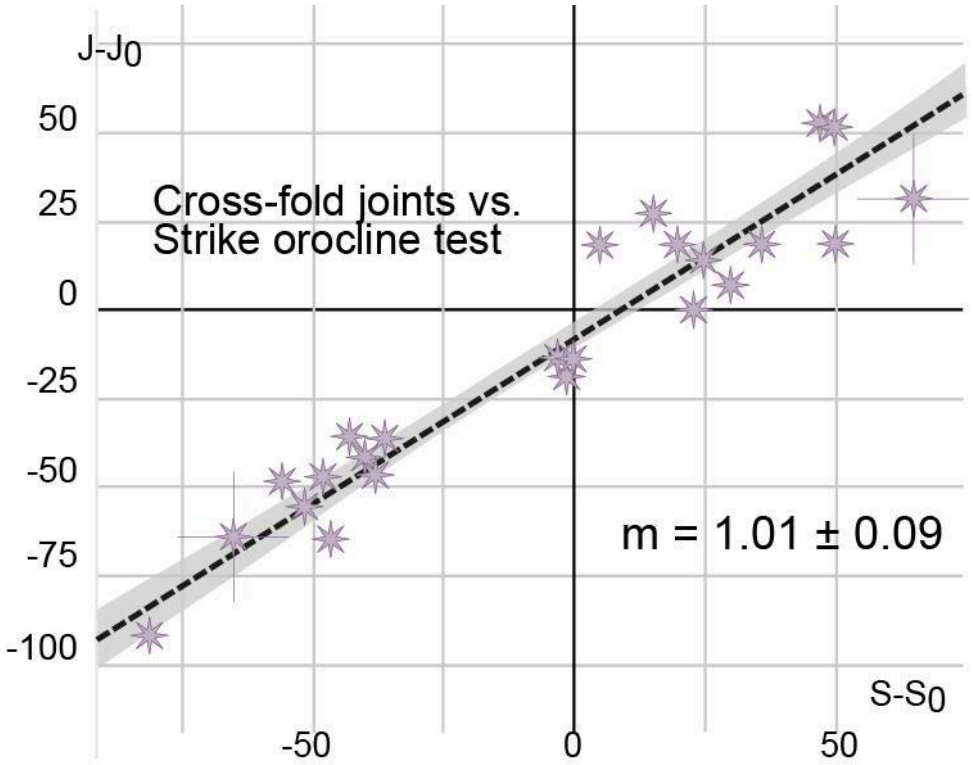

Figure 5.13 Bootstrapped Total Least Squares Orocline Test (Pastor-Galán et al., 2017) Cross-fold joint set vs. strike. J-Jo = Joint strike; S-So = Strike.

Chapter 6

The Sierra Madre Oriental Orocline: Tectonic Model & Conclusions

> "Scientists have become the bearers of the torch of discovery in our quest for knowledge."
>
> — **Stephen Hawking**

6.1 Tectonic Evolution of the Sierra Madre Oriental Orocline

The simplest kinematic scenario that integrates structural and geochronological data and explains our new observations is synthesized in Figure 6.1 and 6.2. During the Late Cretaceous the Mexican Fold and Thrust Belt was an approximately linear belt with a nearly N-S strike of its fold axes and E-W oriented cross-fold joints (Figure 6.1). During this time the Jurassic units had already undergone a remagnetization due to the Late Jurassic magmatism, and the Taraises Fm. was deposited acquiring a pseudo-primary DRM (>70 Ma; Figure 6.1 A). During and shortly after deformation, some parts of the Taraises Formation was remagnetized (~72 Ma Figure 6.1 B).

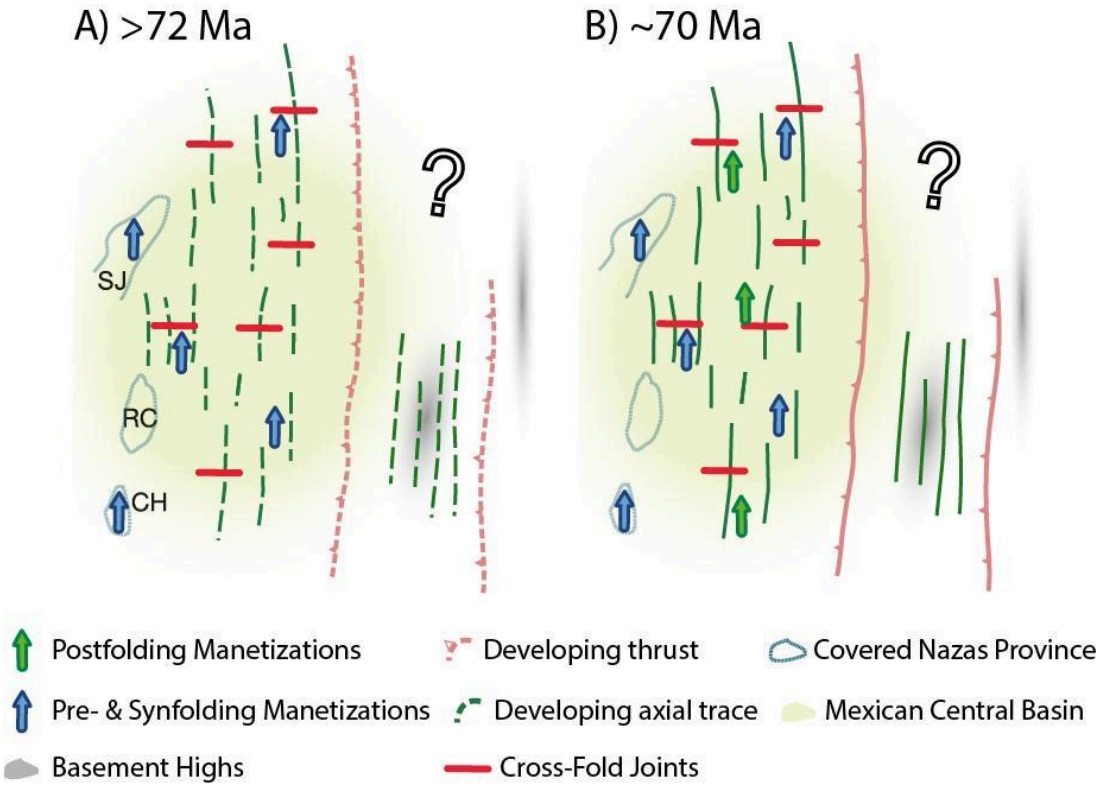

Figure 6.1 Tectonic evolution model for: A) 72 Ma mark during this time the Nazas Fm. and the Jurassic Red Beds were covered by sediments of the Mexican Central Basin. During this time the initial structures of the MFTB were developing. B) At 70 Ma the deformation stage of the oldest folds had matured and in some places remagnetization was taking place.

Sometime after the remagnetization the whole belt underwent vertical axis rotations. The northern limb of the orocline accommodated up to 90° of counterclockwise rotation whereas the southern limb accommodated < 30° clockwise rotation (Figure 6.2 A). Whether and how the basement highs were involved in the rotations cannot be assessed with the available kinematic data. They could have played a role in the tectonic process either actively rotating or passively forcing the belt to rotate to accommodate a pre-rotation angular shape. During the orocline bending/buckling process, and likely due to the space problems generated by the rotation of the hinge, the Monterrey Salient began folding at ~60 - 50 Ma (Nemkin et al., 2019). Finally, after the orocline formation was completed, the Laramide-style thick skinned tectonic event occurred (Figure 6.2 B), cross-cutting the curved shape of the orocline (for example, see the Norias fault in the San Julián block; Figure 1).

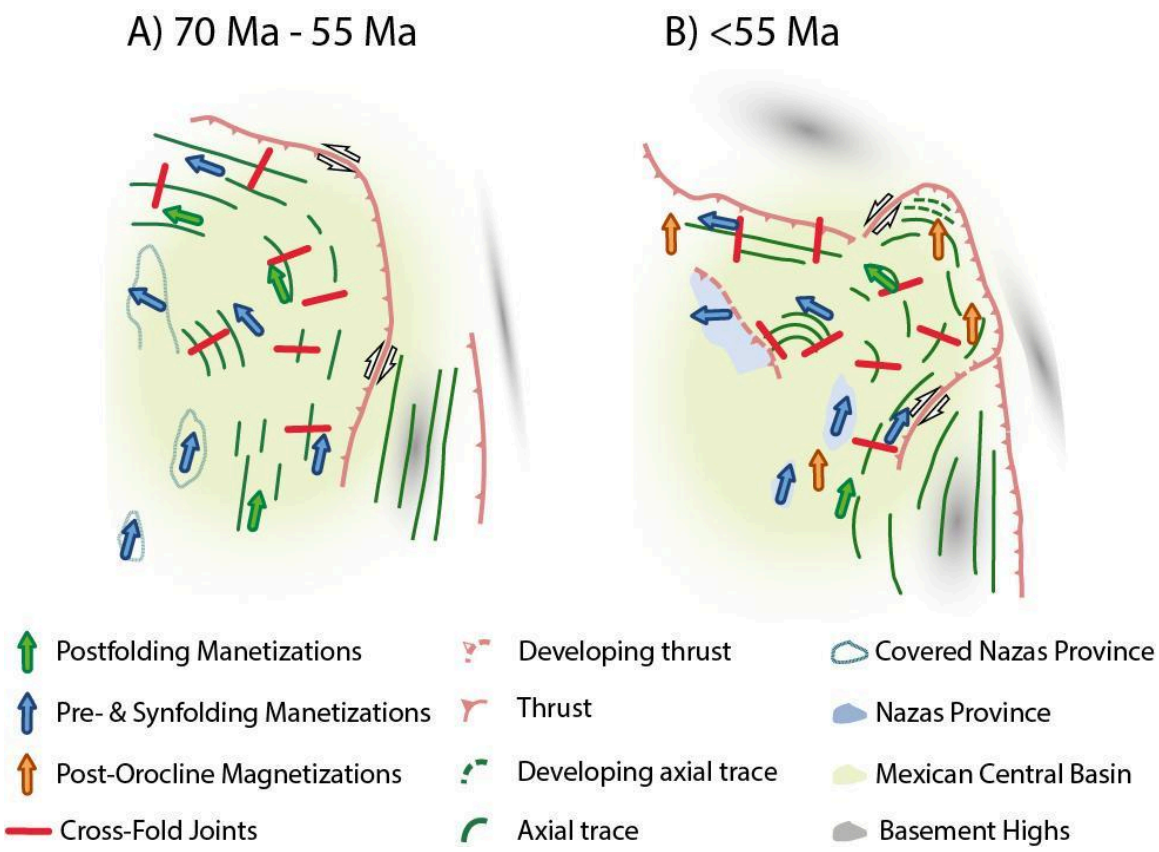

Figure 6.2 Tectonic evolution model continued: A) Shows principal time interval when substantial rotations occurred. B) Shows the final undistorted magnetizations posterior to Orocline Bending/Buckling of the Sierra Madre Oriental.

This kinematic scenario calls for a geodynamic mechanism, at present, we cannot confidently provide one, however we can speculate on it. The subduction of the Farallon plate below the North American plate is the main geodynamic process that could play a significant role in the oroclinal bending process. The Cocos slab and the imaged Farallon subducted plate contain steep thickened segments and low-angle “flat slab” segments in the upper mantle and in the upper lower mantle (Boschman, et al., 2018a; b). The observed variations in geometry of the slab suggest episodes of slab retreat and advance, which these subduction scenarios translate to extension and shortening events respectively(Heuret & Lallemand, 2005; Lallemand, 2005). It is likely that an episode of flat slab subduction, which would also explain, at

least partially, the distribution pattern of magmatic rocks in the Sierra Madre Oriental, could generate the required differential deformation to bend the Sierra Madre Oriental.

6.2 Recapitulation

This thesis investigates the vertical-axis rotational kinematics of the Sierra Madre Oriental in northeastern Mexico, a prominently curved segment of the Mexican Fold and Thrust Belt (MFTB). The integrated approach that combines paleomagnetic and structural analyses shows robust evidence that the Sierra Madre Oriental Orocline formed during Maastrichtian to Paleocene times.

This thesis identifies multiple remagnetization events in NE México. These include a widespread Late Jurassic remagnetization affecting the Nazas, La Joya, and La Boca formations, likely driven by hypabyssal intrusions, and a younger remagnetization event postdating 60 Ma. The Taraises Formation preserves pre-, syn-, and post-folding magnetizations, with the pre-folding component interpreted as (pseudo-)primary, while the syn- and post-folding components are linked to remagnetization during the thin-skinned Sevier event (110–50 Ma).

This region exhibits large-scale vertical-axis rotations, with approximately 90° counterclockwise rotation in the northern limb of the proposed Sierra Madre Oriental Orocline and less than 30° clockwise rotation in the southern limb. This orocline, a 450 km-long, ~110° curved belt extending from Durango to San Luis Potosí, initially developed as a rectilinear N–S fold-and-thrust belt parallel to the subduction trench. Its present curvature is the result of an oroclinal bending process between 70 and 55 Ma, indicating a Late Cretaceous–Early Eocene secondary orocline formation.

The potential occurrence of large-scale oroclinal bending or buckling in the North American Cordillera could profoundly reshape our understanding of this complex Mesozoic-Cenozoic tectonic system. Investigating the formation mechanisms of the Sierra Madre Oriental Orocline is crucial for refining our knowledge of the Eastern Pacific-Panthalassa subduction system and its role during the fragmentation of Pangea. Furthermore, the new kinematics proposed for the Sierra Madre Oriental Orocline may provide insights into the tectonic evolution of basement highs and cratonic blocks in northeastern Mexico. These blocks, considered mobile from the Mesozoic to the Eocene, remain poorly constrained due to limited outcrop exposure and scarce geophysical data (e.g., Keppie, 2004; Lawton and Molina-Garza, 2014). A deeper understanding of their distribution and kinematic history is essential not only for reconstructing Mesozoic and Cenozoic tectonics but also for deciphering the Paleozoic and pre-Paleozoic evolution of North America.

References

Alemán-Gallardo, E. A., Ramírez-Fernández, J. A., Rodríguez-Díaz, A. A., Velasco-Tapia, F., Jenchen, U., Cruz-Gámez, E. M., De León-Barragán, L., & Navarro-De León, I. (2019). Evidence for an Ordovician continental arc in the pre-Mesozoic basement of the Huizachal–Peregrina Anticlinorium, Sierra Madre Oriental, Mexico: Peregrina Tonalite. *Mineralogy and Petrology*, *113*(4), 505–525. https://doi.org/10.1007/s00710-019-00660-4

Anderson, E. M. (1951). The Dynamics of Faulting and Dyke Formation: With Applications to Britain. *Nature*, *149*(3789), 651–652. https://doi.org/10.1038/149651b0

Anderson, T. H. (2005). *The Mojave-Sonora Megashear Hypothesis: Development, Assessment, and Alternatives*. Geological Society of America.

Anderson, T. H., & Schmidt, V. A. (1983). The evolution of Middle America and the Gulf of Mexico–Caribbean Sea region during Mesozoic time. *Geological Society of America Bulletin*, *94*(8), 941. https://doi.org/10.1130/0016-7606(1983)94<941:TEOMAA>2.0.CO;2

Barboza-Gudiño, J. R., Molina-Garza, R. S., & Lawton, T. F. (2012). Sierra de Catorce: Remnants of the ancient western equatorial margin of Pangea in central Mexico. In J. J. Aranda-Gómez, G. Tolson, & R. S. Molina-Garza

(Eds.), *The Southern Cordillera and Beyond* (Vol. 25, p. 0). Geological Society of America. https://doi.org/10.1130/2012.0025(01)

Barboza-Gudiño, J. R., Orozco-Esquivel, M. T., Gómez-Anguiano, M., & Zavala-Monsiváis, A. (2008). The Early Mesozoic volcanic arc of western North America in northeastern Mexico. *Journal of South American Earth Sciences*, *25*(1), 49–63. https://doi.org/10.1016/j.jsames.2007.08.003

Barboza-Gudiño, J. R., Zavala-Monsiváis, A., Castellanos-Rodríguez, V., Jaime-Rodríguez, D., & Almaraz-Martínez, C. (2021). Subduction-related Jurassic volcanism in the Mesa Central province and contemporary Gulf of Mexico opening. *Journal of South American Earth Sciences*, *108*, 102961. https://doi.org/10.1016/j.jsames.2020.102961

Barboza-Gudiño, J. R., Zavala-Monsiváis, A., Venegas-Rodríguez, G., & Barajas-Nigoche, L. D. (2010). Late triassic stratigraphy and facies from northeastern Mexico: Tectonic setting and provenance. *Geosphere*, *6*(5), 621–640. Scopus. https://doi.org/10.1130/GES00545.1

Bartolini, C., Lang, H., & Spell, T. (2003). *Geochronology, Geochemistry, and Tectonic Setting of the Mesozoic Nazas Arc in North-Central Mexico, and its Continuation to Northern South America*. 427–461. http://archives.datapages.com/data/specpubs/memoir79/CHAPTER20/CHAPTER20.HTM

Bartolini, C., Wilson, J. L., & Lawton, T. F. (1999). *Mesozoic Sedimentary and Tectonic History of North-central Mexico*. Geological Society of America.

Belcher, R. C. (1979). *Depositional Environments, Paleomagnetism, and Tectonic Significance of Huizachal Red Beds (Lower Mesozoic), Northeastern Mexico*. University of Texas at Austin.

Boschman, L. M., Molina Garza, R. S., Langereis, C. G., & van Hinsbergen, D. J. J. (2018). Paleomagnetic constraints on the kinematic relationship between the Guerrero terrane (Mexico) and North America since Early Cretaceous time. *GSA Bulletin*, *130*(7–8), 1131–1142. https://doi.org/10.1130/B31916.1

Boschman, L. M., van Hinsbergen, D. J. J., Kimbrough, D. L., Langereis, C. G., & Spakman, W. (2018). The Dynamic History of 220 Million Years of Subduction Below Mexico: A Correlation Between Slab Geometry and Overriding Plate Deformation Based on Geology, Paleomagnetism, and Seismic Tomography. *Geochemistry, Geophysics, Geosystems*, *19*(12), 4649–4672. https://doi.org/10.1029/2018GC007739

Busby, C. J., & Centeno-García, E. (2022). The “Nazas Arc” is a continental rift province: Implications for Mesozoic tectonic reconstructions of the southwest Cordillera, U.S. and Mexico. *Geosphere*, *18*(2), 647–669. https://doi.org/10.1130/GES02443.1

Butler, R. (1992). Paleomagnetism: Magnetic Domains to Geologic Terranes. *Blackwell Science Inc*.

Cameron, K. L., Lopez, R., Ortega-Gutiérrez, F., Solari, L. A., Keppie, J. D., & Schulze, C. (2004). U-Pb geochronology and Pb isotopic compositions of

leached feldspars: Constraints on the origin and evolution of Grenville rocks from eastern and southern Mexico. In R. P. Tollo, J. McLelland, L. Corriveau, & M. J. Bartholomew (Eds.), *Proterozoic Tectonic Evolution of the Grenville Orogen in North America* (Vol. 197, p. 0). Geological Society of America. https://doi.org/10.1130/0-8137-1197-5.755

Campa, M. F., & Coney, P. J. (1983). Tectono-stratigraphic terranes and Mineral resource distributions in Mexico. *Canadian Journal of Earth Sciences*, *20(6)*, 1040–1051. https://doi.org/10.1139/e83-094

Carey, S. W. (1955). The orocline concept in geotectonics-Part I. *Papers and Proceedings of the Royal Society of Tasmania*, *89*, 255–288.

Centeno-García, E. (2017). Mesozoic tectono-magmatic evolution of Mexico: An overview. *Ore Geology Reviews*, *81*, 1035–1052. https://doi.org/10.1016/j.oregeorev.2016.10.010

Centeno-García, E., Anderson, T. H., Nourse, J. A., McKee, J. W., & Steiner, M. B. (2005). Review of upper Paleozoic and lower Mesozoic stratigraphy and depositional environments, central and west Mexico: Constraints on terrane analysis and paleogeography. *SPECIAL PAPERS-GEOLOGICAL SOCIETY OF AMERICA*, *393*, 233.

Centeno-García, E., Guerrero-Suastegui, M., & Talavera-Mendoza, O. (2008). The Guerrero Composite Terrane of western Mexico: Collision and subsequent rifting in a supra-subduction zone. In A. E. Draut, Peter. D. Clift, & D. W. Scholl (Eds.), *Formation and Applications of the*

Sedimentary Record in Arc Collision Zones (Vol. 436, p. 0). Geological Society of America. https://doi.org/10.1130/2008.2436(13)

Chávez-Cabello, G., Cossío-Torres, T., & Peterson-Rodríguez, R. H. (2004). Change of the maximum principal stress during the Laramide Orogeny in the Monterrey salient, northeast México. In A. J. Sussman & A. B. Weil (Eds.), *Orogenic curvature: Integrating paleomagnetic and structural analyses* (Vol. 383, p. 0). Geological Society of America. https://doi.org/10.1130/0-8137-2383-3(2004)383[145:COTMPS]2.0.CO;2

Chávez-Cabello, G., Torres Ramos, A., Porras Vázquez, N. D., Cossio Torres, T., & Aranda Gómez, J. J. (2011). *Evolución estructural del frente tectónico de la Sierra Madre Oriental en el Cañón Santa Rosa, Linares, Nuevo León*. *63*(2), 253–270.

Cifelli, F., Mattei, M., & Della Seta, M. (2008). Calabrian Arc oroclinal bending: The role of subduction. *Tectonics*, *27*(5). https://doi.org/10.1029/2008TC002272

Cifelli, F., Mattei, M., & Rossetti, F. (2007). Tectonic evolution of arcuate mountain belts on top of a retreating subduction slab: The example of the Calabrian Arc. *Journal of Geophysical Research: Solid Earth*, *112*(B9). https://doi.org/10.1029/2006JB004848

Clement, B. M., Poetisi, E., Bralower, T. J., Cobabe, E., & Longoria, J. (2000). Magnetostratigraphy of mid-Cretaceous limestones from the Sierra Madre of northeastern Mexico. *Geophysical Journal International*, *143*(1),

219–229. https://doi.org/10.1046/j.1365-246X.2000.00232.x

De Boer, C. B., & Dekkers, M. J. (1998). Thermomagnetic behaviour of haematite and goethite as a function of grain size in various non-saturating magnetic fields. *Geophysical Journal International*, *133*(3), 541–552.

DeCelles, P. G. (1994). Late Cretaceous-Paleocene synorogenic sedimentation and kinematic history of the Sevier thrust belt, northeast Utah and southwest Wyoming. *GSA Bulletin*, *106*(1), 32–56. https://doi.org/10.1130/0016-7606(1994)106<0032:LCPSSA>2.3.CO;2

DeCelles, P. G. (2004). Late Jurassic to Eocene evolution of the Cordilleran thrust belt and foreland basin system, western U.S.A. *American Journal of Science*, *304*(2), 105–168. https://doi.org/10.2475/ajs.304.2.105

DeCelles, P. G., Ducea, M. N., Kapp, P., & Zandt, G. (2009). Cyclicity in Cordilleran orogenic systems. *Nature Geoscience*, *2*(4), Article 4. https://doi.org/10.1038/ngeo469

DeCelles, P. G., & Giles, K. A. (1996). Foreland basin systems. *Basin Research*, *8*(2), 105–123. https://doi.org/10.1046/j.1365-2117.1996.01491.x

Deenen, M. H., Langereis, C. G., van Hinsbergen, D. J., & Biggin, A. J. (2011). Geomagnetic secular variation and the statistics of palaeomagnetic directions. *Geophysical Journal International*, *186*(2), 509–520.

Dickinson, W. R., & Lawton, T. F. (2001). Carboniferous to Cretaceous assembly and fragmentation of Mexico. *Geological Society of America Bulletin*,

113(9), 1142–1160.

Dickinson, W. R., & Snyder, W. S. (1978). Plate tectonics of the Laramide orogeny. In V. Matthews III (Ed.), *Laramide Folding Associated with Basement Block Faulting in the Western United States* (Vol. 151, p. 0). Geological Society of America. https://doi.org/10.1130/MEM151-p355

Draper, N. R., & Smith, H. (1998). *Applied Regression Analysis*. (3rd ed.). Wiley-Interscience. https://www.wiley.com/en-us/Applied+Regression+Analysis%2C+3rd+Edition-p-9780471170822

Dunlop, D. J., & Özdemir, Ö. (1997). *Rock magnetism: Fundamentals and frontiers*. Cambridge university press.

Dunne, W. M., & North, C. P. (1990). Orthogonal fracture systems at the limits of thrusting: An example from southwestern Wales. *Journal of Structural Geology*, *12*(2), 207–215. https://doi.org/10.1016/0191-8141(90)90005-J

Eguiluz, S. (2021). Deformación de sedimento blando en la Formación Cuesta del Cura, México. *Deformación de Sedimento Blando En laFormación Cuesta Del Cura, México*. https://www.academia.edu/83425508/Deformaci%C3%B3n_de_sedimento_blando_en_la_Formaci%C3%B3n_Cuesta_del_Cura_M%C3%A9xico

Eguiluz, S., Aranda, M., & Marrett, R. (2000). Tectónica de la Sierra Madre Oriental, México. *Boletín de La Sociedad Geológica Mexicana*, *53*(1), 1–26.

Eguiluz y de Antuñano, S. (2022). Estratigrafía y evolución estructural del Bloque de Coahuila, noreste de México. *Boletín de la Sociedad Geológica Mexicana*, *74*(2). https://doi.org/10.18268/bsgm2022v74n2a110522

Eichelberger, N., & McQuarrie, N. (2015). Kinematic reconstruction of the Bolivian orocline. *Geosphere*, *11*(2), 445–462. https://doi.org/10.1130/GES01064.1

Eldredge, S., Bachtadse, V., & Van der Voo, R. (1985). Paleomagnetism and the orocline hypothesis. *Tectonophysics*, *119*(1–4), 153–179.

Engelder, T., & Geiser, P. (1980). On the use of regional joint sets as trajectories of paleostress fields during the development of the Appalachian Plateau, New York. *Journal of Geophysical Research: Solid Earth*, *85*(B11), 6319–6341. https://doi.org/10.1029/JB085iB11p06319

Fastovsky, D. E., Hermes, O. D., Strater, N. H., Bowring, S. A., Clark, J. M., Montellano, M., & Rene, H. R. (2005). *Pre–Late Jurassic, fossil-bearing volcanic and sedimentary red beds of Huizachal Canyon, Tamaulipas, Mexico*.

Fischer, M. P., & Jackson, P. B. (1999). Stratigraphic controls on eformation patterns in fault-related folds: A detachment fold example from the Sierra Madre Oriental, northeast Mexico. *Journal of Structural Geology*, *21*(6), 613–633. https://doi.org/10.1016/S0191-8141(99)00044-9

Fitz-Díaz, E., Hall, C. M., & van der Pluijm, B. A. (2016). XRD-based 40Ar/39Ar age

correction for fine-grained illite, with application to folded carbonates in the Monterrey Salient (northern Mexico). *Geochimica et Cosmochimica Acta*, *181*, 201–216. https://doi.org/10.1016/j.gca.2016.02.004

Fitz-Díaz, E., Hudleston, P., Tolson, G., & van der Pluijm, B. (2014). Progressive, episodic deformation in the Mexican Fold–Thrust Belt (central Mexico): Evidence from isotopic dating of folds and faults. *International Geology Review*, *56*(6), 734–755. https://doi.org/10.1080/00206814.2014.896228

Fitz-Díaz, E., Lawton, T. F., Juárez-Arriaga, E., & Chávez-Cabello, G. (2018). The Cretaceous-Paleogene Mexican orogen: Structure, basin development, magmatism and tectonics. *Earth-Science Reviews*, *183*, 56–84.

Flinn, D. (1962). On folding during three-dimensional progressive deformation. *Quarterly Journal of the Geological Society*, *118*(1–4), 385–428.

Frost, C., & Thompson, S. G. (2000). Correcting for Regression Dilution Bias: Comparison of Methods for a Single Predictor Variable. *Journal of the Royal Statistical Society Series A: Statistics in Society*, *163*(2), 173–189. https://doi.org/10.1111/1467-985X.00164

Gerritsen, D., Vaes, B., & van Hinsbergen, D. J. (2022). Influence of data filters on the position and precision of paleomagnetic poles: What is the optimal sampling strategy? *Geochemistry, Geophysics, Geosystems*, *23*(4), e2021GC010269.

Goldhammer, R. K. (1999). *Mesozoic sequence stratigraphy and paleogeographic evolution of northeast Mexico*.

Goldhammer, R. K., & Johnson, C. A. (2001). Middle Jurassic-Upper Cretaceous Paleogeographic Evolution and Sequence-stratigraphic Framework of the Northwest Gulf of Mexico Rim. In C. Bartolini, R. T. Buffler, & A. Cantú-Chapa (Eds.), *The Western Gulf of Mexico Basin: Tectonics,Sedimentary Basins, and Petroleum Systems* (Vol. 75, p. 0). American Association of Petroleum Geologists. https://doi.org/10.1306/M75768C3

Goldhammer, R. K., Lehmann, P. J., Todd, R. G., Wilson, J. L., Ward, W. C., & Johnson, C. R. (1991). Sequence stratigraphy and cyclostratigraphy of the Mesozoic of the Sierra Madre Oriental, northeast Mexico. *Society for Sedimentary Geology*, *a field guidebook: Gulf Coast Section,* 85. https://store.beg.utexas.edu/gcs-sepm-publications/1901-gcs212.html

Golub, G. H., & van Loan, C. F. (1980). An Analysis of the Total Least Squares Problem. *SIAM Journal on Numerical Analysis*, *17*(6), 883–893. https://doi.org/10.1137/0717073

Gómez-Torres, R. C., Cavazos-Tovar, J. G., Chávez-Cabello, G., Aranda-Gómez, J. J., & Ramírez-Peña, C. F. (2025). U-Pb, Hf isotopes and trace elements of zircon reveals a Mesoproterozoic crustal source for the Jurassic Caopas sub-volcanic intrusion: Northern part of the Nazas Igneous Province in Mexico. *Journal of South American Earth Sciences*, *151*, 105266. https://doi.org/10.1016/j.jsames.2024.105266

González-Naranjo, G., Molina Garza, R., Aranda-Gomez, J., González, M.,

Aguillón-Robles, A., Iriondo, A., & Bellon, H. (2012). Paleomagnetismo y edad de la Ignimbrita Panalillo Superior, Campo Volcánico de San Luis Potosí, México. *Boletin de La Sociedad Geologica Mexicana*, *64*, 387–409. https://doi.org/10.18268/BSGM2012v64n3a9

Gose, W. A., Belcher, R. C., & Scott, G. R. (1982). Paleomagnetic results from northeastern Mexico: Evidence for large Mesozoic rotations. *Geology*, *10*(1), 50–54. https://doi.org/10.1130/0091-7613(1982)10<50:PRFNME>2.0.CO;2

Gray, G. G., & Lawton, T. F. (2011). New constraints on timing of Hidalgoan (Laramide) deformation in the Parras and La Popa basins, NE Mexico. *Boletín de La Sociedad Geológica Mexicana*, *63*(2), 333–343. http://www.scielo.org.mx/scielo.php?script=sci_abstract&pid=S1405-3322201100020001 4&lng=es&nrm=iso&tlng=en

Gross, M. R., Fischer, M. P., Engelder, T., & Greenfield, R. J. (1995). Factors controlling joint spacing in interbedded sedimentary rocks: Integrating numerical models with field observations from the Monterey Formation, USA. *Geological Society, London, Special Publications*, *92*(1), 215–233. https://doi.org/10.1144/GSL.SP.1995.092.01.12

Gubbins, D. (2007). Time-Averaged Paleomagnetic Field. In D. Gubbins & E. Herrero-Bervera (Eds.), *Encyclopedia of Geomagnetism and Paleomagnetism* (pp. 947–948). Springer Netherlands. https://doi.org/10.1007/978-1-4020-4423-6_304

Gubbins, D., & Herrero-Bervera, E. (2007). *Encyclopedia of Geomagnetism and Paleomagnetism*. Springer Science & Business Media.

Guerra Roel, R. (2019). *Análisis estructural de la zona norte del bloque de San Julián, Zacatecas México* [Masters, Universidad Autónoma de Nuevo León]. http://eprints.uanl.mx/18367/

Guerra Roel, R. (2023). *Repository files to "The Sierra Madre Oriental Orocline. Paleomagnetism of The Nazas Province in NE México."* [Dataset]. Zenodo. https://doi.org/10.5281/zenodo.10914408

Guerra Roel, R., Pastor Galán, D., Chávez-Cabello, G., Ramírez-Peña, C. F., Aranda Gómez, J. J., Patiño Méndez, G., Giovanny Nova, R., Rodríguez-Parra, A., & Molina Garza, R. S. (2024). The Sierra Madre Oriental Orocline: Paleomagnetism of the Nazas Province in NE Mexico. *Journal of Geophysical Research: Solid Earth*, *129*(9), e2024JB029239. https://doi.org/10.1029/2024JB029239

Gutiérrez-Navarro, R., Fitz-Díaz, E., Barboza-Gudiño, J. R., & Stockli, D. F. (2021). Shortening and exhumation of Sierra de Catorce in northeastern Mexico, in light of 40Ar/39Ar illite dating and (U-Th)/He zircon thermochronology. *Journal of South American Earth Sciences*, *111*, 103334. https://doi.org/10.1016/j.jsames.2021.103334

Hernández-Romano, U., Aguilera-Franco, N., Martínez-Medrano, M., & Barceló-Duarte, J. (1997). Guerrero-Morelos Platform drowning at the Cenomanian–Turonian boundary, Huitziltepec area, Guerrero State,

southern Mexico. *Cretaceous Research*, *18*(5), 661–686.

Heuret, A., & Lallemand, S. (2005). Plate motions, slab dynamics and back-arc deformation. *Physics of the Earth and Planetary Interiors*, *149*(1), 31–51. https://doi.org/10.1016/j.pepi.2004.08.022

Hindle, D., & Burkhard, M. (1999). Strain, displacement and rotation associated with the formation of curvature in fold belts; the example of the Jura arc. *Journal of Structural Geology*, *21*(8), 1089–1101. https://doi.org/10.1016/S0191-8141(99)00021-8

Hospers, J. (1954). Rock Magnetism and Polar Wandering. *Nature*, *173*(4416), 1183–1184. https://doi.org/10.1038/1731183a0

Huang, W., Lippert, P. C., Jackson, M. J., Dekkers, M. J., Zhang, Y., Li, J., Guo, Z., Kapp, P., & van Hinsbergen, D. J. J. (2017). Remagnetization of the Paleogene Tibetan Himalayan carbonate rocks in the Gamba area: Implications for reconstructing the lower plate in the India-Asia collision. *Journal of Geophysical Research: Solid Earth*, *122*(2), 808–825. https://doi.org/10.1002/2016JB013662

Imlay, R. W., Cepeda, E., Alvarez, M., & Diaz, T. (1948). Stratigraphic relations of certain Jurassic formations in eastern Mexico. *AAPG Bulletin*, *32*(9), 1750–1761.

Irving, E. (1988). The paleomagnetic confirmation of continental drift. *Eos, Transactions American Geophysical Union*, *69*(44), 994–1014. https://doi.org/10.1029/88EO01169

Jelinek, V. (1981). Characterization of the magnetic fabric of rocks. *Tectonophysics*, *79*(3–4), T63–T67.

Jiménez, G., Speranza, F., Faccenna, C., Bayona, G., & Mora, A. (2014). Paleomagnetism and magnetic fabric of the Eastern Cordillera of Colombia: Evidence for oblique convergence and nonrotational reactivation of a Mesozoic intracontinental rift. *Tectonics*, *33*(11), 2233–2260. https://doi.org/10.1002/2014TC003532

Johnston, S. T. (2001). The Great Alaskan Terrane Wreck: Reconciliation of paleomagnetic and geological data in the northern Cordillera. *Earth and Planetary Science Letters*, *193*(3), 259–272. https://doi.org/10.1016/S0012-821X(01)00516-7

Johnston, S. T., Weil, A. B., & Gutiérrez-Alonso, G. (2013). Oroclines: Thick and thin. *GSA Bulletin*, *125*(5–6), 643–663. https://doi.org/10.1130/B30765.1

Keep, M. (2000). Models of lithospheric-scale deformation during plate collision: Effects of indentor shape and lithospheric thickness. *Tectonophysics*, *326*(3), 203–216. https://doi.org/10.1016/S0040-1951(00)00123-2

Keppie, J. D. (2004). *Terranes of Mexico Revisited: A 1.3 Billion year Odyssey: International Geology Review: Vol 46, No 9*. https://www.tandfonline.com/doi/abs/10.2747/0020-6814.46.9.765

Keppie, J. D., & Ortega-Gutiérrez, F. (2010). 1.3–0.9 Ga Oaxaquia (Mexico): Remnant of an arc/backarc on the northern margin of Amazonia.

Journal of South American Earth Sciences, *29*(1), 21–27. https://doi.org/10.1016/j.jsames.2009.07.001

Kleist, R., Hall, S. A., & Evans, I. (1984). A paleomagnetic study of the Lower Cretaceous Cupido Limestone, northeast Mexico: Evidence for local rotation within the Sierra Madre Oriental. *GSA Bulletin*, *95*(1), 55–60. https://doi.org/10.1130/0016-7606(1984)95<55:APSOTL>2.0.CO;2

Kollmeier, J. M., van der Pluijm, B. A., & Van der Voo, R. (2000). Analysis of Variscan dynamics; early bending of the Cantabria–Asturias Arc, northern Spain. *Earth and Planetary Science Letters*, *181*(1), 203–216. https://doi.org/10.1016/S0012-821X(00)00203-X

Koymans, M. R., Langereis, C. G., Pastor-Galán, D., & van Hinsbergen, D. J. (2016). *Paleomagnetism. org: An online multi-platform open source environment for paleomagnetic data analysis*. Elsevier.

Krýza, O., Lexa, O., Schulmann, K., Guy, A., Gapais, D., Cosgrove, J., & Xiao, W. (2021). Oroclinal buckling and associated lithospheric-scale material flow – insights from physical modelling: Implication for the Mongol-Hingan orocline. *Tectonophysics*, *800*, 228712. https://doi.org/10.1016/j.tecto.2020.228712

Lallemand, S. (2005). *On the relationships between slab dip, back-arc stress, upper plate absolute motion, and crustal nature in subduction zones.* https://agupubs.onlinelibrary.wiley.com/doi/full/10.1029/2005GC000917

Lehmann, C., Osleger, D. A., Montañez, I. P., Sliter, W. V., Vanneau, A. A., &

Banner, J. L. (1999). Evolution of Cupido and Coahuila carbonate platforms, early Cretaceous, northeastern Mexico. *Geological Society of America Bulletin*, *111*(7), 1010–1029. https://doi.org/10.1130/0016-7606(1999)111<1010:EOCACC>2.3.CO;2

Li, P., Rosenbaum, G., & Donchak, P. J. (2012). Structural evolution of the Texas Orocline, eastern Australia. *Gondwana Research*, *22*(1), 279–289.

Liu, L., Gurnis, M., Seton, M., Saleeby, J., Müller, R. D., & Jackson, J. M. (2010). The role of oceanic plateau subduction in the Laramide orogeny. *Nature Geoscience*, *3*(5), 353–357. https://doi.org/10.1038/ngeo829

Maffione, M., Speranza, F., Faccenna, C., & Rossello, E. (2010). Paleomagnetic evidence for a pre-early Eocene (~50Ma) bending of the Patagonian orocline (Tierra del Fuego, Argentina): Paleogeographic and tectonic implications. *Earth and Planetary Science Letters*, *289*(1), 273–286. https://doi.org/10.1016/j.epsl.2009.11.015

Malandri, C., Soukis, K., Maffione, M., Özkaptan, M., Vassilakis, E., Lozios, S., & van Hinsbergen, D. J. J. (2017). Vertical-axis rotations accommodated along the Mid-Cycladic lineament on Paros Island in the extensional heart of the Aegean orocline (Greece). *Lithosphere*, *9*(1), 78–99. https://doi.org/10.1130/L575.1

Markovsky, I., & Van Huffel, S. (2007). Overview of total least-squares methods. *Signal Processing*, *87*(10), 2283–2302. https://doi.org/10.1016/j.sigpro.2007.04.004

Marshak, S. (1988). Kinematics of orocline and arc formation in thin-skinned orogens. *Tectonics*, *7*(1), 73–86. https://doi.org/10.1029/TC007i001p00073

Martini, M., Mori, L., Solari, L., & Centeno-García, E. (2011). Sandstone Provenance of the Arperos Basin (Sierra de Guanajuato, Central Mexico): Late Jurassic–Early Cretaceous Back-Arc Spreading as the Foundation of the Guerrero Terrane. *The Journal of Geology*, *119*(6), 597–617. https://doi.org/10.1086/661989

Martini, M., & Ortega-Gutiérrez, F. (2018). Tectono-stratigraphic evolution of eastern Mexico during the break-up of Pangea: A review. *Earth-Science Reviews*, *183*, 38–55. https://doi.org/10.1016/j.earscirev.2016.06.013

McCaig, A. M., & McClelland, E. (1992). Palaeomagnetic techniques applied to thrust belts. In K. R. McClay (Ed.), *Thrust Tectonics* (pp. 209–216). Springer Netherlands. https://doi.org/10.1007/978-94-011-3066-0_19

McElhinny, M. W. (2007). Geocentric Axial Dipole Hypothesis. In D. Gubbins & E. Herrero-Bervera (Eds.), *Encyclopedia of Geomagnetism and Paleomagnetism* (pp. 281–287). Springer Netherlands. https://doi.org/10.1007/978-1-4020-4423-6_107

Meert, J. G., Pivarunas, A. F., Evans, D. A. D., Pisarevsky, S. A., Pesonen, L. J., Li, Z.-X., Elming, S.-Å., Miller, S. R., Zhang, S., & Salminen, J. M. (2020). The magnificent seven: A proposal for modest revision of the Van der Voo (1990) quality index. *Tectonophysics*, *790*, 228549. https://doi.org/10.1016/j.tecto.2020.228549

Michalzik, D. (1988). *Trias bis tiefste Unter-Kreide der nordöstlichen Sierra Madre Oriental, Mexiko—Fazielle Entwicklung eines passiven Kontinentalrandes* (pp. 1–247).

Michalzik, D. (1991). Facies sequence of Triassic-Jurassic red beds in the Sierra Madre Oriental (NE Mexico) and its relation to the early opening of the Gulf of Mexico. *Sedimentary Geology*, *71*(3), 243–259. https://doi.org/10.1016/0037-0738(91)90105-M

Miser, H. D. (1932). Oklahoma structural salient of the Ouachita Mountains. *Geological Society of America Bulletin*, *v. 43*, 138.

Mixon, R. B., Murray, G. E., & Teodoro, D. G. (1959). Age and Correlation of Huizachal Group (Mesozoic), State of Tamaulipas, Mexico1: ADDENDUM. *AAPG Bulletin*, *43*(4), 757–771. https://doi.org/10.1306/0BDA5ED3-16BD-11D7-8645000102C1865D

Molina Garza, R. (2004). Paleomagnetic reconstruction of Coahuila, Mexico: The Late Triassic Acatita intrusives. *Geofísica Internacional*, *44*. https://doi.org/10.22201/igeof.00167169p.2005.44.2.254

Molina-Garza, R. S., & Iriondo, A. (2005). La Megacizalla Mojave-Sonora: La hipótesis, la controversia y el estado actual de conocimiento. *Boletín de la Sociedad Geológica Mexicana*, *57*(1), 1–26. https://doi.org/10.18268/bsgm2005v57n1a1

Molnar, N., & Buiter, S. (2023). Analogue modelling of the inversion of multiple extensional basins in foreland fold-and-thrust belts. *Solid Earth*, *14*(2),

213–235. https://doi.org/10.5194/se-14-213-2023

Montes, C., Bayona, G., Cardona, A., Buchs, D. M., Silva, C. A., Morón, S., Hoyos, N., Ramírez, D. A., Jaramillo, C. A., & Valencia, V. (2012). Arc-continent collision and orocline formation: Closing of the Central American seaway. *Journal of Geophysical Research: Solid Earth*, *117*(B4). https://doi.org/10.1029/2011JB008959

Mullender, T. A. T., Frederichs, T., Hilgenfeldt, C., de Groot, L. V., Fabian, K., & Dekkers, M. J. (2016). Automated paleomagnetic and rock magnetic data acquisition with an in-line horizontal “2G” system. *Geochemistry, Geophysics, Geosystems*, *17*(9), 3546–3559. https://doi.org/10.1002/2016GC006436

Mullender, T. a. T., van Velzen, A. J., & Dekkers, M. J. (1993). Continuous drift correction and separate identification of ferrimagnetic and paramagnetic contributions in thermomagnetic runs. *Geophysical Journal International*, *114*(3), 663–672. https://doi.org/10.1111/j.1365-246X.1993.tb06995.x

Nemkin, S. R., Chávez-Cabello, G., Fitz-Díaz, E., van der Pluijm, B., & Van der Voo, R. (2019). Concurrence of folding and remagnetization events in the Monterrey Salient (NE Mexico). *Tectonophysics*, *760*, 58–68. https://doi.org/10.1016/j.tecto.2017.12.002

Nova-Rodríguez, E. G. (2016). *VISIÓN PALEOGEOGRÁFICA DEL ARCO JURÁSICO CODILLERANO EN MÉXICO A PARTIR DE*

PALEOMAGNETISMO EN LA FORMACIÓN NAZAS. Universidad Nacional Aútonoma de México.

Nowicki, M. J., Hall, S. A., & Evans, I. (1993). Palaeomagnetic evidence for local and regional post-eocene rotations in northern Mexico. *Geophysical Journal International*, *114*(1), 63–75. https://doi.org/10.1111/j.1365-246X.1993.tb01466.x

Ocampo-Díaz, Y. Z. E. (2011). *IMPLICACIONES TECTONO-SEDIMENTARIAS DE LAS INTERCALACIONES CLÁSTICAS EN EL LÍMITE JURÁ SICO – CRETÁ CICO DEL NORESTE DE MÉXICO (FOSA DE MONTERREY Y CUENCA DE SABINAS).* [Tesis Doctoral]. UNIVERSIDAD AUTÓNOMA DE NUEVO LEÓN FACULTAD DE CIENCIAS DE LA TIERRA.

Ocampo-Díaz, Y. Z. E., Guerrero-Suastegui, M., & Jenchen, U. (2012). Petrography and source for the Galeana sandy member (Taraises Formation, Valanginian-early Hauterivian), Sierra Madre Oriental, NE Mexico. *Boletín de La Sociedad Geológica Mexicana*, *64*(3), 335–352. http://www.scielo.org.mx/scielo.php?script=sci_abstract&pid=S1405-3322 2012000300006&lng=es&nrm=iso&tlng=es

Ocampo-Díaz, Y. Z. E., Pinzon-Sotelo, M. P., Chávez-Cabello, G., Ramírez-Díaz, A., Martínez-Paco, M., Velasco-Tapia, F., Guerrero-Suastegui, M., Barboza-Gudiño, J. R., Ocampo-Díaz, Y. Z. E., Pinzon-Sotelo, M. P., Chávez-Cabello, G., Ramírez-Díaz, A., Martínez-Paco, M., Velasco-Tapia, F., Guerrero-Suastegui, M., & Barboza-Gudiño, J. R. (2016). Propuesta

nomenclatural y análisis de procedencia de la Formación Concepción del Oro (antes Formación Caracol): Implicaciones sobre la evolución tectónica del sur de Norteamérica durante el Cretácico Tardío. *Revista mexicana de ciencias geológicas*, *33*(1), 3–33. http://www.scielo.org.mx/scielo.php?script=sci_abstract&pid=S1026-87742016000100003&lng=es&nrm=iso&tlng=es

O'Reilly, W. (1984). Applications of rock and mineral magnetism. In W. O'Reilly (Ed.), *Rock and Mineral Magnetism* (pp. 194–212). Springer US. https://doi.org/10.1007/978-1-4684-8468-7_9

Ortega-Gutierrez, F., Ruiz, J., & Centeno-Garcia, E. (1995). Oaxaquia, a Proterozoic microcontinent accreted to North America during the late Paleozoic. *Geology*, *23*(12), 1127–1130. https://doi.org/10.1130/0091-7613(1995)023<1127:OAPMAT>2.3.CO;2

Padilla y Sánchez, R. J. (1985). Las estructuras de la Curvatura de Monterrey, estados de Coahuila, Nuevo León, Zacatecas y San Luis Potosí. *Revista Mexicana de Ciencias Geológicas*, *6*(1), 1–20.

Pantoja-Alor, J. (1972). Datos geológicos y estratigráficos de la Formación Nazas (memoria), II Convención Nacional. *Mazatlán, Sinaloa, Sociedad Geológica Mexicana*, 25–31.

Parés, J. M. (2015). Sixty years of anisotropy of magnetic susceptibility in deformed sedimentary rocks. *Frontiers in Earth Science*, *3*. https://www.frontiersin.org/articles/10.3389/feart.2015.00004

Parolari, M., Martini, M., Gómez-Tuena, A., Ortega-Gutiérrez, F., Errázuriz-Henao, C., & Cavazos-Tovar, J. G. (2022). The petrogenesis of Early–Middle Jurassic magmatism in southern and central Mexico and its role during the break-up of Western Pangaea. *Geological Magazine*, *159*(6), 873–892. https://doi.org/10.1017/S0016756822000061

Pastor-Galán, D., Gutiérrez-Alonso, G., Dekkers, M. J., & Langereis, C. G. (2017). Paleomagnetism in Extremadura (Central Iberian zone, Spain) Paleozoic rocks: Extensive remagnetizations and further constraints on the extent of the Cantabrian orocline. *Journal of Iberian Geology*, *43*(4), 583–600. https://doi.org/10.1007/s41513-017-0039-x

Pastor-Galán, D., Gutiérrez-Alonso, G., & Weil, A. B. (2011). Orocline timing through joint analysis: Insights from the Ibero-Armorican Arc. *Tectonophysics*, *507*(1), 31–46. https://doi.org/10.1016/j.tecto.2011.05.005

Pastor-Galán, D., Gutiérrez-Alonso, G., Zulauf, G., & Zanella, F. (2012). Analogue modeling of lithospheric-scale orocline buckling: Constraints on the evolution of the Iberian-Armorican Arc. *GSA Bulletin*, *124*(7–8), 1293–1309. https://doi.org/10.1130/B30640.1

Pastor-Galán, D., Martín-Merino, G., & Corrochano, D. (2014). Timing and structural evolution in the limb of an orocline: The Pisuerga–Carrión Unit (southern limb of the Cantabrian Orocline, NW Spain). *Tectonophysics*, *622*, 110–121. https://doi.org/10.1016/j.tecto.2014.03.004

Pfiffner, O. A. (2006). Thick-skinned and thin-skinned styles of continental

contraction. In S. Mazzoli & R. W. H. Butler (Eds.), *Styles of Continental Contraction* (p. 0). Geological Society of America. https://doi.org/10.1130/2006.2414(09)

Pfiffner, O. A. (2017). Thick-Skinned and Thin-Skinned Tectonics: A Global Perspective. *Geosciences*, *7*(3), Article 3. https://doi.org/10.3390/geosciences7030071

Pindell, J., & Kennan, L. (2001). Kinematic Evolution of the Gulf of Mexico and Caribbean. In R. H. Fillon, N. C. Rosen, P. Weimer, A. Lowrie, H. Pettingill, R. L. Phair, H. H. Roberts, & H. H. van Hoom (Eds.), *Petroleum Systems of Deep-Water Basins–Global and Gulf of Mexico Experience* (Vol. 21, p. 0). SEPM Society for Sedimentary Geology. https://doi.org/10.5724/gcs.01.21.0193

Price, M. F. (2015). Why do mountains matter? In M. Price (Ed.), *Mountains: A Very Short Introduction* (p. 0). Oxford University Press. https://doi.org/10.1093/actrade/9780199695881.003.0001

Pueyo, E. L., Mauritsch, H. J., Gawlick, H.-J., Scholger, R., & Frisch, W. (2007). New evidence for block and thrust sheet rotations in the central northern Calcareous Alps deduced from two pervasive remagnetization events. *Tectonics*, *26*(5). https://doi.org/10.1029/2006TC001965

Pueyo, E. L., Sussman, A. J., Oliva-Urcia, B., & Cifelli, F. (2016). Palaeomagnetism in fold and thrust belts: Use with caution. *Geological Society, London, Special Publications*, *425*(1), 259–276. https://doi.org/10.1144/SP425.14

Rahbek, C., Borregaard, M. K., Colwell, R. K., Dalsgaard, B., Holt, B. G., Morueta-Holme, N., Nogues-Bravo, D., Whittaker, R. J., & Fjeldså, J. (2019). Humboldt's enigma: What causes global patterns of mountain biodiversity? *Science*, *365*(6458), 1108–1113. https://doi.org/10.1126/science.aax0149

Ramírez-Peña, C. F. (2017). *Análisis de la deformación progresiva en la zona sur del sector transversal de Parras y la Saliente de Monterrey, México* [Unpublished PhD. Tesis, Universidad Autónoma de Nuevo León, Facultad de Ciencias de la Tierra.]. https://scholar.google.com/citations?view_op=view_citation&hl=es&user=96g7lyEAAAAJ&citation_for_view=96g7lyEAAAAJ:9yKSN-GCB0IC

Ramírez-Peña, C. F., & Chávez-Cabello, G. (2017). Age and evolution of thin-skinned deformation in Zacatecas, Mexico: Sevier orogeny evidence in the Mexican Fold-Thrust Belt. *Journal of South American Earth Sciences*, *76*, 101–114. https://doi.org/10.1016/j.jsames.2017.01.007

Ramírez-Peña, C. F., Chávez-Cabello, G., Fitz-Díaz, E., Aranda-Gómez, J. J., & Valdés, R. S. (2019). Uplift and syn-orogenic magmatism in the Concepción del Oro Block: A thick-skinned (Laramide style?) contractional structure in the Mexican Fold-Thrust Belt. *Journal of South American Earth Sciences*, *93*, 242–252. https://doi.org/10.1016/j.jsames.2019.04.012

Ries, A. C., & Shackleton, R. M. (1976). Patterns of Strain Variation in Arcuate

FoldBelts. *Philosophical Transactions Ofthe Royal Society of London*, *283*(1312), 281–288.

Rodríguez-Parra, A. (2020). *VISIÓN PALEOGEOGRÁFICA DEL ARCO JURÁSICO CODILLERANO EN MÉXICO A PARTIR DE PALEOMAGNETISMO EN LA FORMACIÓN NAZAS*. Universidad Nacional Aútonoma de México.

Rosenbaum, G., & Lister, G. S. (2004). Neogene and Quaternary rollback evolution of the Tyrrhenian Sea, the Apennines, and the Sicilian Maghrebides. *Tectonics*, *23*(1). https://doi.org/10.1029/2003TC001518

Rubio Cisneros, I. I., Ramírez Fernández, J. A., & García Obregón, R. (2011). Source analysis of jurassic clastic rocks in the Huizachal Valley, Sierra Madre Oriental: Influence from synsedimentary volcanism and the crystalline basement. *Boletín de La Sociedad Geológica Mexicana*, *63*(2), 137–156. http://www.scielo.org.mx/scielo.php?script=sci_abstract&pid=S1405-33222011000200002&lng=es&nrm=iso&tlng=es

Rubio-Cisneros, I. I., & Lawton, T. F. (2011). Detrital zircon U-Pb ages of sandstones in continental red beds at Valle de Huizachal, Tamaulipas, NE Mexico: Record of Early-Middle Jurassic arc volcanism and transition to crustal extension. *Geosphere*, *7*(1), 159–170. https://doi.org/10.1130/GES00567.1

Salvador, A. (1987). Late Triassic-Jurassic Paleogeography and Origin of Gulf of Mexico Basin1. *AAPG Bulletin*, *71*(4), 419–451.

https://doi.org/10.1306/94886EC5-1704-11D7-8645000102C1865D

Sapienza, F., Gallo, L. C., Zhang, Y., Vaes, B., Domeier, M., & Swanson-Hysell, N. L. (2023). Quantitative Analysis of Paleomagnetic Sampling Strategies. *Journal of Geophysical Research: Solid Earth*, *128*(11), e2023JB027211. https://doi.org/10.1029/2023JB027211

Schellart, W. P., Freeman, J., Stegman, D. R., Moresi, L., & May, D. (2007). Evolution and diversity of subduction zones controlled by slab width. *Nature*, *446*(7133), 308–311. https://doi.org/10.1038/nature05615

Schmidt, K. L., Wetmore, P. H., Alsleben, H., & Paterson, S. R. (2014). Mesozoic tectonic evolution of the southern Peninsular Ranges batholith, Baja California, Mexico: Long-lived history of a collisional segment in the Mesozoic Cordilleran arc. In D. M. Morton & F. K. Miller (Eds.), *Peninsular Ranges Batholith, Baja California and Southern California* (p. 0). Geological Society of America. https://doi.org/10.1130/2014.1211(20)

Schwartz, S. Y., & Van der Voo, R. (1983). Paleomagnetic evaluation of the Orocline Hypothesis in the central and southern Appalachians. *Geophysical Research Letters*, *10*(7), 505–508. https://doi.org/10.1029/GL010i007p00505

Shaw, J., Johnston, S. T., Gutiérrez-Alonso, G., & Weil, A. B. (2012). Oroclines of the Variscan orogen of Iberia: Paleocurrent analysis and paleogeographic implications. *Earth and Planetary Science Letters*, *329–330*, 60–70. https://doi.org/10.1016/j.epsl.2012.02.014

Silva-Romo, G., Arellano-Gil, J., Mendoza-Rosales, C., & Nieto-Obregón, J. (2000). A submarine fan in the Mesa Central, Mexico. *Journal of South American Earth Sciences*, *13*(4–5), 429–442.

Stamatakos, J., & Hirt, A. M. (1994). Paleomagnetic considerations of the development of the pennsylvania salient in the central appalachians. *Tectonophysics*, *231*(4), 237–255. https://doi.org/10.1016/0040-1951(94)90037-X

Stegman, D. R., Freeman, J., Schellart, W. P., Moresi, L., & May, D. (2006). Influence of trench width on subduction hinge retreat rates in 3-D models of slab rollback. *Geochemistry, Geophysics, Geosystems*, *7*(3). https://doi.org/10.1029/2005GC001056

Sussman, A. J., & Weil, A. B. (2004). *Orogenic Curvature: Integrating Paleomagnetic and Structural Analyses*. Geological Society of America.

Tardy, M. (1980). *Contribution à l'étude géologique de la Sierra Madre orientale au Mexique.: Stratigraphie, évolution paléogéographique et évolution tectonique sur un profil du secteur transverse de Parras; organisation et géodynamique de la Sierra Madre orientale au passage Domaine alpin caraibe -Cordillère ouest-americaine*. [Phdthesis, Université Pierre et Marie Curie - Paris VI]. https://theses.hal.science/tel-00849853

Tardy, M., Longoria, J., Martínez-Reyes, J., Mitre-Salazar, L. M., Patiño, M., Padilla y Sánchez, R. J., & Ramírez, C. (1975). Observaciones generales sobre la

estructura de la Sierra Madre Oriental: La aloctonía del conjunto cadena alta-altiplano central, entre Torreón, Coah.. Y San Luis Potosí, S.L.P., Mexico | Revista Mexicana de Ciencias Geológicas. *Revista Mexicana de Ciencias Geológicas*, *0*(1), 1–11. https://rmcg.geociencias.unam.mx/index.php/rmcg/article/view/1481

Tarling, D., & Hrouda, F. (1993). *Magnetic Anisotropy of Rocks*. Springer Science & Business Media.

Tauxe, L. (2010). *Essentials of Paleomagnetism*. Univ of California Press.

Tauxe, L., & Watson, G. S. (1994). The fold test: An eigen analysis approach. *Earth and Planetary Science Letters*, *122*(3), 331–341. https://doi.org/10.1016/0012-821X(94)90006-X

Thomas, W. A., & Whiting, B. N. (1995). The Alabama Promontory; an example of the evolution of an Appalachian- Ouachita thrust belt recess at a promontory of the rifted continental margin in Hibbard, J.P., van Staal C.R., and Cawood, P.A., eds., Current Perspectives in the Appalachian-Caledonian Orogen. *Geological Association of Canada Special Paper*, *41*, 1–20.

Trainor, R. J., Nance, R. D., & Keppie, J. D. (2011). Tectonothermal history of the Mesoproterozoic Novillo Gneiss of eastern Mexico: Support for a coherent Oaxaquia microcontinent. *Revista Mexicana de Ciencias Geológicas*, *28*(3), 580–592. http://www.scielo.org.mx/scielo.php?script=sci_abstract&pid=S1026-8774

20110003000018&lng=es&nrm=iso&tlng=en

Turner, J. P., & Hancock, P. L. (1990). Relationships between thrusting and joint systems in the Jaca thrust-top basin, Spanish Pyrenees. *Journal of Structural Geology*, *12*(2), 217–226. https://doi.org/10.1016/0191-8141(90)90006-K

Vaes, B., van Hinsbergen, D. J. J., van de Lagemaat, S. H. A., van der Wiel, E., Lom, N., Advokaat, E. L., Boschman, L. M., Gallo, L. C., Greve, A., Guilmette, C., Li, S., Lippert, P. C., Montheil, L., Qayyum, A., & Langereis, C. G. (2023). A global apparent polar wander path for the last 320 Ma calculated from site-level paleomagnetic data. *Earth-Science Reviews*, *245*, 104547. https://doi.org/10.1016/j.earscirev.2023.104547

van Hinsbergen, D. J. J., & Schmid, S. M. (2012). Map view restoration of Aegean–West Anatolian accretion and extension since the Eocene. *Tectonics*, *31*(5). https://doi.org/10.1029/2012TC003132

Walcott, C. R., & White, S. H. (1998). Constraints on the kinematics of post-orogenic extension imposed by stretching lineations in the Aegean region. *Tectonophysics*, *298*(1), 155–175. https://doi.org/10.1016/S0040-1951(98)00182-6

Warrior, S. (2008). A paleomagnetic investigation of the Mojave-Sonora megashear hypothesis in north-central and northeastern Mexico. *ETD Collection for University of Texas, El Paso*, 1–188. https://scholarworks.utep.edu/dissertations/AAI1453858

Weil, A. B., Gutiérrez-Alonso, G., & Wicks, D. (2013). Investigating the kinematics of local thrust sheet rotation in the limb of an orocline: A paleomagnetic and structural analysis of the Esla tectonic unit, Cantabrian–Asturian Arc, NW Iberia. *International Journal of Earth Sciences*, *102*(1), 43–60. https://doi.org/10.1007/s00531-012-0790-3

Weil, A. B., & Yonkee, A. (2009). Anisotropy of magnetic susceptibility in weakly deformed red beds from the Wyoming salient, Sevier thrust belt: Relations to layer-parallel shortening and orogenic curvature. *Lithosphere*, *1*(4), 235–256. https://doi.org/10.1130/L42.1

Wengler, M., Barboza-Gudiño, J. R., Thomsen, T. B., & Meinhold, G. (2019). Sediment provenance of Triassic and Jurassic sandstones in central Mexico during activity of the Nazas volcanic arc. *Journal of South American Earth Sciences*, *92*, 329–349. https://doi.org/10.1016/j.jsames.2019.03.009

Whitaker, A. E., & Engelder, T. (2005). Characterizing stress fields in the upper crust using joint orientation distributions. *Journal of Structural Geology*, *27*(10), 1778–1787. https://doi.org/10.1016/j.jsg.2005.05.016

Whitaker, A. E., & Engelder, T. (2006). Plate-scale stress fields driving the tectonic evolution of the central Ouachita salient, Oklahoma and Arkansas. *GSA Bulletin*, *118*(5–6), 710–723. https://doi.org/10.1130/B25780.1

Williams, S. A., Singleton, J. S., Prior, M. G., Mavor, S. P., Cross, G. E., & Stockli, D. F. (2021). The early Palaeogene transition from thin-skinned to

thick-skinned shortening in the Potosí uplift, Sierra Madre Oriental, northeastern Mexico. *International Geology Review*, *63*(2), 233–263. https://doi.org/10.1080/00206814.2020.1805802

Yonkee, A., & Weil, A. B. (2010). Reconstructing the kinematic evolution of curved mountain belts: Internal strain patterns in the Wyoming salient, Sevier thrust belt, U.S.A. *GSA Bulletin*, *122*(1–2), 24–49. https://doi.org/10.1130/B26484.1

Zachary, D. W. (2012). *Stratigraphic Controls on the Structural Evolution of the Sierra Madre Oriental Fold-thrust Belt, Eastern Mexico* [Msc Thesis]. University of Houston.

Zavala-Monsiváis, A., Barboza-Gudiño, J. R., Velasco-Tapia, F., & García-Arreola, M. E. (2012). Sucesión volcánica Jurásica en el área de Charcas, San Luis Potosí: Contribución al entendimiento del Arco Nazas en el noreste de México. *Boletín de La Sociedad Geológica Mexicana*, *64*(3), 277–293.

Zhu, Z., Campbell, I. H., Allen, C. M., Brocks, J. J., & Chen, B. (2022). The temporal distribution of Earth's supermountains and their potential link to the rise of atmospheric oxygen and biological evolution. *Earth and Planetary Science Letters*, *580*, 117391. https://doi.org/10.1016/j.epsl.2022.117391

Zijderveld, J. D. A. (1967). *AC demagnetization of rocks: Analysis of results, Methods in Paleomagnetism DW Collinson, KM Creer, SK Runcorn, 254–286*. Elsevier, New York.